NTNU

Norwegian University of
Science and Technology

The Morphology of the Mohn's Ridge

with Special Focus on Listric and Detachment
Faults and their Link to the Formation of
Seafloor-massive Sulfides

Hauke Reimers

Geology
Submission date: May 2017
Supervisor: Steinar Løve Ellefmo, IGP
Co-supervisor: Stephen Lippard, IGB

Norwegian University of Science and Technology
Department of Geoscience and Petroleum

Abstract

Slow and ultraslow-spreading mid-ocean ridges are linked to limited magma supply, discontinuous axial volcanic ridges, asymmetric flank development and formation of oceanic core complexes where lower crustal and upper mantle lithologies are frequently exposed. It is estimated that more than 80 % of the yet to be discovered seafloor-massive sulfide deposits will be found on slow and ultraslow-spreading ridges. The Mohn's Ridge is an ultraslow-spreading ridge segment of the Arctic mid-ocean ridge, where several active and inactive hydrothermal fields and deposits have been discovered, among them the active black smoker vent field" Loki's Castle". The ridge lies within Norwegian Jurisdiction and in light of potential future mineral exploration, warrants further investigation of its morphology, geological structures and their connection to the formation of hydrothermal mineral deposits.

By using digital terrain analysis of a gridded bathymetry, seismic reflection profiles and teleseismic earthquake data, the investigation shows that the northern Mohn's Ridge displays a pronounced asymmetric flank development. The western flank hosts several structures that have been identified as oceanic core complexes, characterized by ridge-parallel, outward-facing breakaway ridges and dome-shaped central surfaces, often displaying ridge-perpendicular corrugations or rafted blocks. Major normal faults close to the valley walls frequently show significant amounts of outward-rotation. In comparison, the eastern flank does not show the same amount of topographical relief and is characterized by the presence of volcanic abyssal hills, which show little to no rotation. From north to south, the ridge transitions from a distinctly asymmetrical to a more symmetrical flank topography, implying that the magma availability increases accordingly. Normal faults at the ridge likely show listric geometries at depth, however, their exact behavior is uncertain due to a lack of subsurface information. The core complexes and their associated detachment faults are probably not active any longer, as they have all been cut off from the axial valley by newer, rotated normal faults.

Major, rotated normal faults located close to the axial valley walls and axial volcanic ridges indicate a significant potential for channeling fluids and building ore deposits, and should therefore be taken into consideration in future exploration. Non-transform faults effectively segment the ridge between the axial volcanic ridges and are indicated to be significant contributors to hydrothermal circulation. However, it should be investigated in further studies what role they may play as potential prospecting tools.

Sammendrag

Sakte- og ultrasaktespredende midthavsrygger er blitt koblet til begrenset magmatilgjengelighet, diskontinuerlige vulkanske akserygger (axial volcanic ridges), asymmetrisk utvikling av flankene og dannelse av marine kjernekompleks hvor bergarter fra den nedre skorpen og øvre mantelen typisk blir blottlagt. Det er estimert at 80 % av de gjenværende og uoppdagede massive havsbunnsmalmene befinner seg på slike typer midthavsrygger. Mohnsryggen er et ultrasaktespredende segment av den arktiske midthavsryggen hvor flere aktive og inaktive hydrotermale forekomster har blitt oppdaget, blant annet den aktive sorte røykeren på «Lokeslottet». Mohnsryggen ligger innenfor norsk jurisdiksjon, og i sammenheng med mulig fremtidig mineralutvinning, kreves det ytterligere analyser og undersøkelse av dens morfologi og oppbygging, geologiske strukturer, samt deres potensielle kobling til dannelsen av hydrotermale mineralforekomster på havbunnen.

Ved bruk av digital terrenganalyse av havbunnsbatymetri, seismiske profiler og teleseismisk jordskjelvdata viser denne studien at den nordre Mohnsryggen er preget av en tydelig asymmetrisk flankeutvikling. På den vestre flanken er det flere strukturer som har blitt identifisert som kjernekompleks. Disse er karakterisert av rygg-parallelle, utoverpekende løsrivelsesrygger (breakaway ridges) og sentrale, kuppelformede overflater som enten viser rifling som forløper perpendikulær med ryggaksen, eller overskjøvede blokker (rafted blocks). Store normalforkastninger i nærheten av rifteveggene er ofte betydelig rotert utover. Til sammenlikning er den østre flanken mye jevnere, med mindre variasjon i topografisk relieff, og er karakterisert av vulkanske dyphavsrygger (abyssal hills). Fra nord til sør viser ryggen en markant overgang fra asymmetrisk til mer symmetrisk spredning, noe som impliserer at den totale magmatilgjengeligheten under ryggaksen øker i samsvar.

Normalforkastninger langs ryggen er trolig listrisk i dybden, likevel er deres nøyaktige adferd uviss på grunn av informasjonsmangel om undergrunnen. Kjernekompleksene og deres assosierte avskjæringsforkastninger (detachment faults) er sannsynligvis ikke aktive lenger, da samtlige har blitt avskjært fra riftedalen av nyere, til dels roterte forkastninger.

Store og roterte normalforkastninger som befinner seg nærme rifteveggene og vulkanske akserygger har trolig et betydelig potensial for å drive væskesirkulering og danne hydrotermale forekomster. Ikke-transformforkastninger segmenterer ryggen mellom de vulkanske akseryggene og er indikert til å være en betydelig bidragsyter til sirkulering av hydrotermale væsker. Det må imidlertid bekreftes i ytterligere studier hvilken rolle de kan spille som potensielle prospekteringsverktøy.

Acknowledgements

I want to thank my supervisor Steinar Ellefmo for making this study possible, for guiding me for the past two years and enabling me to participate on the first MarMine Cruise in august of 2016. He portrays an immense enthusiasm for the topic and is always ready for discussions and new approaches, which resulted in inspiring ideas and thinking “outside the box” to try and resolve some of the challenges related to this topic.

Thank you also to Cyril Juliani for his constructive criticism and recommendations, and Anna Lim for help with the seismic data. Also, a huge thank you to everyone who participated on the MarMine 2016 Cruise for an unforgettable three weeks. Although the days were long and exhausting, it was an amazing experience that I will never forget.

I also thank my father for taking his time to proofread my work and make suggestions for improvements.

Last, but not least, I want to thank my mother who, despite her hardships, always found energy to support me through my ups and downs for the past two years, provided feedback and pushed me when motivation was not at its peak.

Hauke Reimers, Trondheim, May 2017

Table of Contents

List of Figures

List of Tables

Abbreviations

AVR	Axial Volcanic Ridge
AMOR	Arctic Mid-Ocean Ridge
AUV	Autonomous Underwater Vehicle
CH	Copper Hill
DF	Detachment Fault
CTD	Conductivity, Temperature, Depth
DTM	Digital Terrain Model
FZ	Fracture Zone
GIS	Geographic Information System
KR	Knipovich Ridge
LC	Loki's Castle
MOR	Mid-Ocean Ridge
MAR	Mid-Atlantic Ridge
MR	Mohn's Ridge
MT	Mohn's Treasure
NTNU	Norwegian University of Science and Technology
NTO	Non-Transform Offset
OCC	Oceanic Core Complex
ROV	Remotely Operated Vehicle
SMS	Seafloor-Massive Sulfides
TAG	Trans-Atlantic Geotraverse
TFZ	Transform Fault Zone

Common Sulfide Minerals

Anhydrite	$CaSO_4$
Barite	$BaSO_4$
Chalcopyrite	$CuFeS_2$
Galena	PbS
Pyrite	FeS_2
Pyrrhotite	FeS
Sphalerite	ZnS

1. Introduction

1.1 Rationale

This study is part of the increasing search for knowledge about deep-sea mineral resources and what potential such deposits may have as future sources of metal. With increasing demand, but declining size and quality of newly discovered deposits on land (Hannington et al., 2015), companies and countries are looking toward other sources, including the ocean's deep-sea mineral deposits, to satiate the world's needs in the future. Countries such as China, France, Germany and Russia, for instance, are actively exploring for manganese-filled nodules on the Pacific seafloor (Hannington et al., 2011), and the world's first deep-sea mining license was already allocated to Nautilus Minerals in 2011 for exploration in the Bismarck Sea.

However, in addition to environmental concerns regarding the mining of SMS deposits, the debate about the global feasibility of such deposits is still on-going, as current global resource estimates are affected by low sample sizes and large amounts of assumptions, making it challenging to conduct proper assessments due to missing information about size, distribution and composition of the deposits (Petersen et al., 2016).

The world's need for metals will likely only increase in the future, especially with the advancement in the clean energy and technology sectors, along with a steadily increasing global population (Grandell et al., 2016; Petersen et al., 2016). Deep-sea mining could therefore be a chance to diversify the metal market and make it less vulnerable to future global challenges or conflicts (Petersen et al., 2016). Initial models for the resource potential on the MORs (Hannington et al., 2011), however, yield relatively small deposits (median size 70 000 tonnes), with a total Cu + Zn tonnage of $\sim 3\times10^7$ tonnes in the global axial neo-volcanic zones, which is only slightly more than the annual production of these metals from all land-based deposits (Hannington et al., 2011). It should be noted that this tonnage is based on currently active and magmatically-hosted SMS sites in neo-volcanic zones only, and does neither include deposits potentially located off-axis on the ridge flanks close to the valley walls nor extinct deposits that have been transported farther away from the ridge axis. Extinct deposits are, however, challenging to locate as there are no plume signatures to detect and most probably a layer of sediments covering them. Even active black smoker fields may not be as straight forward to detect as one might think, as is the case with the Loki's castle black smoker vent field located at the northern Mohn's Ridge at around ~73°, where a plume does exist, but due to strong and changing currents it is difficult to detect consistently (Pedersen et al., 2013). Based on current

knowledge and estimates, SMS deposits found at spreading centers are therefore thought to only have a minor impact on the global metal market, as opposed to manganese nodules, where the reserves appear to be significantly larger (Petersen et al., 2016).

There exists a general consensus that magma-poor sections of slow-spreading ridges are prone to the formation of large-scale detachment faulting and subsequent core complex formation (e.g. Tucholke et al., 1998), both of which have been linked to hydrothermal fluid circulation and sulfide deposit formation (de Martin et al., 2007; Humphris et al., 2015; McCaig et al., 2007). The Mohn's Ridge is an ultraslow-spreading ridge (Dick et al., 2003) and more than 80% of the yet-to-be discovered SMS deposits are suggested to be located on slow and ultraslow-spreading ridges (Hannington et al., 2011). Initial resource estimates indicate a significant potential within Norwegian jurisdiction along the Mohn's and Knipovich Ridges, albeit with a large amount of uncertainty (Ellefmo et al., 2014). Therefore, the potential of the area appears promising and warrants further research to assess the future resource potential and feasibility of deep-sea mining operations in this area.

1.2 Scope and Purpose of this Study

The purpose of this study is to investigate and analyze the surface morphology of the Mohn's Ridge (MR), a section of the arctic mid-ocean ridge between the Jan Mayen Island and Svalbard, to gain a better understanding of the structural and morphological features. Geological information will be extracted and described in order to determine the distribution of tectonic features and establish what their potential connections are with the occurrence of seafloor-massive-sulfide deposits formed at sites of active hydrothermal venting on the arctic mid-ocean ridge (AMOR). As part of this thesis, I participated on the three-week long NTNU MarMine cruise to the northern Mohn's Ridge, where my primary task was to establish a cruise GIS system that would be continuously updated with the latest data and information (e.g., dive logs, event logs, maps, ROV tracks) and produce maps when required. Whenever the opportunity presented itself, I took part in surveying and logging during the ROV-dives and preparing and packing the recovered geological samples After every dive, the gathered information had to be made easily available and interpretable, so that further decisions could be made.

This study focuses primarily on the northern section of the Mohn's Ridge bordering the Knipovich Ridge (KR) section further to the north. Initial resource estimates indicate significant resources but are affected by high uncertainty (Ellefmo et al., 2014). The overall goal is to gain knowledge and a better understanding of the morphology and structure of the ridge to hopefully reduce some of this uncertainty by constraining which features are present and what their relationship are to SMS deposits. In the future of mineral exploration along the AMOR, it is desirable to limit its vast extent to smaller, more promising areas for detecting SMS deposits. Considering this, a few key aspects shall be investigated in this study:

- What type of structural features characterize the morphology and geology of the study area?
- How are the structures distributed in the study area and what are the geological implication of this?
- How can such features be identified and analyzed?
- What are the relationships between these structures and the formation of hydrothermal mineral deposits, and how is this applicable to the study area?

Pinpointing with certainty the locations of new deposits is outside of the scope of this study. Rather, this work shall contribute to the general understanding of the morphology of the Mohn's Ridge, the mechanisms that are responsible for its formation and potential connections to hydrothermal activity. Deposit sizes, resource estimates or other kinds of quantification of deposits are not part of this.

1.3 Outline of the Thesis

The outline of the thesis is presented below and aims to give a quick overview of what is included and can be expected from each chapter, in a compressed format.

Chapter 1 – Introduction: A general introduction to the study and the context from which it has resulted, along with an outline of the scope and purpose of what is to be achieved, but also a description of the limits of the study and what is not within its scope.

Chapter 2 – Background: This section introduces the geological setting of the Mohn's Ridge and gives an overview of relevant previous work and descriptions of known hydrothermal activity at the ridge.

Chapter 3 – Field Work: Provides a summary of the 2016 NTNU MarMine Cruise to the northern Mohn's Ridge, with a brief overview of the different activities that took place.

Chapter 4 – Theory: This chapter provides the necessary theoretical background knowledge for this study. It represents a detailed literature review of relevant aspects to the topic, and as such lays the theoretical foundation upon which the study is built.

Chapter 5 – Materials and Methods: Gives on overview of the available data and the methods used for data processing and interpretation.

Chapter 6 – Results: This section presents the results and findings of the analysis and interpretation of the data.

Chapter 7 – Discussion: This chapter discusses the results in light of the theoretical background knowledge provided in Chapter 4, and as such relates the findings of this study to the current literature in order to establish a foundation from which conclusions can be derived.

Chapter 8 – Methodological Considerations: Highlights some considerations to be aware of with respect to the methodology.

Chapter 9 – Conclusions: Lists the conclusions of this study considering the questions asked in the introduction of Chapter 1.

Chapter 10 – Further Work: This section discusses a few methods that could be employed in the future.

2. Background

2.1 Geological Setting and Previous Work

The study area (Figure 2.1) is located in the northern part of the Mohn's Ridge section of the Arctic Mid-Ocean Ridge in the Norwegian Sea. The Ridge extends roughly 550 km with an axial strike of 060NE, has a full spreading rate of 16 mm/yr (Dubinin et al., 2013; Klingelhöfer et al., 2000) and represents the boundary between the Eurasian and North American plates (Dauteuil & Brun, 1993). The ridge is unaffected by any transform fault zones (TFZ), instead there are Non-Transform-Offsets (NTOs) resulting in a pronounced en-échelon pattern in the axial valley (Dauteuil & Brun, 1993). Dick et al. (2003) argued that ridge segments displaying such low spreading rates exhibit sufficient tectonic differences compared to slow-spreading ridges with rates > 20 mm/yr that they warrant their own class of spreading ridges, and as such the MR is classified as an ultraslow-spreading ridge.

To the north, at roughly 73 °N, the ridge transitions into the Knipovich Ridge marked by a distinct NW-oriented bend, while to the south it is terminated by the Jan Mayen fracture zone (Dubinin et al., 2013). The northward-continuing KR has an approximate trend ranging from ~ 350 – 005N (Connelly et al., 2007). The axial valley in the transitional bend is magmatically dominated, marked by a pronounced elongate volcanic structure, termed axial volcanic ridge (AVR), 35 km long and peaking at around 2100 m depth (Bruvoll et al., 2009). While the most southern and northern sections of the mid-Atlantic Ridge are typically characterized by orthogonal spreading, the central Mohns is marked by distinctly oblique spreading (Dauteuil & Brun, 1993; Pedersen & Bjerkgård, 2016).

The ridge initiated 53 My ago when the Greenland Sea started to open, forming a rift between the Greenland and European Plates (Dauteuil & Brun, 1993). In its initial stages, the ridge was spreading perpendicularly to its axis, at a very fast rate of 2.5 cm/yr (Talwani & Eldholm, 1977) before a reorganization of the plates 27 My ago led to the oblique spreading seen at the ridge today (Dauteuil & Brun, 1993). Because of this oblique orientation and NTOs, the ridge displays pronounced en-échelon patterns within the axial valley, where lineaments and volcanic ridges are trending about 30° off set, relative to the ridge axis before curving to a parallel orientation when nearing the valley walls.

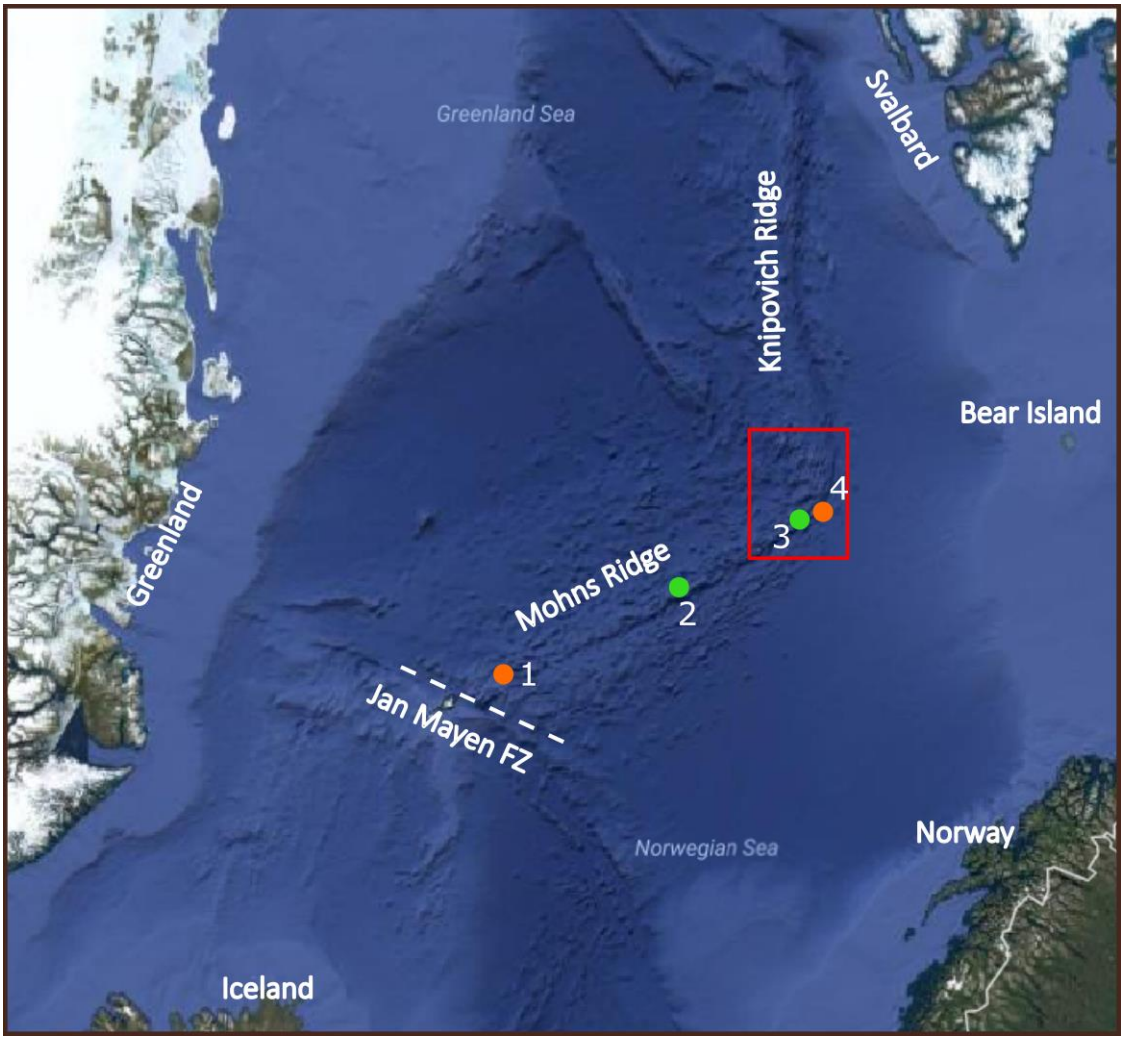

Figure 2.1: *Overview map of the Mohn's Ridge in the Norwegian Sea. It is bound by the Jan Mayen Fracture Zone to the south and a marked bend at the transition to the Knipovich Ridge to the north. Red square marks the study area. 1) Soria Moria and Troll Wall, 2) Copper Hill, 3) Mohn's Treasure, 4) Loki's Castle. Orange = active sites, green = inactive sites. Vent site locations taken from Pedersen et al. (2013).*

A brief morphological and geological overview was provided in studies of volcano-tectonic events and sedimentation (Géli, 1993), followed by a study of the burial history of the Mohns-Knipovich bend (Bruvoll et al., 2009). In the area of the transition between the two ridge segments, distinct differences were found between the western flank of the MR, which contained low-angle faults with large displacements and average dips of $20-25°$, and the eastern flank, dominated by smaller, but more numerous faults with larger variation of fault angles (15-55°) (Bruvoll et al., 2009).

Structures described as oceanic core complexes (OCCs) were identified on the western flank of the MR, characterized by high-relief domal surfaces showing axis-perpendicular corrugations, whereas the eastern flank exhibits lower relief variations and a sediment cover related to the Bear Island Fan to the northeast (Bruvoll et al., 2009). These morphological

observations fit reports by e.g. Escartín et al. (2008) regarding the co-occurrence and relationship between asymmetrical ridge flank development, large-scale detachment faults and formation of core complexes on slow-spreading ridge segments. Sampling from fault surfaces on the western flank of the Mohn - Knipovich bend associated with the domal highs, recovered gabbros and serpentinites (Pedersen et al., 2007), confirming that they are indeed core complexes where lower crust and mantle rocks have been exhumed.

The crustal structure on the Mohn's Ridge is anomalously thin (Figure 2.2), just 4.0 ± 0.5 km, which is about $1-2$ km thinner than usual at the MAR, where spreading is $30-40$ % faster (Klingelhöfer et al., 2000). Typically, oceanic crust can be divided into layers displaying an increasing velocity gradient with depth, where the upper crust is comprised of pillow basalt underlain by a sheeted dike complex (layers 2a and 2b, respectively) with a combined thickness of 2.11 ± 0.55 km and a velocity gradient increasing from $2.5-6.6$ km/s (White et al., 1992). The much thicker layer 3 (4.97 ± 0.9 km) constitutes the lower crust and is believed to contain mostly gabbros representing the cooled magma chambers which originally fed the overlying basaltic dikes and lavas. (Allaby, 2013b). This layer displays higher seismic velocities of around $6.6-7.6$ km/s and is followed by the upper mantle with seismic velocities starting at 7.9 km/s (White et al., 1992).

On the MR, the upper crust has an average thickness of about 1.57 ± 0.16, while the lower crust is about 2.45 ± 0.5 km thick (Klingelhöfer et al., 2000). Variations of the crustal thickness were found to be mostly present in seismic layer 3, whereas the combined thickness of layer 2a and 2b is more or less constant, only changing internally (Klingelhöfer et al., 2000). Furthermore, variations in the thickness of layer 3 were observed below topographic highs, supporting a theory where isostatic compensation is accomplished by increasing the thickness of layer 3 below topographic highs and decreasing its thickness below topographic basins (Klingelhöfer et al., 2000). In addition to an anomalously thin crust, the lower crust and upper mantle also display lower seismic velocities (upper mantle ≈ 7.5 km/s) than is common at mid-ocean ridges (Klingelhöfer et al., 2000). This is suggested to be caused by the influence of hydrothermal activity and circulation of fluids, which lead to serpentinization of the upper mantle and lower crust (Klingelhöfer et al., 2000). This low-velocity effect is observed away from the ridge until a crustal age of 10 My, after which it is suggested that the effect of hydrothermal activity in the crust ceases and subsequently leads to sealing of faults and fractures (Klingelhöfer et al., 2000).

Work regarding total resource estimates and identification of prospective areas with respect to SMS deposits on the MR has been conducted in a report prepared for the NTNU

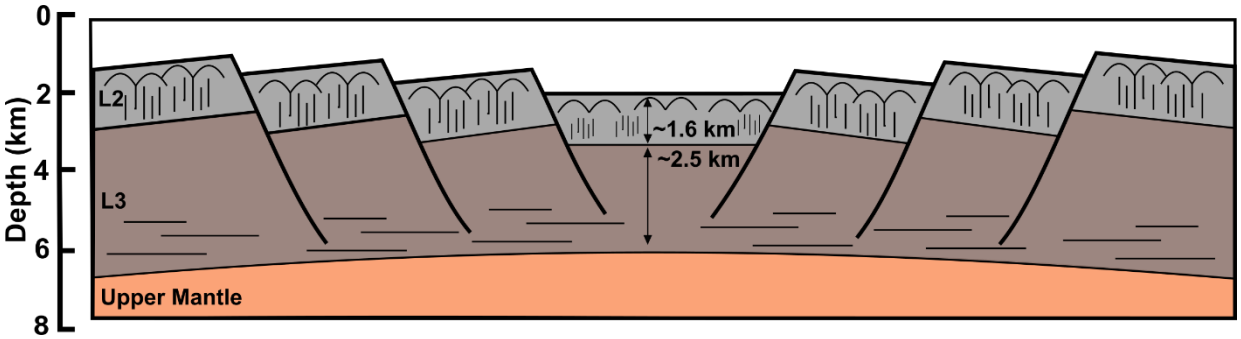

Figure 2.2: *Conceptual crustal structure of the Mohn's Ridge, based on the results of Klingelhöfer et al. (2000). It visualizes the relative thicknesses of the individual layers that make up the approximately 4 km thick crust at the axial valley of the ridge. Layer 2 is roughly 1.6 km thick and comprised of (2a) lava flows and pillow basalt, and (2b) sheeted dikes. Layer 3 is about 2.5 km thick and consists of massive gabbros underlain by a portion of layered gabbros.*

(Cherkashov et al., 2013). This report identified multiple areas along the Mohn and Knipovich Ridges that could host hydrothermal vent fields based on criteria such as the presence of axial volcanic ridges, proximity to major tectonic features and abundance of flat-topped volcanoes within the axial valley.

2.2 Hydrothermal Activity on the Mohn's Ridge

Several hydrothermal vent fields have been identified on the Mohn's Ridge, most notably at the southern and northern ends of the ridge. Below follows a brief overview and description of the know hydrothermal activity.

2.2.1 Soria Moria & Troll Wall

The two high-temperature vent fields, Soria Moria and Troll Wall, are the southernmost known vent fields, located close to the Jan Mayen FZ at approximately 71 °N and 6 °E (Pedersen et al., 2013). Discovered in 2003 during the BIODEEP-05 cruise (Pedersen et al., 2005), they were the first hydrothermal vent fields to be identified on the MR.

Troll Wall is a vent field consisting of at least 10 major vent sites, where multiple 5 – 10 meter high chimneys grow from elongate hydrothermal mounds at the foot of a ~ 100 meter high normal fault at a depth of around 550 meters (Pedersen et al., 2013). The chimneys (Figure 2.3a) are primarily composed of anhydrite ($CaSO_4$), barite ($BaSO_4$) and talc, expelling white smoker fluids measured as hot as 270° C through the surface of a talus deposit (Pedersen et al., 2013). In addition to focused expulsion of fluids through chimneys, areas of diffuse venting through the talus deposit were also observed on the seafloor, marked with distinct white mats of sulfur-oxidizing bacteria and heating of the subsurface of up to 80 °C at 5 – 10 centimeters

depth (Pedersen et al., 2013).

The Soria Moria vent field is the second high-temperature vent site in the Jan Mayen Vent Field area, located approximately 5 kilometers southeast of Troll Wall on top of a volcanic ridge at a depth of around 700 meters (Pedersen et al., 2013). Here, venting occurs in two discrete areas, each 100 – 200 meters across, which, in contrast to Troll Wall, are not located on a talus surface but on top of a volcanic structure (Pedersen et al., 2013). Venting has been observed to occur through two distinct types of structures; in one type, hydrothermal activity is similar to Troll Wall, with white smoker fluids escaping focused and rapidly from typical chimneys structures, 8 – 9 meters tall, whereas the other type of structure (Figure 2.3b) is irregularly shaped, made of barite, silica and minor amounts pyrite (FeS_2), sphalerite (ZnS) and galena (PbS) (Pedersen et al., 2013). These irregularly shaped structures have been observed to grow as large 10 meters tall and 15 – 20 meters wide (Pedersen et al., 2013).

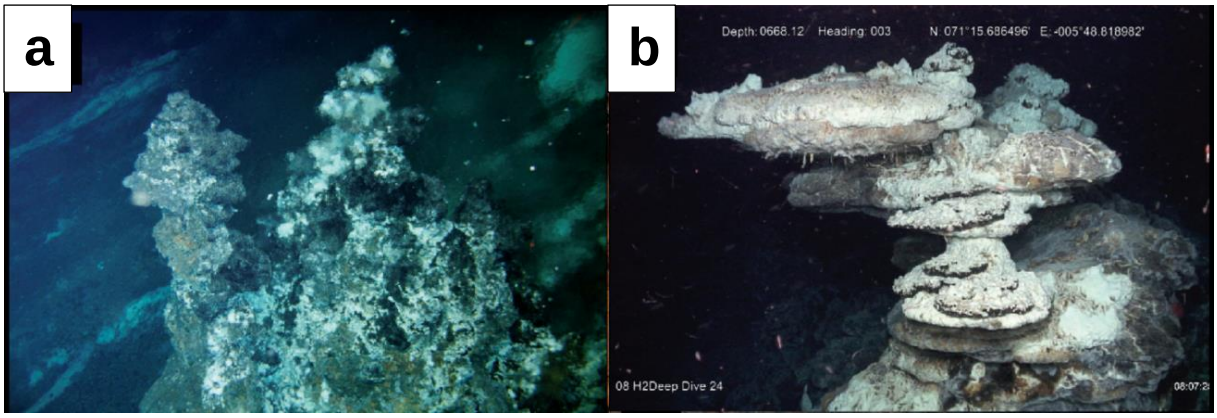

Figure 2.3: *Images of chimneys from Troll Wall and Soria Moria.* ***(a)*** *A white smoker chimney at the Troll Wall field. The white patches on the seafloor mark areas of hydrothermal leaks in the sediments where bacterial mats have grown,* ***(b)*** *Barite-silica chimneys with irregular shape emitting low-temperature fluids at the Soria Moria field. Images from Pedersen et al. (2013).*

2.2.2 Copper Hill

Copper Hill is described as a mineralized fault breccia, discovered and dredge-sampled during a cruise with the *R/V Håkon Mosby* in 2000, and located on the northwestern flank of the central section of the Mohn's Ridge at 72.32 °N and 2.1 °E at around 900 m depth (Pedersen et al., 2013). Sampling was conducted near a ridge that likely represents a rotated and uplifted fault block, with significant block rotation (30 – 40°), which Pedersen et al., (2013) have suggested could represent a breakaway ridge related to formation of a dome-shaped core complexes, elaborating further that many such ridges and accompanying dome-shaped structures are present in the Copper Hill area. Such rotation and uplift of fault blocks on slow-spreading ridges has been linked to severe tectonic extension accommodated on a single or only

a few large, deep-rooted detachment faults (Smith et al., 2008). Formation of core complexes and exhumation of lower crustal and upper mantle rocks is not uncommon on slow and ultraslow-spreading mid-ocean ridges (Smith et al., 2008; Tucholke et al., 1998; Whitney et al., 2013), and a potential connection between the mineralized breccia, hydrothermal activity, detachment faulting and core complexes is therefore possible. The mineral assemblage in the recovered breccia samples consists of around 50 % quartz and 30 % sulfides, with chalcopyrite ($CuFeS_2$) as the primary mineral (Pedersen et al., 2013). Nygård (2004) (as cited in Pedersen et al., 2013) found that multiple generations of chalcopyrite are present in the samples, demonstrating that the sulfide mineralization has taken place syn-tectonically in the epidote zone of hydrothermal systems at temperatures of 330 – 370 °C.

2.2.3 Mohn's Treasure

The Mohn's Treasure is a site located roughly at 73.45 °N and 7.2 °E, where dredging during a cruise with the *R/V Håkon Mosby* in 2002 recovered sulfide samples from a depth of around 2600 meters (Pedersen et al., 2013). The samples contained mostly pyrite in typically fine-grained chimney fragments with distinctly visible fluid channels; however, no plume was detected in the area, suggesting that the deposits originate from a now extinct vent field (Pedersen et al., 2013). The samples were recovered from a ledge along the valley walls, which is most likely the result of a mass wasting event located northwest of an AVR running parallel in the axial valley (Pedersen et al., 2013). Until now, the source of the sulfides recovered from the ledge has not yet been found, although gravity coring southeast of the AVR recovered a 10 centimeter thick sulfide layer at around 1.5 meters into the sediment, which likely is fallout from a nearby (extinct) plume, possibly located on the AVR, as the AVR would likely be an effective barrier for any potential sulfide transport from the Mohn's Treasure (Pedersen et al., 2013). In order to confirm the suggestion that the area indeed is a SMS deposit formed by an extinct hydrothermal field, extensive visual observations and sampling were conducted during the 2016 MarMine Cruise (Ludvigsen et al., 2016), however, at the time of this writing no conclusive indications for this theory were identified.

2.2.4 Loki's Castle

The Loki's Castle vent field area was discovered in 2008 and revisited in 2009 and 2010 for further testing and sampling (Pedersen et al., 2010). The site is located at 73 °N and 8 °E on top of an approximately 30 km long AVR, where the MR transitions into the KR through a marked northwest bend (Pedersen et al., 2013). Venting is here associated with a 150 meter deep rift transecting the AVR at around 2400 meters depth (Pedersen et al., 2010) and is to-date the only known black smoker site on the MR. Fluids are expelled from chimneys, up to 13 m tall, located on top of two mounds approximately 150 m apart, 20 – 30 m high and 150 – 200 m wide, (Pedersen et al., 2010). By area, the Loki's Castle Vent Field yields a slightly larger deposit area size than the TAG deposit on the MAR (35 000 m^2 and 30 000 m^2, respectively)(German et al., 2016), thus making it the largest known SMS deposit in a neo-volcanic setting on the MAR to date.

Whereas Pedersen et al. (2010) originally reported four black smoker chimneys, the number has later increased to five (Pedersen et al., 2013). The fluids reach temperatures up to 317 °C with a primary sulfide assemblage of sphalerite, pyrite, pyrrhotite (*FeS*) and minor amounts of chalcopyrite (Pedersen et al., 2010). On the east side of the mound, low-temperature venting has been observed associated with several smaller chimneys (< 1 m) and white bacterial mats (Pedersen et al., 2010).

Located on top of an AVR, the field known to date is hosted magmatically (Pedersen 2013) and one of the largest found globally, contradicting suggestions that the largest and richest SMS deposits would be hosted tectonically on slow-spreading ridges; however, perhaps on ultraslow-spreading ridges this does not necessarily have to be true (German et al., 2016).

Directly parallel to the AVR, only a few kilometers to the northwest, a faulted and rotated structure has been identified that could be an uplifted domal feature and a basin behind a rotated breakaway ridge (Pedersen et al., 2013). If this is the case, the associated detachment fault could act as a pathway for hydrothermal fluids, enabling long-lived circulation and formation of a large SMS deposit. Such a fluid circulation mechanism has been suggested before (McCaig et al., 2007). Additional topographic highs have been identified and sampled further to the northwest on the ridge flank, revealing gabbros and altered peridotites (serpentinites), confirming that they are oceanic core complexes (Pedersen et al., 2007).

2.2.5 Ægir's Vent Field

The *Æ*gir's vent field was discovered in 2015 by the University of Bergen and is located near a volcanic ridge in the central area of the ridge at 2200 m depth (Olsen et al., 2016). For the time being, the only data collected are video footage and rock samples for geological characterization; however, no detailed publications are available at the time of this writing. The overall vent fauna appears similar to Loki's Castle (Olsen et al., 2016)

3. Field Work - MarMine Cruise 2016

3.1 Cruise Summary

In august 2016, the NTNU Marine Minerals (MarMine) project launched its first research cruise to the Mohn's Ridge, specifically the Loki's Castle and Mohn's Treasure areas (Figure 3.1) to gather samples and test newly developed technology. High-resolution bathymetric data was acquired by an AUV (autonomous underwater vehicle), processed and then imported into the onboard GIS system. AUV tracks and CTD (conductivity, temperature, depth, along with methane and salinity) measurements were also imported and made available for viewing. ROV (remotely operated vehicle) dive logs included regular positioning, manually logged observations and sample locations, which all were plotted onto the newly acquired bathymetric maps. Below follows a short description of the MarMine project and a brief summary of the results from the MarMine Cruise 2016 (Ludvigsen et al., 2016).

MarMine is a NTNU-led project for the research of exploration and exploitation technologies for marine minerals on the extended Norwegian continental shelf, and involves scientists from many different disciplines who work together to solve the challenges that arise from deep-sea mining prospects. For this first cruise, the objectives were to:

- obtain geological samples for mineral characterization and assessment of the mining and mineral processing potential
- test new methods and technologies
- obtain biological samples to establish an analysis of the biological activity present at the hydrothermal areas
- explore areas of interest determined based on earlier analysis of resource potential and permissive tracts

Data acquisition was focused around an AUV, collecting high-resolution bathymetric data for areas of interest, and two ROVs for surveying, video transects and gathering biological and geological samples. In total 22 ROV dives were executed, divided amongst the three primary areas of interest. During the dives at Loki's Castle, extensive geological and biological sampling was conducted during which several hundred kilos of rock samples were collected. A preliminary analysis of the rock compositions was conducted using a handheld XRF scanner, which showed variable amounts of copper and/or zinc, alongside traces of gold and silver. These are, however, very crude results and further testing and analysis is needed for a detailed

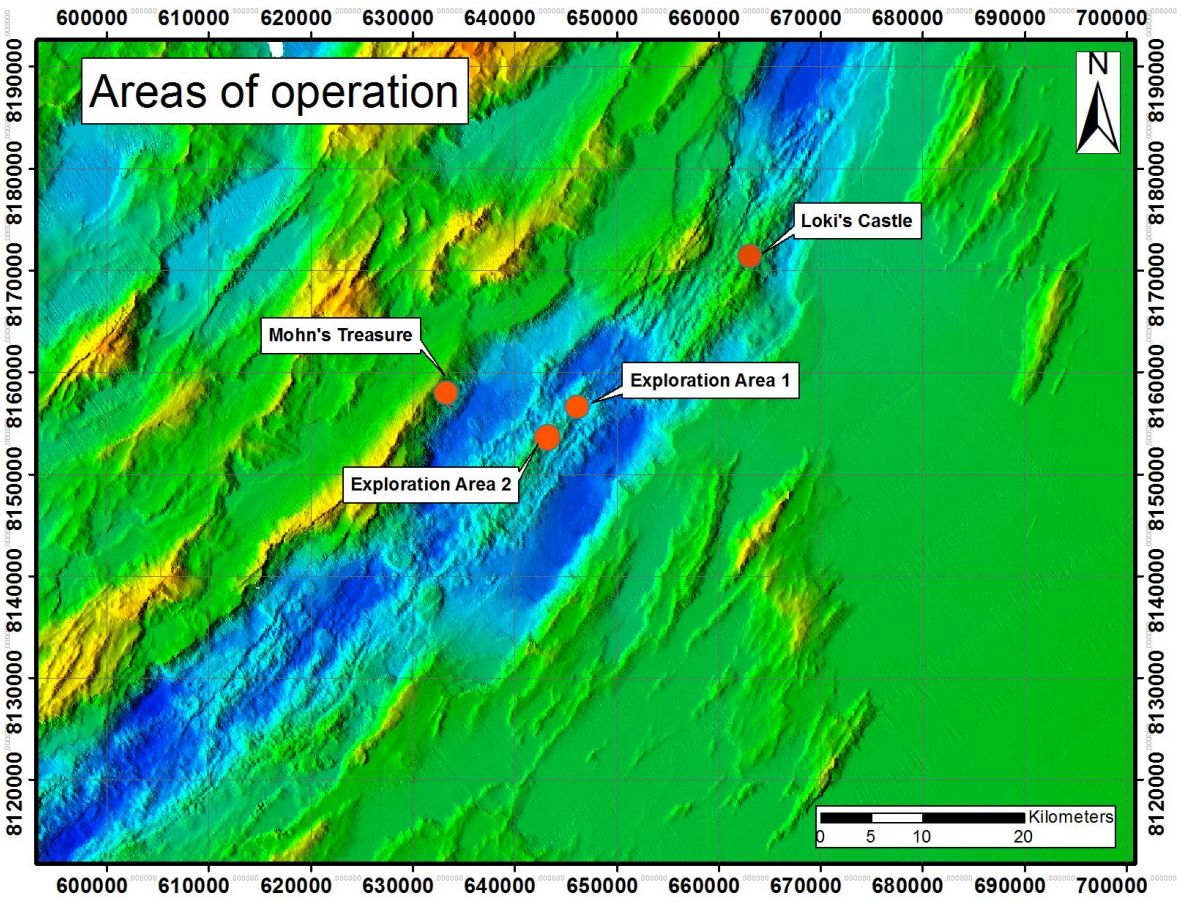

Figure 3.1: *Overview map of surveyed areas from MarMine 2016 Cruise. These areas include the Loki's Castle and Mohn's Treasure areas, alongside two exploration areas situated on an AVR further southeast on the ridge axis. Coordinates are in UTM31N/ETRS89, EPSG: 25381. Figure from MarMine Cruise Report, Ludvigsen et al. (2016).*

mineralogical characterization. The AUV was used to gather high resolution bathymetry and other data, including depth, temperature, methane, salinity and conductivity. In order to have a reference of a hydrothermal water column signature, the AUV was used at Loki's Castle to establish a base signature.

Two new technologies were tested during the cruise; an underwater hyperspectral imager (UHI) and a remotely operated core sampler (ROCS) (Ludvigsen et al., 2017). The UHI was mounted to the AUV and ROV during dives and demonstrated that the mineralized rocks have a clear hyperspectral signature, but further analysis is needed to confirm the results and continue to develop the technology. With the ROCS, it was a relatively simple task to recover drill cores from pillow lava basalt at 2600 m depth within a few hours, although the tool did have trouble with drilling in the mineralized chimney fragments found on the surface at Loki's Castle because of their loose and unconsolidated nature.

The AVR just south of the Loki's Castle AVR was determined to be an area of interest, termed exploration area 1 and 2, based on seafloor analysis and earlier studies, and was

surveyed with the AUV. Based on the collected high-resolution bathymetry, geological features were chosen to be inspected with the ROV. The seafloor surface displayed high variation in relief, defined by high peaks and ridges formed by faulting and volcanic activity, however, no clear evidence of hydrothermal activity was found during these surveys

In total seven ROV dives were carried out at Loki's Castle, divided between the two mounds and the surrounding area. Detailed video and photo recording were made of the chimney structures and the black smoker venting. Pillow lavas and sediments are present on the slope of the mounds, along with an increasing amount of chimney fragments toward the top of the mounds. Extensive sampling was conducted and point-based XRF analyses of the samples show detectable anomalies of Cu, Zn, Au and Ag.

The Mohn's Treasure area has previously been described as an extinct massive sulfide deposit (Pedersen et al., 2013) and was therefore subject to extensive study during the cruise in order to try to confirm this theory. However, after a several dives and extensive visual observation, no conclusive indications were found for the presence of an SMS deposit. Given that the area is supposed to be situated in a mass wasting event, it is very well possible that the potential deposit is covered by sediments. Overall, the area is largely sediment-covered, partially with extensive fields of crinoids. Locally, outcrops of basalt ridges and fields of basalt fragments are present. Some porous fragments were recovered that showed indications of fluid channels. An area with mysterious cave-like structures in the lithified sediments were also discovered. In order to investigate if perhaps sulfides are present in deeper layers, a gravity core sample was taken, however, no logging results are currently available.

.

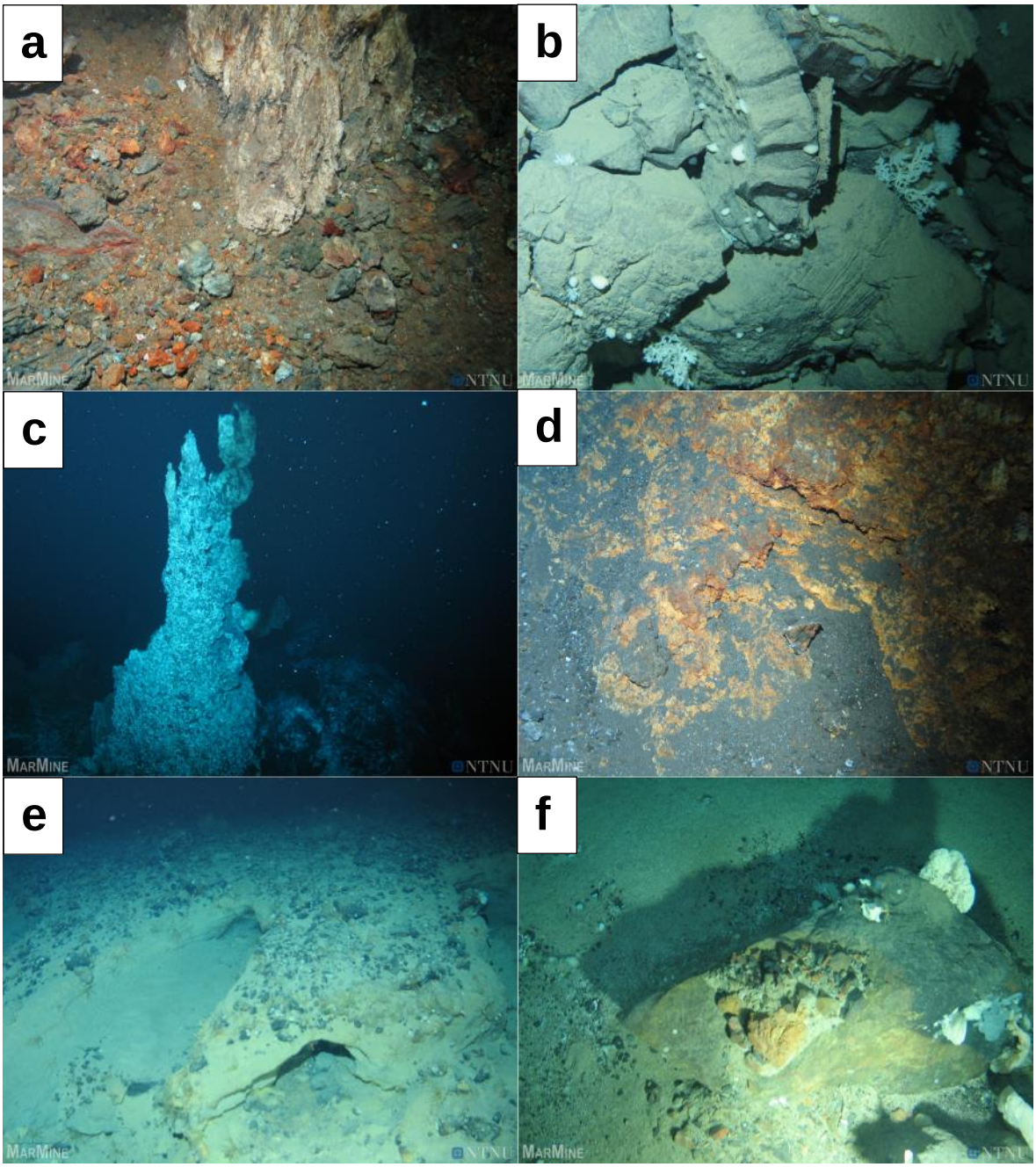

Figure 3.2: *Underwater images from the Mohn's Ridge, taken from a ROV during the MarMine 2016 Cruise.* ***(a)****chimney fragments at the top of one of the Loki's Castle mounds,* ***(b)*** *pieces of pillow lavas with sponges at the Loki's Castle area,* ***(c)*** *sulfide chimneys at the Loki's Castle vent field expelling high-temperature black smoker fluids,* ***(d)*** *the base of one of the chimneys at the top of the Loki's Castle mounds,* ***(e)*** *cave structures in partially solidified seafloor sediments discovered in the Mohn's Treasure area,* ***(f)*** *basalt fragments with sponges found on the sediment plain at Mohn's Treasure. Photos: NTNU/MarMine*

4. Theory

4.1 Morpho-tectonics of slow-spreading Ridges

Mid-ocean ridges have varying spreading rates and it is now very well documented that slow-spreading ridges (< 55 mm/yr) have a markedly different morphology than their fast-spreading (> 80 mm/yr) counterparts (Macdonald, 2001). The former typically consist of a deep axial valley and rugged flank topography, whereas the latter exhibit a much more regular flank topography on each side of an elevated central ridge axis (Macdonald, 2001). However, it has also been revealed that ridge morphology does not only depend on spreading rate, but also on magma supply and thermal structure of the ridge and underlying lithosphere (Dick et al., 2003).

The overall structure of slow-spreading ridges is characterized by steeply-dipping, inward facing normal faults as half-grabens structures, creating a "staircase"-morphology on the seafloor surface (Mutter & Karson, 1992). Typical for slow-spreading ridges are deep central valleys with discontinuous neo-volcanic zones in the form of axial volcanic ridges (AVRs), which mark areas of active volcanism along the ridge (Macdonald, 2001; Mutter & Karson, 1992; Smith et al., 1997). AVRs are typically elongated parallel to the axis, several tens of kilometers long, a few kilometers wide and a few hundred meters high (Searle et al., 2010). Furthermore, the valleys are bordered by a complex valley wall consisting of inward-facing fault scarps and terraces leading toward the ridge flanks where rugged terrain and topographic highs dominate (Laughton & Searle, 1979).

4.1.1 Magma Supply and Modes of Extension

Extension on mid-ocean ridges can be divided into two endmember categories; magmatic extension and amagmatic extension, giving rise to two distinct modes of lithospheric accretion: (1) accretion generated by primarily tectonic processes and (2) accretion by primarily magmatic processes (Buck et al., 2005; Cann et al., 2015; Escartín et al., 2008; Tucholke et al., 1998).

During periods of increased magma availability, lithospheric accretion is primarily accomplished by magmatism in the form of dike intrusions and lava flows, resulting in formation of AVRs and volcanic abyssal hills on the ridge flanks, caused by minor faulting and subsequent drift and transport of material within the valley onto the flanks (Cann et al., 2015). Amagmatic periods with less or no magma availability, on the other hand, are characterized by extension-accommodation along fewer, but larger normal faults, often accompanied by

formation of core complexes with little to no volcanic input (Cann et al., 2015; Escartín et al., 2008). Typically, at slower-spreading ridges, the ridge axis is marked by a central valley or trench, often 1 – 3 km deep, whereas fast-spreading ridges are marked by a continuously elevated central axial ridge (Figure 4.1). These morphological differences are commonly attributed to the overall magma availability beneath the ridge axis and the associated lava flows in the neo-volcanic zone, where magma availability is typically higher at fast-spreading ridges and lower at slow-spreading ridges (Escartín et al., 2008; Harper, 1985; Tucholke et al., 1998). The importance of magma supply in the formation of the axial morphology is also evident from the Reykjanes Ridge south of Iceland, where a very high rate of magma input has produced a continuously elevated axil high despite very slow spreading rates (20 mm/yr full rate) (Talwani et al., 1971). This is believed to be closely related to the ridge's proximity and interaction with the Iceland hotspot (White et al., 1995).

Furthermore, the magma supply at slow and ultraslow-spreading ridge segments is commonly believed to be discontinuous (Dick et al., 2003; Mutter & Karson, 1992) and perhaps even episodic (Harper, 1985). This theory is supported by the belief that at many segments with slow and ultraslow spreading rates, the surface morphology and spreading process are significantly controlled by mechanical extension and tectonic accretion rather than volcanic accretion (Buck et al., 2005; Tucholke et al., 2008). This gives rise to discontinuous AVRs in the axial valley, which should preclude the existence of long-lived and continuous magma chambers beneath the ridge axis (Mutter & Karson, 1992).

Discontinuous AVRs and a lack of transform faults that split the ridge into distinct high order segments are key characteristics of ultraslow-spreading ridges, typically found at full spreading rates < 20 mm/yr (Dick et al., 2003). Low magma supply thus leads to a surface expression on the flanks that commonly exhibits large amounts of normal faulting due to tectonically accommodated extension, with throws up to several hundred meters (Laughton & Searle, 1979) and formation of core complexes where lower crustal and mantle rocks may be exhumed (e.g. Escartín et al., 2008; Tucholke et al., 1998).

Because the magma availability beneath the axial valley at slow-spreading ridges is also thought to be temporally discontinuous (e.g. Harper, 1985; Tucholke et al., 1998), a period where the magma availability is limited will be followed by a period where it is more readily available. During these magmatic periods, discontinuous AVRs in the neo-volcanic zones will be built up and eventually broken down, following continuous extension. (Cann et al., 2015). Cut-off AVR slices, commonly 5 – 10 km wide, will subsequently be transported away

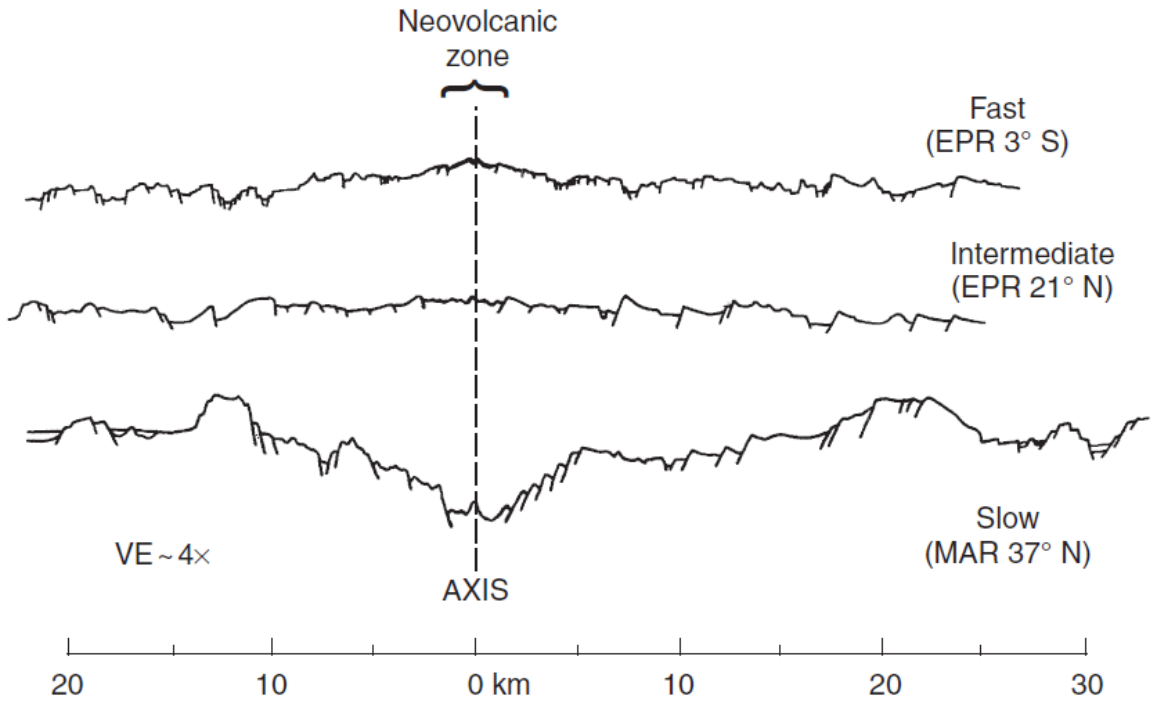

Figure 4.1: *Typical across-flank topographies of mid-ocean ridges, based on spreading rate. EPR: East Pacific Rise, MAR: Mid-Atlantic Ridge. Figure from MacDonald (2001).*

from the axial valley to the flanks, where they reside as volcanically constructed and parallelly oriented "abyssal hills" (Cann et al., 2015; Goff et al., 1995). As these structures are pieces of earlier AVRs, they are recognizable by similar morphology as the current valley floor and AVRs, typically expressing hummocky and knobby terrain, flat-topped volcanoes and lava flows on their outward-facing slopes (Cann et al., 2015).

Amagmatic segments, where extension may result in large-scale normal faulting and core complex formation, are also often found to display very different ridge flank morphologies compared to their more magmatically dominated counterparts (Escartín et al., 2008). Such segments commonly exhibit an asymmetrical style of spreading and lithospheric accretion, where one flank displays much more irregularity and topographic relief than its conjugate (Escartín et al., 2008), such as e.g. the northern Mohn's Ridge, where the western flank shows a distinctly different morphological style than the eastern flank (Bruvoll et al., 2009).

4.1.2 Formation of Detachment Faults and Core Complexes

Oceanic core complexes (OCC) are dome-shaped features at the seafloor where typically lower crustal and upper mantle rocks are exhumed as a result of prolonged slip and displacement along a single large-scale normal fault (Blackman et al., 1998; Tucholke et al., 1998). The resulting structures have also been termed megamullions (Tucholke et al., 1998) and are topographic highs on the ridge flanks characterized by distinctly corrugated domal surfaces and elevated residual gravity anomalies (Blackman et al., 1998; Canales et al., 2004), believed to be caused by thinning of the crust (Smith et al., 2008; Tucholke et al., 1998). Sampling on such surfaces often recovered gabbros, peridotites and serpentinites, providing evidence for the lower crustal and upper mantle origin of the domed structures (Okino et al., 2004; Pedersen et al., 2007; Tucholke et al., 1998).

OCCs can be regarded as the marine equivalents of continental metamorphic core complexes, both in terms of scale and structure (Tucholke et al., 1998), and are thought to be the rotated footwalls of large low-angle detachment faults, forming as a result of periods of amagmatic spreading related to limited or completely absent magma supply below the spreading center (Smith et al., 2008; Tucholke et al., 1998; Tucholke & Lin, 1994). Such cycles of alternating magmatic and amagmatic spreading are observed at slow and ultra-slow-spreading mid-ocean ridges and heavily influence which extensional mechanism is dominant (Buck et al., 2005; Harper, 1985). During periods of a readily available magma supply, the brittle-ductile transition rises beneath the axial valley, producing strong lateral temperature gradients that may result in fault localization in the weak lithosphere above the magma chamber (Harper, 1985). The result is extension accommodated by magmatic accretion of new lithosphere, along with strain partitioning across multiple small-scale normal faults (Escartín et al., 2008) that regularly “jump” inward, supposedly because it is easier to generate a new fault in the weak crust than it is to overcome the friction and strength of the old fault (Tucholke et al., 1998).

During periods of amagmatic spreading, the absence of a magma source in the shallow lithosphere leads to the fall of the brittle-ductile transition (Harper, 1985). The absence of a magma source results in a scenario where extension can no longer be accommodated by predominantly magmatic processes. In contrast to an amagmatic period, the lateral temperature gradients will be small and the strength of the lithosphere will be greater and relatively similar over large areas (Harper, 1985). Under these conditions a fault may just as well continue growing along the already established weakness zone instead of producing a new fault

(Tucholke et al., 1998). The relationship between magmatic-amagmatic cycles and the mode of spreading was also suggested by Buck et al., (2005), where numerical modeling of the modes of faulting during lithospheric accretion demonstrated that detachment faults have a high possibility of forming when only about 50 % of the total extension is accommodated by magmatic accretion, and that extension under such conditions subsequently will be taken up by large detachment faults initiated by normal faulting (Buck et al., 2005). These findings were confirmed and supported later by a similar study (Tucholke et al., 2008), where detachment fault formation was found to be favored when between 30 – 50 % of the extension were taken up by magmatic processes (Figure 4.3).

The morphology of detachment faults, or rather its system of associated structures and features (Figure 4.2) includes a so-called breakaway ridge, which marks the location of the fault where the detachment originally initiated as a steep normal fault (Canales et al., 2004; Smith et al., 2008; Tucholke et al., 1998). The breakaway ridges typically display outward-facing slopes as a result of fault rotation, with angles in excess of 20º being common (Smith et al., 2008; Tucholke et al., 1998). The core complex itself is restricted to a zone between the breakaway fault and subsequent termination closer to the ridge axis (Tucholke et al., 1998).

A question that arises when discussing the geometry of detachment faults is their nature at depth. Microearthquakes indicate that the faults extend into the mantle (Harper, 1985); however, what exactly happens to them at depth is unclear, as they for example may either flatten and mark a zone of transition between brittle and ductile deformation, or they may be planar and transition into aseismic ductile shear zones (Harper, 1985). Still, the observations of varying fault angles and the inferred progressive rotation of fault blocks as they are moved away from the ridge axis may indicate the general geometry of the faults at depth (Smith et al., 2008): Outward-facing slopes on the mid-Atlantic Ridge (MAR) are interpreted as being originally horizontal valley floor that has been progressively rotated with time, while inward-facing slopes represent the scarps of rotated normal faults (Smith et al., 2008). Fault rotation by as much as 20º is reported as close to the volcanic axis as 5 km, and because the distance over which this rotation has occurred is small, the normal faults must be steep at depth (Smith et al., 2008). These observations fit the generally accepted model of fault rotation (Buck, 1988) which explains the mechanism of normal fault rotation and predicts a shallow-dipping fault at or near the surface followed by a rapid steepening at depth (see chapter 4.4).

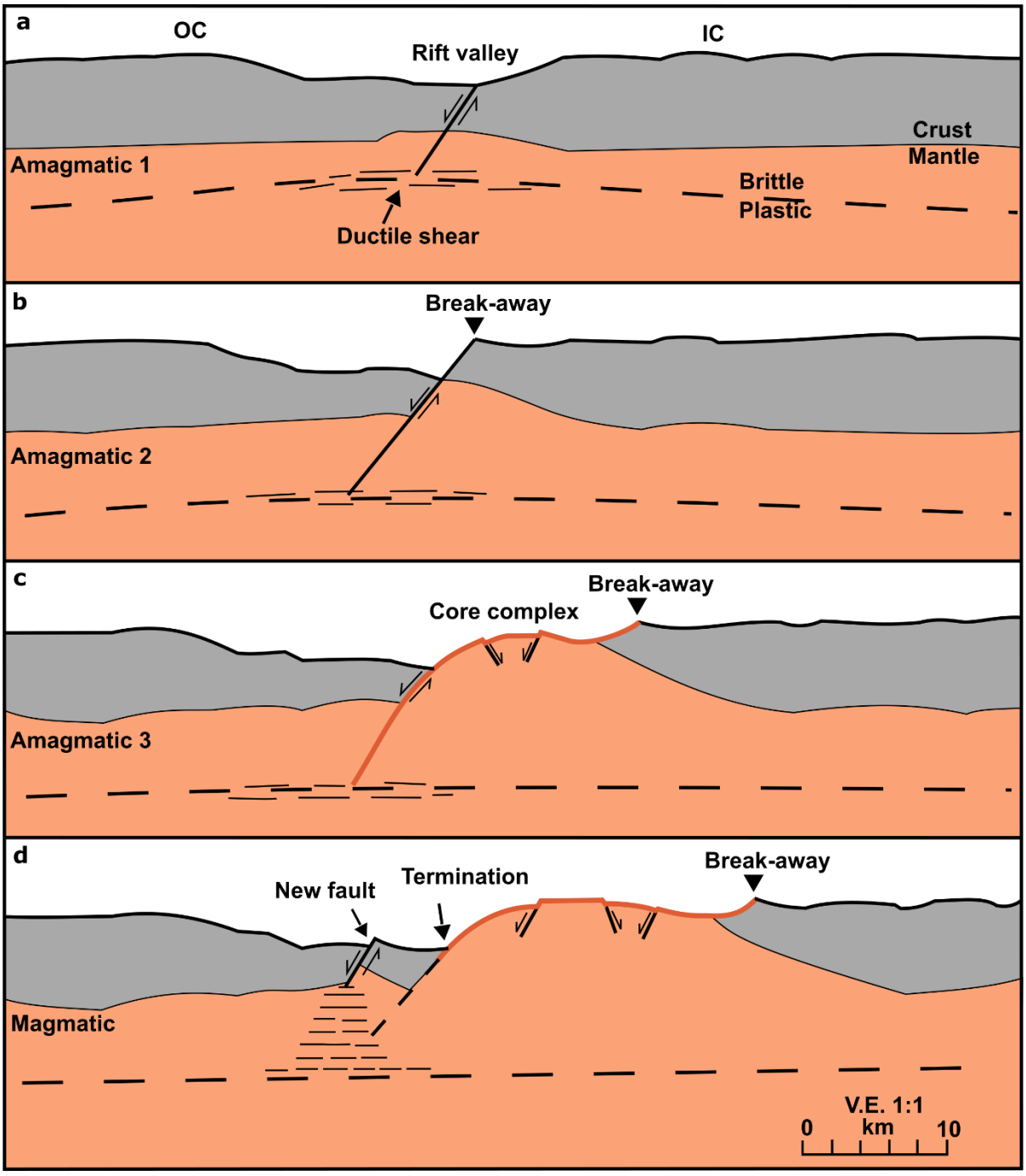

Figure 4.2: *Evolution and development of detachment faults and core complexes as envisioned by Tucholke et al. (1998)). **(a)**: A period of amagmatic spreading leads to the initiation of fault-accommodated extension. **(b)** Further extension is taken up by the same fault, producing a breakaway ridge and deeper-seated fault **(c)**: A longer period of amagmatic spreading leads to prolonged slip on the same fault and the subsequent exhumation of lower crustal and upper mantle rocks. The detachment fault progressively rotates to a sub-horizontal orientation as it moves away from the ridge axis, forming the dome-shaped core complex. Due to large degrees of extension and flexural rotation, the fault steepens beneath the ridge valley because of regional isostasy. **(d)** The detachment fault ceases to be active and the termination is formed once a new period of magmatic spreading has begun. A new minor normal fault forms at the ridge center and is through time move off-axis and replaced by another normal fault "jumping inward" in the process. Figure modified from Tucholke et al., (1998)*

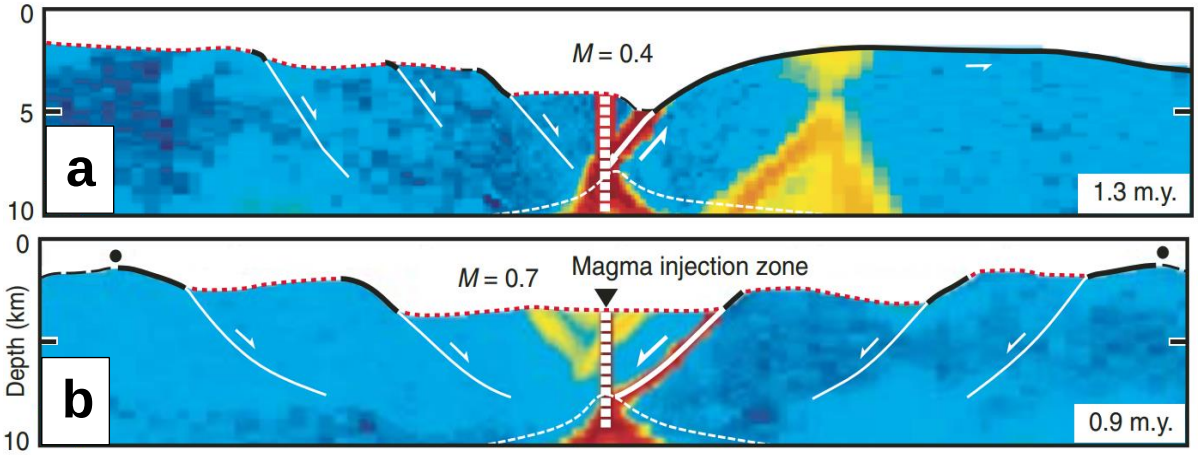

Figure 4.3: *Mid-ocean ridge morphology as a function of magmatic accretion.* ***(a)*** *A magmatic component of M = 0.4 favors asymmetrical flank development and formation of large-scale detachment faults. Significant amounts of extension are accommodated by tectonic mechanisms;* ***(b)*** *A scenario where the extension is primarily accommodated by magmatic processes (M = 0.7) results in symmetrical flank development with normal faulting on both side of the axial valley. Figure taken from Tucholke et al. (2008).*

Such detachment fault plane geometries have also been suggested (Smith et al., 2006) on the basis of flexural isostasy, but also by investigation and analysis of microearthquake hypocenters and seismic velocities at the TAG-deposit on the Mid-Atlantic ridge at 26 °N (de Martin et al., 2007). The recorded seismic events (magnitudes between 1 and 4) where found to fit onto a steeply dipping (~ 70°) plane just beneath the ridge axis, extending to more than 7 km below the seafloor (Figure 4.4).

Additionally, high seismic velocity anomalies where found over large areas on one of the flanks, interpreted as being caused by the uplift and exhumation of lower crustal and upper mantle rocks in the detachment footwall. The velocity anomalies were found to display a dip of roughly 20° on the flanks, suggesting the presence of a low-angle detachment fault on the flanks that turns into a steeply-dipping surface beneath the neo-volcanic zone at the ridge axis, with a total fault length of ~ 15 km (de Martin et al., 2007). This fits the geometry previously proposed by e.g. Buck (1988), Cann (1997), Smith et al. (2006) and Tucholke et al. (1998). Large-scale, deeply rooted detachment faults are also believed to be a key component for long-term hydrothermal circulation of black smoker fluids (de Martin et al., 2007), and on the MAR between the Marathon FZ at 13 °N and the Atlantis FZ at 30 °N, it has been shown that seven of eight known active or recently active hydrothermal vent fields are hosted at ridge sections with active detachment faults (Escartín et al., 2008).

.

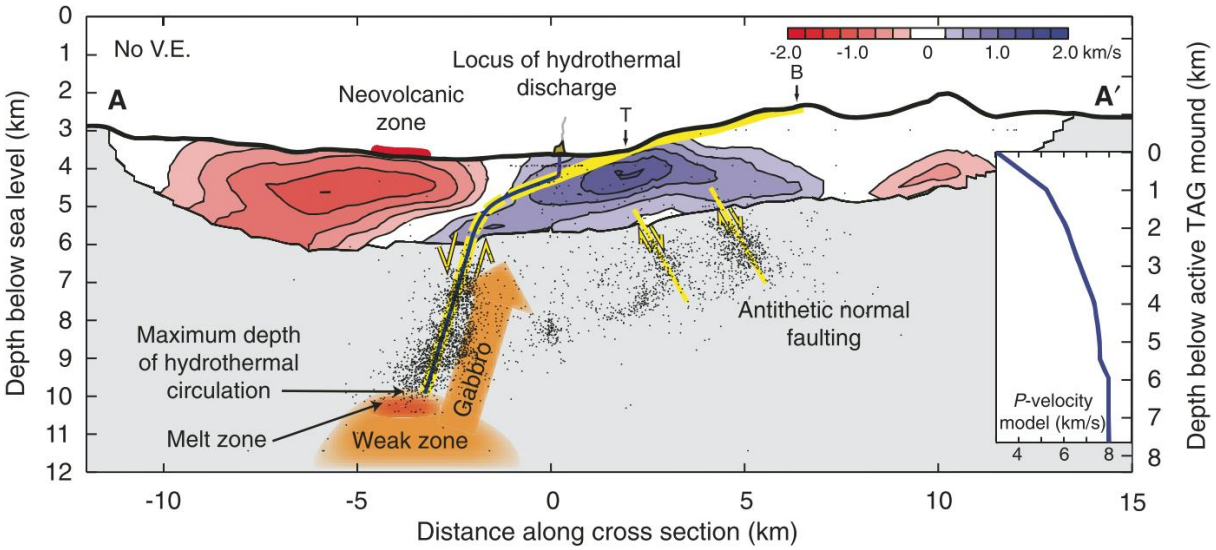

Figure 4.4: *Profile view of the structure of the TAG core complex area. Detachment fault (yellow) is inferred from high-velocity zone (blue) and seismic data. The earthquakes show a shallow dip toward the neo-volcanic zone before steepening beneath the ridge axis. The high velocity anomalies are interpreted as being caused by the uplift and exhumation of lower crustal and upper mantle lithologies in the footwall of the detachment fault. Red areas mark lower seismic velocities, interpreted as being upper crustal basalts. Figure from de Martin et al. (2007).*

4.2 Listric Faulting

The term *listric* was first coined by the Austrian geologist Edward Suess (1831 – 1914) when he described coal districts in France, Belgium and Germany (Suess, 1909, p.534-536). Suess observed that some of the faults in the districts were not purely planar (Figure 4.5), but displayed curved surfaces, flattening at depth. He recognized that they could not be simple planar faults and proceeded to call them *listric planes (greek:* listron – shovel*).*

The Oxford Dictionary of Geology and Earth Sciences defines a listric fault as " a curved extensional fault which characteristically flattens into a décollement horizon" (Allaby, 2013, p.343). Similarly, other authors have described listric faults as normal faults whose dip decreases with depth, resulting in a curved, concave-up geometry, often in a system of consecutively imbricated fault blocks or rollover anticlines (Figure 4.6) (Jackson & McKenzie, 1983; Shelton, 1984; Wernicke & Burchfiel, 1982). Listric faults curving into underlying décollement surfaces are often associated with sedimentary rifts and passive continental margins, where they, for instance, may act as mechanical boundaries offsetting sedimentary sequences from the underlying basement (Bally et al., 1981; Shelton, 1984). Despite being commonly associated with extensional environments, listric thrust faults have also been identified as part of convergent orogenic settings (Bally et al., 1981; Shelton, 1984).

It should be noted that in this thesis, the term *décollement* will be used for an underlying horizontal surface, to not cause any confusion with the frequent use of *detachment* in conjunction with detachment faults as large-scale normal faulting.

Most normal faults will eventually become listric due to rheological factors, a theory based on the influence of geothermal gradients and the inevitable rheological contrasts of the lithological layers as faults propagate to larger depths (Jackson & McKenzie, 1983; Shelton, 1984). The constraint that no voids should form during rotational motion of the faults further restricts the geometry of the fault blocks, from which it follows that most normal faults should

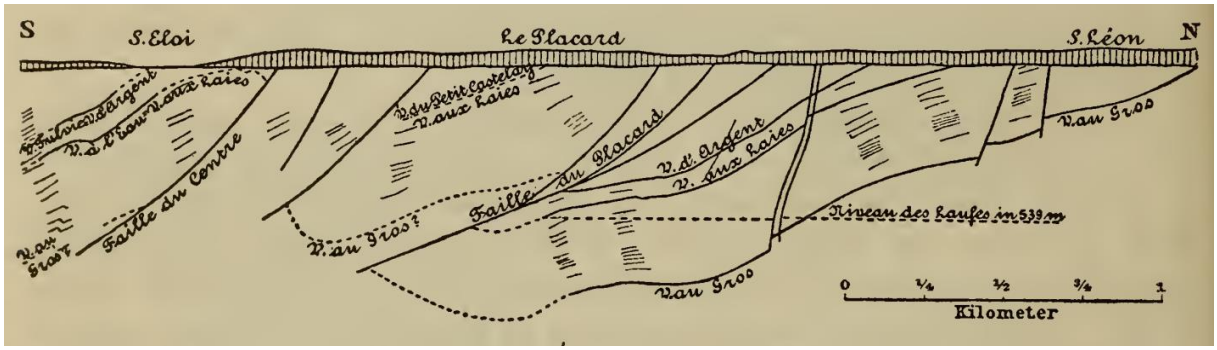

Figure 4.5: *Cross-section of the coal field from Saint Éloi to Saint Léon. South-dipping, curved fault surfaces were observed and described as listric planes. Figure from Suess (1909), p.534.*

be listric, especially if they are rotated (Jackson & McKenzie, 1983).

Listric normal faults have been described on active mid-ocean ridges (Karson & Rona, 1990) and ophiolite complexes (Roberts et al., 1993; Varga & Moores, 1985; Verosub & Moores, 1981). Zones of hydrothermal circulation at the TAG vent field were attributed to a transfer fault, or "accommodation zone", acting as a boundary between a segment with listric fault scarps and a segment with planar fault scarps (Karson & Rona, 1990). The listric geometry of the normal faults was inferred from the observations of rotated dikes and their overlying beds. Karson & Rona (1990) further suggested that this accommodation zone would allow differential extension and rotation between the fault segments which it bounds, resulting in increased permeability and facilitation of hydrothermal circulation.

Similar observations of tilted dikes and country-rocks have been reported at the Troodos Ophiolite Complex in Cyprus, along with observations of low-angle normal faults (Verosub & Moores, 1981). These observations were used to propose that large-scale block rotation is an important feature at oceanic spreading centers and that this probably happens along listric normal faults (Verosub & Moores, 1981). This was supported with observations from other extensional regimes, such as the listric faulting in the continental Basin and Range Province in the western United States (Verosub & Moores, 1981). Later, Varga & Moores (1985) described the spreading structure of the Troodos Ophiolite Complex to consist of listric and planar normal faults, which they proposed flatten at depth into a décollement within the upper parts of the gabbro section.

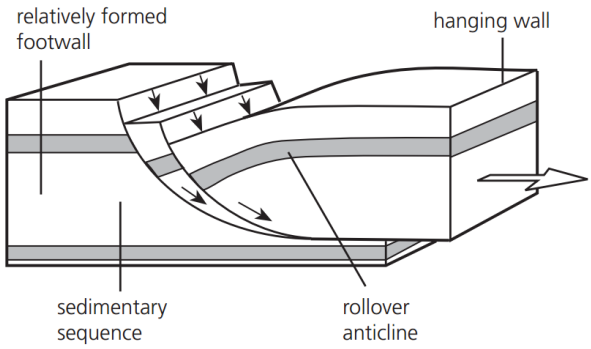

Figure 4.6: *Conceptual sketch of a listric fault. It characteristically flattens into a basal décollement upon which also subsequent fault blocks rotate and flatten into. The hanging wall sags down and forms a rollover anticlinal structure. Figure from Allaby (2013a).*

Observations of multiple generations of diking, where earlier dikes were tilted and later cut by vertical intrusions, were reported from the Lizard Ophiolite Complex (Roberts et al., 1993). Along with severe thinning of the crust (up to 40 %), this tilting was suggested to be caused by a period of limited magmatic extension along listric faults, who additionally also were proposed to provide the mechanism by which the presence of peridotites and gabbros commonly sampled at slow-spreading ridges could be explained (Roberts et al., 1993).

4.3 Hydrothermal Seafloor-Massive Sulfide Deposits

Ore deposits related to seafloor hydrothermal activity were observed for one of the first times in the late 1970's after the discovery of sulfides on the East pacific Rise (Francheteau et al., 1979), described as chimney structures with a porous structure and widespread small fluid channels. Due to the general similarities in type and style of metal assemblages of the recovered samples, the idea emerged that such deep-sea deposits could represent modern analogues of zinc and copper-rich deposits found in ophiolite complexes on land (Francheteau et al., 1979). Today, is it generally accepted that the deposits on land, so-called volcanogenic massive sulfide deposits (VMS), are in fact ancient hydrothermal deposits originally formed on the seafloor (Galley et al., 2007). However, most ophiolite complexes on land are not representative of mid-ocean ridge crust, but mostly fragments of back-arc extension related to subduction zones (Hannington et al., 2005). It is estimated that around 80 % of all VMS deposits were formed in arc-related environments, and almost half of the global VMS tonnage is believed to have formed during a short 340 My period of subduction and arc volcanism along Paleozoic continental margins (Hannington et al., 2005). Most ancient mid-ocean ridge deposits would also not have been preserved in the geological record because the earth's ocean crust is at most 150 My old (Allen & Allen, 2005a) due to their inevitable destruction in subduction zones, which would only leave a few ophiolite suites preserved (Galley et al., 2007; Hannington et al., 2005). Current black smoker venting at mid-ocean ridges represent a specific VMS type, namely the ophiolite-hosted Cu-Zn deposits, such as the Troodos Massif in Cyprus (Robb, 2005).

VMS deposits are an important source for zinc, copper and lead, but also silver and gold, and are typically found in lense-shaped polymetallic deposits, underlain by a "pipe" structure (Figure 4.7) often containing disseminated sulfide mineralization (stockwork mineralization), which represents the conduit through which the fluids have circulated (Galley et al., 2007). Because the ore genesis is controlled by the interaction between rock, fluids and heat, the VMS districts are often characterized by zones of alteration surrounding the deposits (Galley et al., 2007).

SMS deposits form in submarine volcanic settings where cold seawater is intruding into fractured crust, circulating through the crustal rocks while being continuously heated until it is expelled at the spreading centers at temperatures of up to 400 °C (Galley et al., 2007; Robb, 2005; Tivey, 2007). While circulating through the crustal rocks, the chemistry of the fluids is

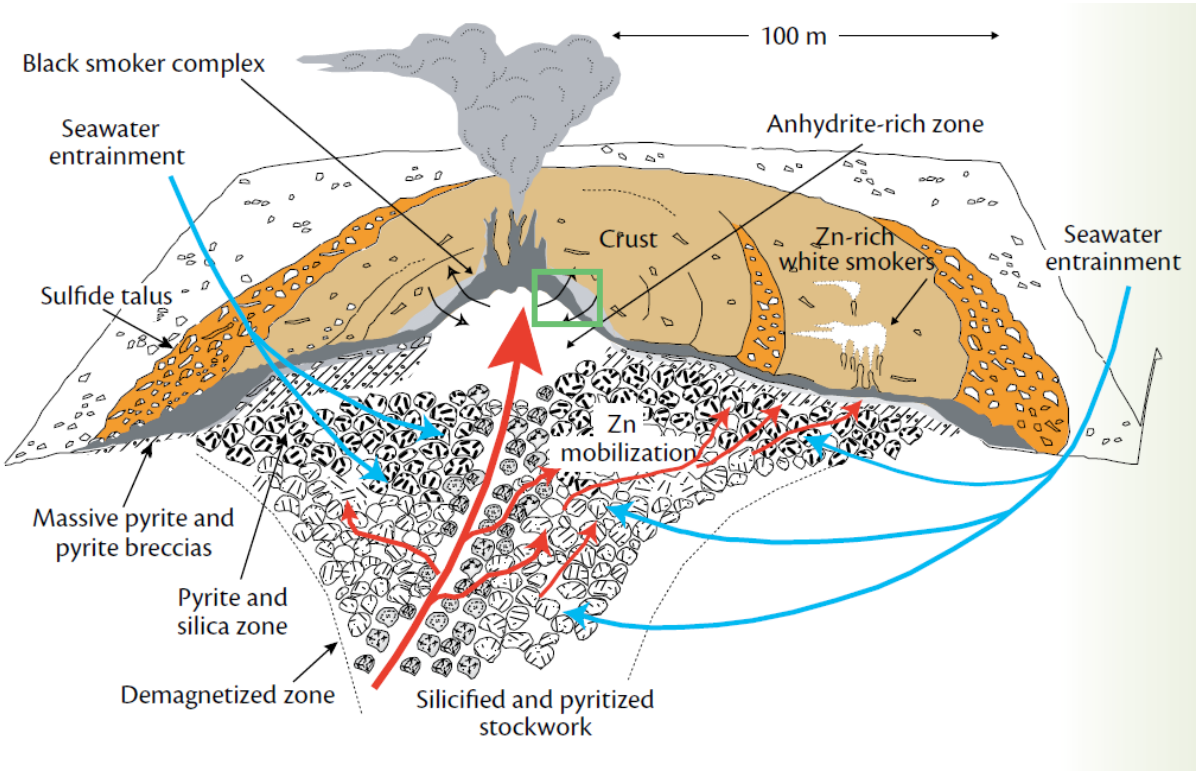

Figure 4.7: *Model of the structure of the TAG hydrothermal mound and underlying stockwork pipe, as envisioned by (Humphris & Tivey, 2000). The mound has a core of pyrite and chalcopyrite surrounded by a zone of anhydrite and Zn, caused by remobilization of the minerals. Image taken from (Tivey, 2007).*

gradually changed due to heating and interaction with the host rock, which produces fluids that are slightly acidic, anoxic and Mg-poor, relative to the seawater (Tivey, 2007). As the fluids pass closer to the heat source below the extensional axis, metals are leached from the rock and enriched in the fluids (Galley et al., 2007; Tivey, 2007). The hot fluids are buoyant and rise towards the seafloor, a process during which the fluids may separate into a low-salinity and vapor-rich phase (Tivey, 2007). This is thought to be the rule rather than the exception, as metals are believed to be transported as metal-chlorine complexes in the aqueous fluids (e.g. Tivey, 2007), and chlorine has a strong affinity for the vapor phase during phase separation (Alletti et al., 2009).

The continuous venting of metal-rich fluids at the seafloor surface leads to the build-up of several meter-high chimney structures during periods of active venting. After some time, they become structurally unstable and may collapse, due to erosion or faulting, and accumulate on a mound of sulfide ore upon which new chimneys form during following active periods (Galley et al., 2007; Humphris et al., 1995; Petersen et al., 2016). Generally, the metal source of the fluids is believed to be the rocks through which they circulate, which is supported by observations that different VMS deposits display matching metal assemblages and ratios as their associated primary igneous rocks (Robb, 2005). As such, mafic rocks will yield more Cu

and Zn, whereas more felsic rocks will gradually incorporate more Pb (Robb, 2005).

VMS deposits on land, and marine SMS deposits, typically show mineral and metal zoning related to the varying temperatures that have ruled during venting. This is typically characterized by an upward and outward radiating paragenetic sequence of *Fe* to *Fe-Cu* to *Cu-Pb-Zn* to *Pb-Zn-Ba* (Figure 4.8) (Galley et al., 2007; Robb, 2005). One way to envision this, is that the hydrothermal system is heating during its growth, where the fluid composition changes as a result changing temperature (Robb, 2005). In such a system, during early low temperature conditions (< 250 °C), the fluids are unable to dissolve significant amounts of metals and the result is a white smoker fluid expelling barite ($BaSO_4$) and anhydrite ($CaSO_4$) (Robb, 2005). As the temperature increases and reaches ~ 250 °C, the solubility of Pb and Zn as chlorine complexes is high, whereas Cu and Au are still poorly soluble, resulting in chimneys with mineral assemblages consisting of anhydrite and barite with sphalerite (*ZnS*), galena(*PbS*) ± minor gold (Robb, 2005). At temperatures of around 300 °C, the fluids are able to contain large amounts of Cu which will be deposited as chalcopyrite ($CuFeS_2$) in the stockwork zone and the base of the sulfide mound, while previously precipitated sphalerite and galena will be dissolved due to the high temperatures and reprecipitated further up the mound or away from it, in a process of "zone refining" (Galley et al., 2007; Robb, 2005). At even higher temperatures (300 – 350 °C), further chalcopyrite precipitation will be accompanied by Au and pyrite (FeS_2) (Robb, 2005).

Around 65 % of current SMS deposits form on mid-ocean ridges (Hannington et al., 2011), although considerable amounts of deposits are also found in arc-related settings. As slow-spreading ridges make up more than 60 % of the global ridge length, it has been estimated that over 80 % of global SMS tonnage should be located on slow-spreading (< 55 mm/yr) mid-ocean ridges (German et al., 2016; Hannington et al., 2011), where hydrothermal systems are often hosted in more tectonic rather than volcanic settings due to an overall lower availability of magma beneath the ridge axis. Hydrothermal systems on slow-spreading ridges also appear to produce larger, although fewer deposits than fast-spreading ridges due to a more stable structural environment and thus more long-lived fluid circulation, and also frequently display interaction with ultramafic rocks, leading to potentially high Cu concentrations (German et al., 2016).

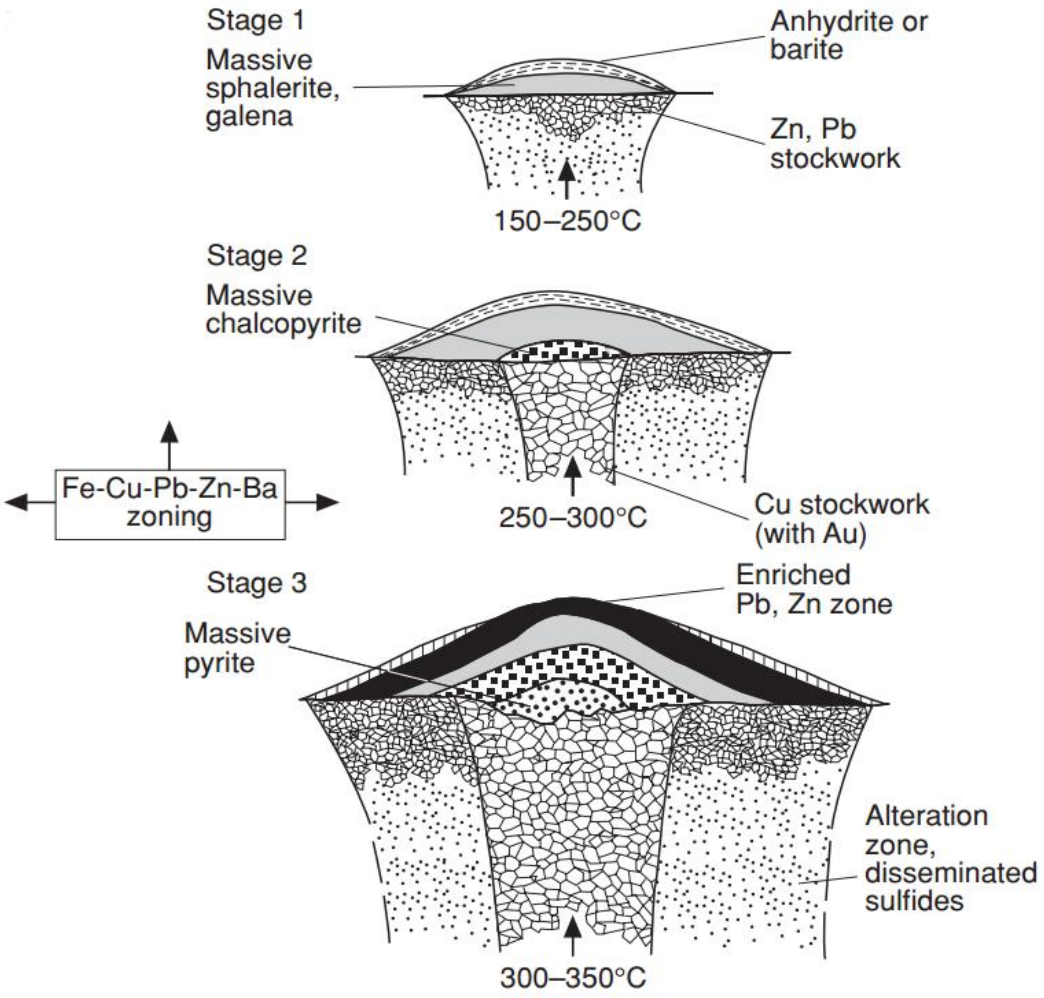

Figure 4.8: *Evolutionary model for hydrothermal sulfide deposits as described by Robb (2005). The deposit grows as the fluid temperature increases (from top to bottom) and results in distinct zoning, reflecting the solubilities of the different sulfide minerals. The final zonation will be the reverse of the solubilities due to progressive reprecipitation and subsequent zone refining. Figure from Robb (2005).*

4.4 The Mechanics of Fault Rotation

Metamorphic core complexes in continental settings are similar to their submarine counterparts in terms of scale and structure (Tucholke et al., 1998), meaning that the same challenges arise when trying to explain how lower crustal and upper mantle material has been uplifted several kilometers and juxtaposed with much younger rocks. One of the models often referenced (Cannat et al., 2009; Smith et al., 2008; Tucholke et al., 1998) investigated the effects of regional isostatic compensation to large offsets on rotated normal faults (Buck, 1988). This was done in response to the question of whether these observed large low-angle normal faults were initiated at those angles or if they were rotated from originally steeper orientations. Basic fault theory (Anderson, 1905) dictates that normal faults should initiate at preferred angles > 45°, typically at around 60°, simply because the maximum compressive stress ($\sigma_{1)}$ is assumed to be vertical and the least compressive stress (σ_3) is horizontal (perpendicular to the fault trace). The observed tilted fault blocks, both on land and in marine environments, however, cannot be explained by this model, because pure slip motion cannot result in rotation, only displacement (Verosub & Moores, 1981).

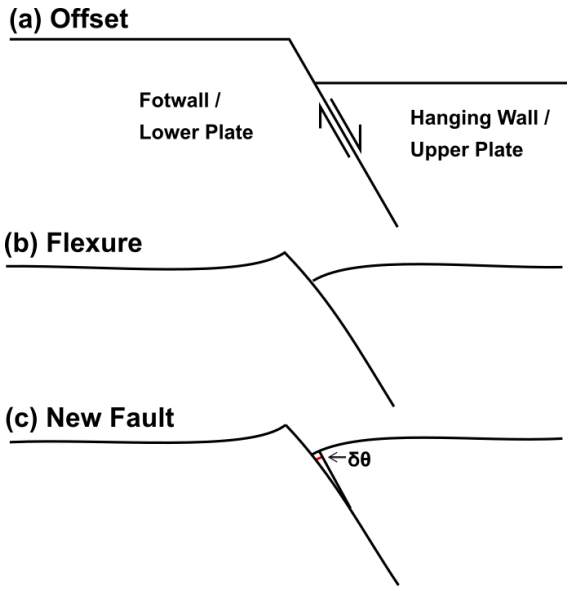

Figure 4.9: *The three principal steps of the flexural rotation model as described by Buck (1988).* ***(a)*** *A normal fault is initiated at a steep angle,* ***(b)*** *Continuous offset will cause flexure as a response to the topographic load, which leads to rotation of the fault,* ***(c)*** *The rotated fault is abandoned and a new fault is initiated. Figure modified from Buck (1988).*

The model presented by Buck (1988) tried to solve this by describing formation of low-angle detachment surfaces as the result of continuous offset of a steep normal fault with a starting angle (θ) (Figure 4.9). The wavelength of the flexural response is directly related to the flexural rigidity, or elastic thickness (T_e), of the lithosphere, which describes the thickness of a perfectly elastic plate (Allen & Allen, 2005b). The model further states that large-offset normal faults must rotate, which in turn will allow parts of the fault to flatten and be abandoned. This process will continue until the active fault has been rotated a given amount (δθ), at which point a new fault will initiate at the optimum angle and the cycle repeats. This new fault will intersect the old fault at a particular depth, called the nucleation depth (Buck, 1988). By modelling sediment infill, this model was able to

reproduce the structures and geometries observed at exposure sites of continental metamorphic core complexes, where an underlying low-angle detachment is capped by rotated listric fault blocks resting on top of it. (Figure 4.10).

Later, Buck co-developed another model (Lavier et al., 1999) using numerical methods to model large-scale low-angle oceanic and continental detachment faults. The results from this study state that in order to form such detachment faults, the presence of a relatively thin and cohesive brittle layer is required, because thick layers with small cohesion will result in multiple faults with small offsets and little strength reduction (Lavier et al., 1999). Fault rotation using this model and moderate strength reduction resulted in a single fault slipping at a high angle, followed by progressive rotation as a function of offset. After 15 km of extension, the fault is rotated to <20°, causing material to be drawn from the depth, assumed to represent lower crustal material (Lavier et al., 1999). The geometry of this modelled detachment fault is comparable with detachment geometries reported in literature (e.g. Escartín et al., 2008; Smith et al., 2008; Tucholke et al., 1998), and contains a breakaway ridge, domal surface and shallow-dipping detachment surface, before steepening beneath the ridge axis (Figure 4.11).

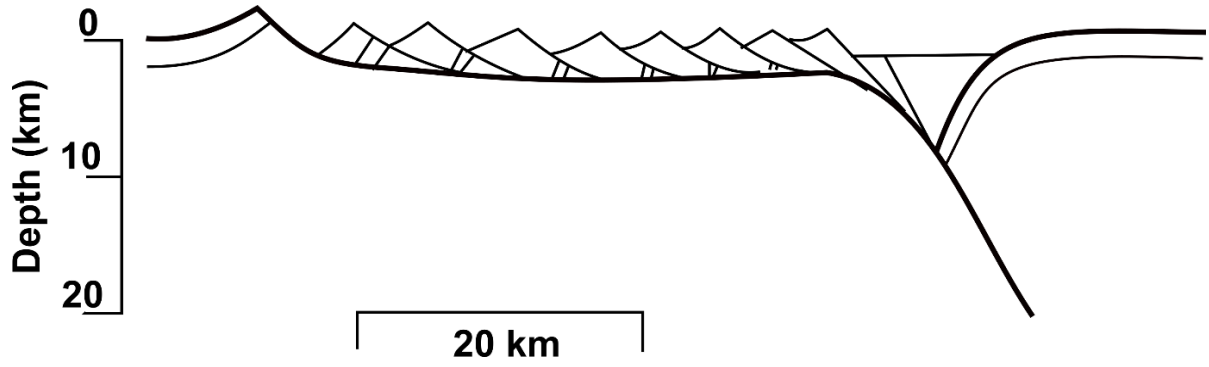

Figure 4.10: *Flexural rotation model of a metamorphic detachment fault using sediment loading. Initial fault angle of 60° and abandonment angle (δθ) of 10°. This model results in the rotation of a normal fault to a major low-angle detachment upon which sequential rotated, listric normal fault blocks rest. Figure modified from Buck (1988).*

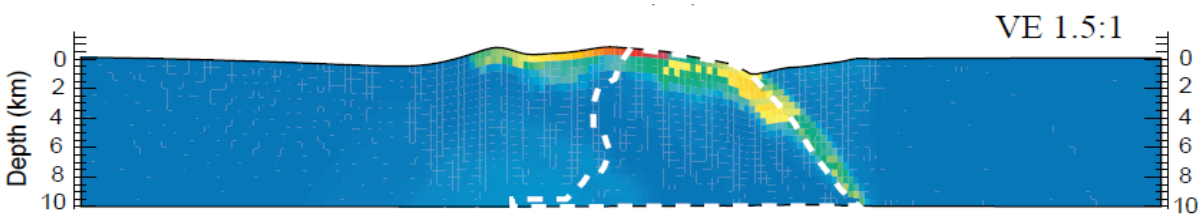

Figure 4.11: *Oceanic detachment fault after 27 km of extension modelled by Lavier et al. (1999). The model exhibits the same characteristic features of observed detachment faults on the MAR. Color change from blue to red marks increasing plastic strain. White dashed line marks uplifted lower crustal material. VE is vertical exaggeration. Figure taken from Lavier et al. (1999).*

4.5 Summary

There is an implied relationship between the extension and fracturing of the oceanic crust, the circulation of hydrothermal fluids through the appearing fractures and the associated formation of massive sulfide deposits. A strong and direct link has also been established between the flow rate changes of circulating hydrothermal fluids and the variability and frequency of earthquake swarms at nearby faults at the Juan de Fuca Ridge (Crone et al., 2010). Large, deeply rooted detachment faults are thought to be a key component for long-term hydrothermal circulation of black smoker fluids (de Martin et al., 2007; McCaig et al., 2007). The steeply dipping geometry of the fault beneath the axial valley would allow the fault to tap into a deeper-lying magma chamber, even during periods of limited magma supply, and extract heat in order to fuel long-lived hydrothermal circulation (de Martin et al., 2007). The importance of detachment faults as black smoker fluid pathways has also been suggested by McCaig et al. (2007), based on oxygen and strontium isotope analysis of rock samples recovered from a currently inactive detachment fault at 15°45'N. When studying the distribution of seismic events on the slow-spreading MAR, it was found that seismic events are overall more numerous and appear concentrated at asymmetric segments compared to their symmetric counterparts (Escartín et al., 2008). De Martin et al. (2007) showed through seismic event studies at the TAG core complex that active detachment fault surfaces are identifiable at depth by a focusing of seismic activity. In addition, between the Marathon FZ at 13°N and the Atlantis FZ at 30°N at the MAR, seven of eight known active or recently active hydrothermal vent fields are hosted at ridge sections with active detachment faults (Escartín et al., 2008), further strengthening the correlation between these elements. Detachment faults and the resulting core complexes may be of particular importance due to the involvement of ultramafic rocks, which may result in higher Cu grades in hydrothermal deposits (German et al., 2016; Petersen et al., 2016). Slow, and ultraslow-spreading ridges in particular, are believed to be formidable environments for the formation hydrothermal deposits due to a stable structural environment with slow spreading rates, allowing for prolonged circulation and build-up of sizeable deposits (German et al., 2016). An intriguing aspect with this is that, while at slow-spreading ridges anomalous Cu grades are achieved by uplift or exhuming of ultramafic rocks by deep-seated detachment faults, the crust at ultraslow-spreading ridges is much thinner, potentially allowing easier and more widespread fluid interaction with ultramafic lithologies and enrichment of Cu (German et al., 2016).

5. Materials and Methods

5.1 Available Data

- **Bathymetric Data:** Bathymetric data was collected for the NPD (Norwegian Petroleum Directorate) in 2000 and 2001 by the Fugro Geoteam. This data is available in a XYZ format containing easting, northing and depth in projected coordinates of the UTM31N system (ETRS89 UTM 31N, EPSG: 28531). These data are ship-acquired and have a gridded resolution of 100x100m.
- **Seismic Reflection Profiles:** Data for five seismic reflection profiles were available for interpretation, acquired by the University of Bergen in 2001 with the R/V Håkon Mosby. These data have already once been interpreted and published by Bruvoll et al. (2009), although in a slightly different research context, with a larger focus on sedimentation and burial history. The profiles are located in the Mohn – Knipovich bend and extend from the western flank across the valley over to the eastern flank (Figure 6.1). In this study, the profiles were analyzed and interpreted using Petrel 2015.
- **Seismic Earthquake Event Data:** Seismic earthquake event data has been gathered for the study area from the reviewed regional database of NORSAR. (NORSAR, n.d.) In total 442 events were recorded and reviewed by seismologists for a period from November 1998 to December 2016. These data include meta information such as the time and depth of each event, magnitude and error ellipsoid. The data are provided using WGS84 decimal degrees coordinates and were transformed to UTM31N projected coordinates using a developed Python code. The data were interpreted using ArcGIS and LeapfrogGeo.

5.2 Analysis of Seafloor Bathymetry

To visualize the study area, a digital terrain model (DTM) will be used. Terrain modeling is a procedure of quantifying the earth's surface by utilizing a mix of geosciences, mathematics, engineering and computer sciences (Pike, 2002). Often the terms DEM (digital elevation model), DMS (digital surface model) and DTM are used alongside each other and may cause confusion, however, they do not necessarily describe the same thing. A DEM, in terms of geographical information systems (GIS), is a generic term for a raster-based dataset (gridded data) describing height relative to a reference surface (commonly mean sea level) with one elevation value, regardless of its source, in each cell (Hirt, 2014; Podobnikar, 2005). A DTM on the other hand is typically a representation of the elevation values of the terrain or ground (Hirt, 2014), and sometimes may include other topographic elements (morphologic variables) derived from the elevation values of the terrain, such as slope, aspect or curvature (Florinsky, 2012). A DSM is also a representation of elevation, but typically represents the elevation of the first surface reflection when acquiring the data, including objects such as trees and buildings (Hirt, 2014).

In order to describe the topography by means of a DTM, morphometric (topographic) variables or attributes are used to describe a given surface (Florinsky, 2012). For analysis of geological landforms and objects, some very essential variables are used and described further below. For computation and visualization QGIS and ArcGIS will be used.

5.2.1 Morphological Variables

There are a multitude of different types of morphological variables, all of which have areas where they are particularly useful (Arrell et al., 2007). Still, it is typically slope, aspect and curvature, meaning first and second derivatives of the elevation, that remain the most used variables (Evans 1972 in Arrell et al. 2007). Since slope and curvature are derivatives, they describe the change of the variables upon which they are based and as such, slope describes the effectiveness of gravity on a surface, while curvature controls the acceleration or deceleration of a flow on a surface (Arrell et al., 2007). Elevation, slope, aspect and curvature are the fundamental variables in geomorphometry (Evans, 2005) and by using GIS software, it is a simple task to derive these variables from a DEM for terrain analysis.

5.2.1.1 Aspect

Aspect (Figure 5.1a) describes the direction that a given surface is facing (Evans, 2005). The aspect values in ArcGIS are calculated by moving a 3x3 cell grid over the DEM and

calculating the direction of the largest change of elevation values. Aspect is given as degrees from 0 (directly north) going clockwise to 360 (north again). Horizontal surfaces receive a value of -1.

5.2.1.2 Slope

Slope (sometimes called slope gradient) (Figure 5.1b) is an angle, usually in degrees but can also be given in percent incline, between a tangent plane and a horizontal plane at a given point (ESRI, 2016; Evans, 2005). The ArcGIS documentation further explains that their algorithm finds the largest possible change between a value and its neighboring cell, determined by a 3x3 cell grid, meaning that the function finds the largest slope between a given cell value and its eight neighboring values. The lower this value, the flatter the surface. The higher the value, the steeper the surface.

5.2.1.3 Hillshade

A hillshade (also called shaded relief) (Figure 5.1c) is usually a grayscale representation of a surface, where the sun's position has been taken into consideration in order to generate shadow effects in the landscape (ESRI, 2016). Hillshade maps can be used to enhance and underline topographic and elevation-related elements by illuminating the features from different angles and heights. Such hillshade maps have been proven to be very powerful tools for the interpretation of structural geological features, as demonstrated by Onorati et al. (1992). Here, using a hillshade map, most faults previously identified by traditional mapping were also found and identified on the hillshade map, demonstrating it to be a valuable tool for the identification of fault structures (Onorati et al., 1992).

5.2.1.4 Curvature

Curvature (Figure 5.1d) is the second derivative of elevation data and the first derivative of slope, and describes the acceleration and deceleration of flow on a surface (Arrell et al., 2007). Two primary types of curvature are commonly used: Profile curvature (K_V) and plan curvature (K_H), or a combination of both (Evans, 2005; Heywood et al., 2006). Profile curvature describes vertical changes in slope and is therefore suited to visualize terraces or plateaus in the landscape, while plan curvature describes horizontal change and is therefore suited to display ridges and valleys (Evans, 2005; Florinsky, 2012; Heywood et al., 2006). They are usually represented as greyscale rasters with values ranging from -1 to 1, where often a negative value indicates concavity and a positive value indicates convexity, although this may vary depending

on the author (Florinsky, 2012). In ArcGIS for example, profile curvature is shown as negative convex and positive concave, while plan curvature is shown as positive convex and negative concave. Because the values of a curvature map are often very small, they are sometimes multiplied by 100 to make the interpretation and potential reclassification easier. ArcGIS is among the softwares that do this.

5.2.2 Workflow and Procedure

The procedure presented below represents the general workflow for deriving morphometric variables, tweaking their symbology and interpreting them based on general geological knowledge. Many authors have used similar methods, among them Florinsky (1996) and Mallast et al. (2011). The procedure can be divided into four main steps:

1. **Smoothing the imported DEM**. This is done to reduce the sensitivity of the applied algorithms to random noise. This filter is often a Gaussian Filter which in essence "blurs" the image, and while this may reduce resolution and detail, it often outweighs the disadvantages as it removes noise from the DEM that could impact the visibility and interpretability (Mallast et al., 2011).
2. **Applying algorithms.** All desired algorithms are applied to the smoothed DEM (e.g. hillshade, slope, aspect, curvature).
3. **Tweaking the symbology.** All the applied algorithms return grayscale images, which are not necessarily informative unless tweaked to a suitable representation for the user. As such, specific colors are used to represent values, and some are even omitted or made transparent, leaving only those of interest visible.
4. **Interpreting and tracing features.** This is the last, but most important step, as it combines all produced maps into one interpretation based on geological knowledge and morphometric theory, and as such it is both an interpretation and quality assurance.

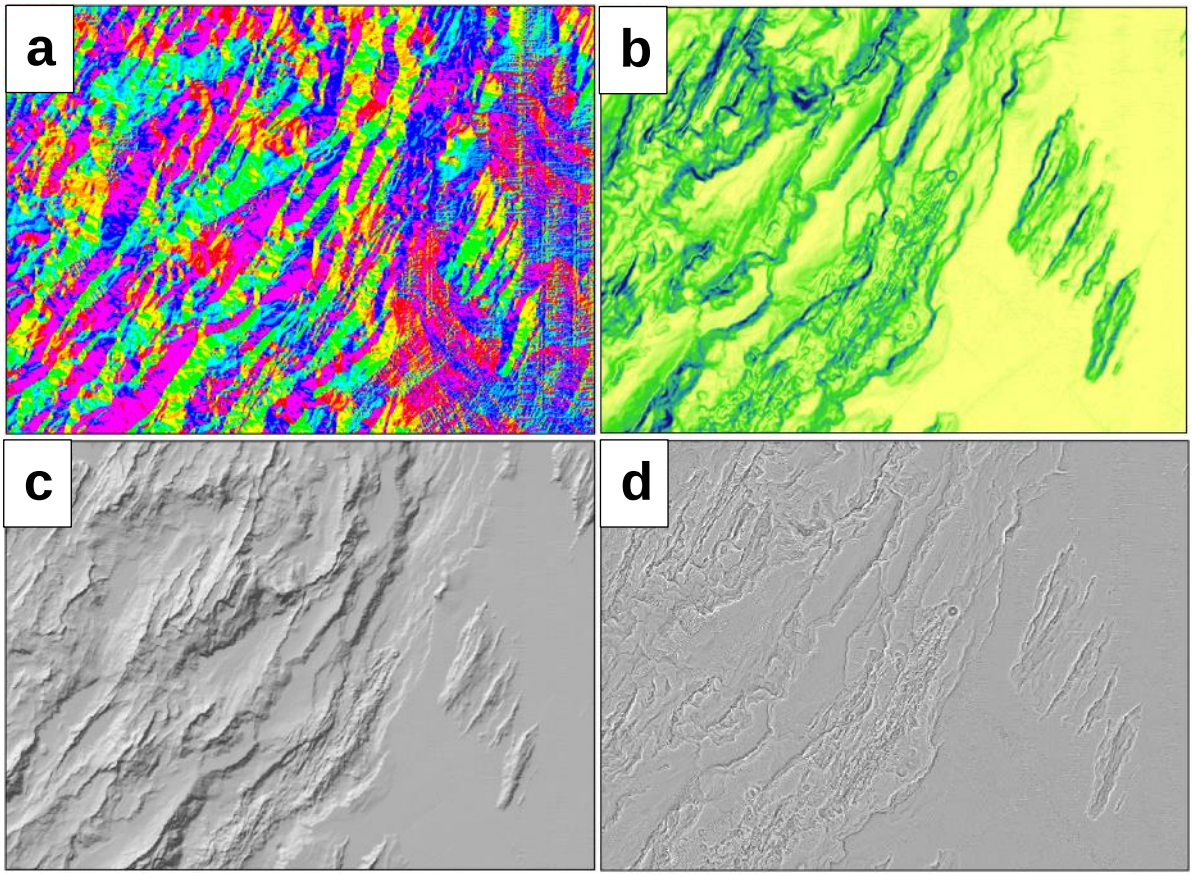

Figure 5.1: *A visual overview of morphological variables that can be derived from elevation data and be used for surface analysis. The images show the same area.* ***(a)*** *Aspect, green faces east, pink faces west* ***(b)*** *Slope, blue is steep, yellow is flat,* ***(c)*** *Hillshade,* ***(d)*** *Profile (vertical) curvature.*

5.2.3 Identification of Surface Structures

Based on theoretical background and previous studies of the morphology of slow and ultraslow-spreading ridges, the surface of the study area will be investigated and analyzed. Different geological structures on the ridge have different morphologies and surface expressions, which can be used as criteria for their identification. Below follows a brief description of the attributes and characteristics used to identify the respective structures on the DTM.

5.2.3.1 Normal faults

Tectonic structural interpretation on mid-ocean ridges is a relatively straightforward task, because there essentially are only two major geological processes which control the surface expression of the seafloor – tectonics and volcanism (Dauteuil, 1995). This comes in addition to the already known tectonic regime and spreading direction, which establishes an expectation for the orientation of tectonic features. Normal faulting will thus be visible on the surface due to vertical throw being expressed as linear features approximately parallel to the

axial trend of the ridge. A simple visual interpretation of a hillshade map combined with slope, contour lines and curvature to find the scarps is therefore a powerful set of tools for analysis of faults on the surface. Aspect maps can be used to determine where scarps are located and which direction they face.

5.2.3.2 Abyssal hills

As abyssal hills are caused by normal faulting, many of the same principles as for default normal faulting apply here. However, abyssal hills are typically characterized by volcanic features on their outward-facing slopes, as they are formed by faulting and subsequent lateral displacement of axial volcanic ridges. These features are often volcanic cones, lava flows and a generally hummocky and knobby terrain, whereas normal faults are often relatively unaffected by volcanic influence and typically show smoother outward-facing slopes, characterized by a lack of these volcanic indicators. Contour lines are effective tools for visualizing potential differences in inward- and outward-facing slope angles, as more densely spaced contours indicate steeper terrain (Sloan & Patriat, 2004). As such, differently spaced contours on the inward and outward-facing slopes could be indicative of abyssal hill ridges.

5.2.3.3 Oceanic Core Complexes and Detachment Faults

Detachment faults are expressed at the surface by dome-shaped core complexes and thus, by identifying the latter, one will be able to infer the associated former. The identifying criteria for core complexes are derived from established descriptions in published literature (e.g. Smith et al., 2008; Tucholke et al., 1998; Whitney et al., 2013) and include a few key elements: (1) An elongate breakaway ridge with an outward-facing slope, oriented parallel to the ridge axis, representing the initial steep normal fault which has been rotated, (2) a dome-shaped, corrugated or non-corrugated central topographic high constituting the core complex itself, which may or may not be covered by rafted blocks and (3) a basinal structure, because according to the flexural rotation model, a sufficiently rotated fault should result in a flexural basin on the off-axis side of the breakaway ridge in order to compensate flexure. Because the dome-shaped topographic highs often stand out from other more linear features on the seafloor this, element will often be identified first, after which the remaining factors will be checked.

5.2.3.4 Axial Volcanic Ridges

AVRs are simple structures to identify as they stand out in the otherwise deep and depressed central axial valley floor as elongate and rugged ridges. Due to overall limited magma

supply on slow and ultraslow-spreading ridges, the AVRs will be discontinuous along the axis and represent local foci of magma upwelling, resulting in the pronounced build-up of axial ridges. These are typically elongate and parallel to the ridge axis, displaying distinct volcanic terrain with flat-topped volcanoes, craters, lava flows and hummocky and knobby terrain.

5.3 Seismic Interpretation

The primary objective of the seismic interpretation is to identify fault planes beneath the seafloor, because this is not possible using bathymetric data. To accomplish this, it is often helpful to identify seismic horizons prior to faults.

In its simplest terms, the identification and tracking of horizons is based on the identification of laterally continuous reflectors. These represent geological timelines of the same event, and a tracked horizon should thus represent an event that has the same geological age throughout its extension. The key to identifying actual timelines is to ensure that the mapped reflectors are laterally (semi) continuous and pronounced from one bounding surface to another throughout the seismic section, i.e. easy to trace. The seabed reflector is an example of a reflector that is often continuous over large extents and easy to identify because it is capped by the water column instead of sedimens. This yield a clear and easily identifiable reflector. In this study, the seabed reflector and the transition from sediment to basement are of primary interest as they effectively delimit the vertical extent of the sediment package.

Faults are visible in seismic sections as systematic discontinuities in intervals of otherwise laterally continuous reflectors, usually represented by vertical offsets of the seismic reflections. Picking reflectors across such fault planes can be relatively simple when the resolution is high and the image is clear. However, where this is not the case, correlation across discontinuities can be difficult and may require the use of other aids to estimate where the reflector should continue. For example, in the case where a fault is easily mapped from a visible offset in reflector A, but the same discontinuity is not visible in a lower-lying reflector B, the interpreter can use the offset in A and base his interpretation on this when mapping on B.

5.4 Analysis of Earthquake Data

The seismic data pulled from the regional database of NORSAR has varying degrees of uncertainty to it. Most of all, the positioning of the events in question has an overall large error ellipsoid, which is the area given by the major and minor axes to describe the probable geometrical shape within which the event is located. The median errors for the major axis,

minor axis and overall error ellipsoid of the epicenters are 44.5 km, 17 km and 2400 km^2, respectively, and their positions are therefore not sufficiently accurate to derive any conclusions of seismic activity in smaller areas, e.g. particular features, or subsurface geometries of particular faults. Instead, they were used for spatial statistics computation to derive more general information about the seismic activity on a larger scale. These results have to be used with caution, however, as their source data still retains its inaccuracy.

For the purpose of applying spatial statistics in Leapfrog, the data were projected onto the mesh surface, disregarding Z-components at large depths below the seafloor. This is done because the spatial statistics calculation was to be visualized on the seafloor mesh; however, the finished calculation would utilize the position of the source data as its center and "radiate" outward from this point resulting in sub-optimal visualization on the surface for data positioned at very large depths. This challenge is solved by projecting the points onto the surface, but introduces data that is not necessarily appropriate for describing processes at depth.

The finished analysis is obviously affected by the parameters applied during the process (Figure 5.2). The distance function does not give much flexibility as it is a simple equation describing the distance between each point on the mesh surface to the nearest seismic event point. Visualization of this can be altered by changing the color map and thus the ranges of values included by each color group, but this does not change the fundamental, quantifiable result, only the presentation of it.

On the other hand, the spatial statistics calculations have multiple statistical parameters which influence the result and need to be chosen adequately. What follows is a brief overview of the parameters from the Leapfrog Geo manual and the reasoning for why a given value was chosen. It should be mentioned that choosing specific values as parameters during this process is arbitrary because there is no expectation, reference or correct answer for what a parameter should be. As such, the process is characterized by conservative changes of the default parameters.

The parameters are: (1) the *interpolant type*, where in this case a spheroidal function was used instead of a linear function because it is expected that with increasing distance, the influence of the data should become zero, (2) the *sill*, defining the range at which there ceases to be any correlation between the data. As there was no other data to help define the value of the sill, the parameter was given the value of the variance of the data, which in this case was 0.7, (3) the *base range*, defining the distance at which the interpolant value is 96% of the sill, (4) the *alpha*, which determines the steepness of the interpolant curve and thus how fast the interpolant value reaches the sill, effectively determining how heavy points at a given distance

should be weighed. Because earthquakes in the crust that occur close to each other should be more related than those that occur at larger distances from each other, a lower-than-default value was chosen to emphasize this relationship, (5) the *nugget*, which represents local variations or anomalies in the data. Choosing a higher nugget value means to smoothen the data and emphasize the average values of neighboring points. Without any expectations of what values neighboring points should have, however, choosing a nugget value is arbitrary. The result did not change significantly for values between 0 and 0.1, so a value of 0.05 was chosen.

Due to the inaccuracy of the source data, the result from this analysis is merely a general indicator and is not sufficiently accurate to say something about smaller, particular areas. They can, however, be used to infer the general seismic activity for a larger area and therefore be used in conjunction with other data to reduce the uncertainty.

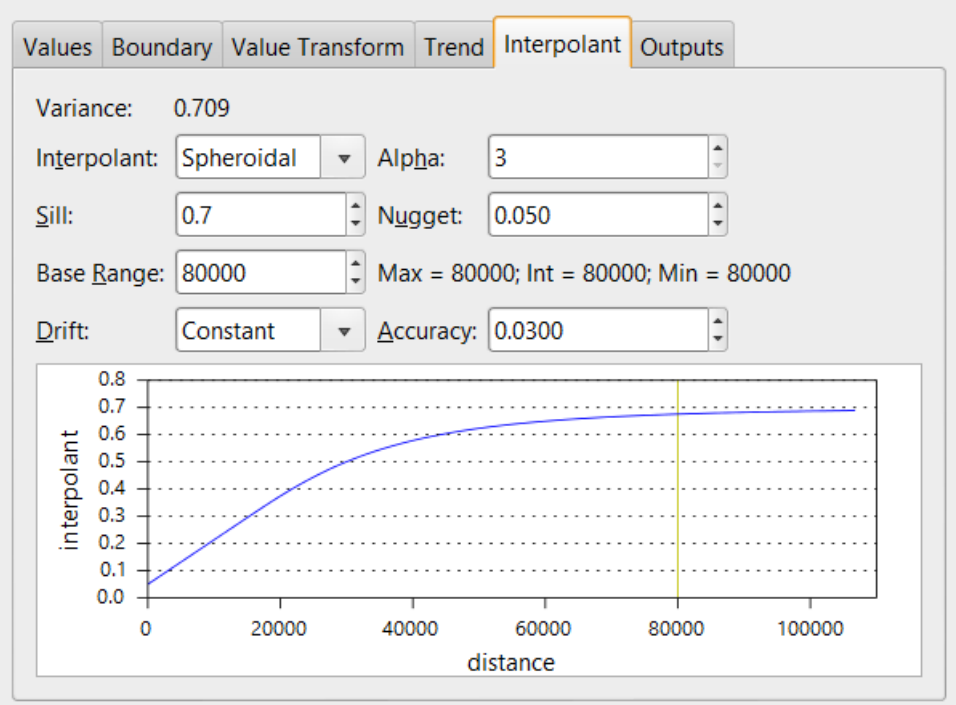

Figure 5.2*: Parameters used for spatial statistics. The initial steepness before it flattens it given by the alpha. The base range (80 000) represents the point at which the interpolant value on the y-axis reaches 96% of the final value of the sill (where the curve flattens horizontally).*

6. Results

6.1 Morphological Analysis

The surface morphology of the ~250 km of the northern Mohn's Ridge and its transition into the Knipovich Ridge has been analyzed using GIS tools on a gridded DTM. The analysis shows that the ridge displays a marked morphological asymmetry across its flanks, particularly in the transitional area between the two ridges. The western flank is here characterized by numerous and irregularly distributed major and minor faults and dome-shaped topographic highs, whereas the eastern flank is marked by more regularly spaced faults, delimiting elongate abyssal hills that were cut off within median valley before being transported to the ridge flanks. A morphological change of the ridge is also visible from north to south. Thirteen elevation profiles have been placed for surface analysis and comparison of different areas along the ridge. For comparative reasons, three of these profiles (2, 3 & 4) were placed so that they overlap with three of the seismic sections from Bruvoll et al. (2009)(B09-25, 23 & 21, respectively). Below follow the results of the morphological analysis of the study area.

6.1.1 Axial Valley

The Mohn's Ridge axial valley (Figure 6.1 and 6.2) trends ~060NE until a northwest bend where its transition into the Knipovich Ridge is marked by the presence of an AVR and trend change. Based on elevation contour lines, the rough axial valley has been enclosed by the -2800 m contour line, as it was found that this is the depth that overall best represents the transition from valley floor to the bounding valley walls. The valley width is relatively even, typically ranging ~7 – 11 km, except for the area around AVR2 and AVR4, where the width increases to ~17 km and 15 km, respectively. The valley floor is consistently deeper than -3000 m, the deepest point being just northeast of AVR4 at around -3500 m. The overall depth varies along the ridge axis as a function of the presence of volcanic ridges, where ridge peaks represent extreme local topographic highs, relative to the surrounding valley floor. (Figure 6.2). Toward the western and eastern flanks, the rift valley is bound by large normal faults that make up the

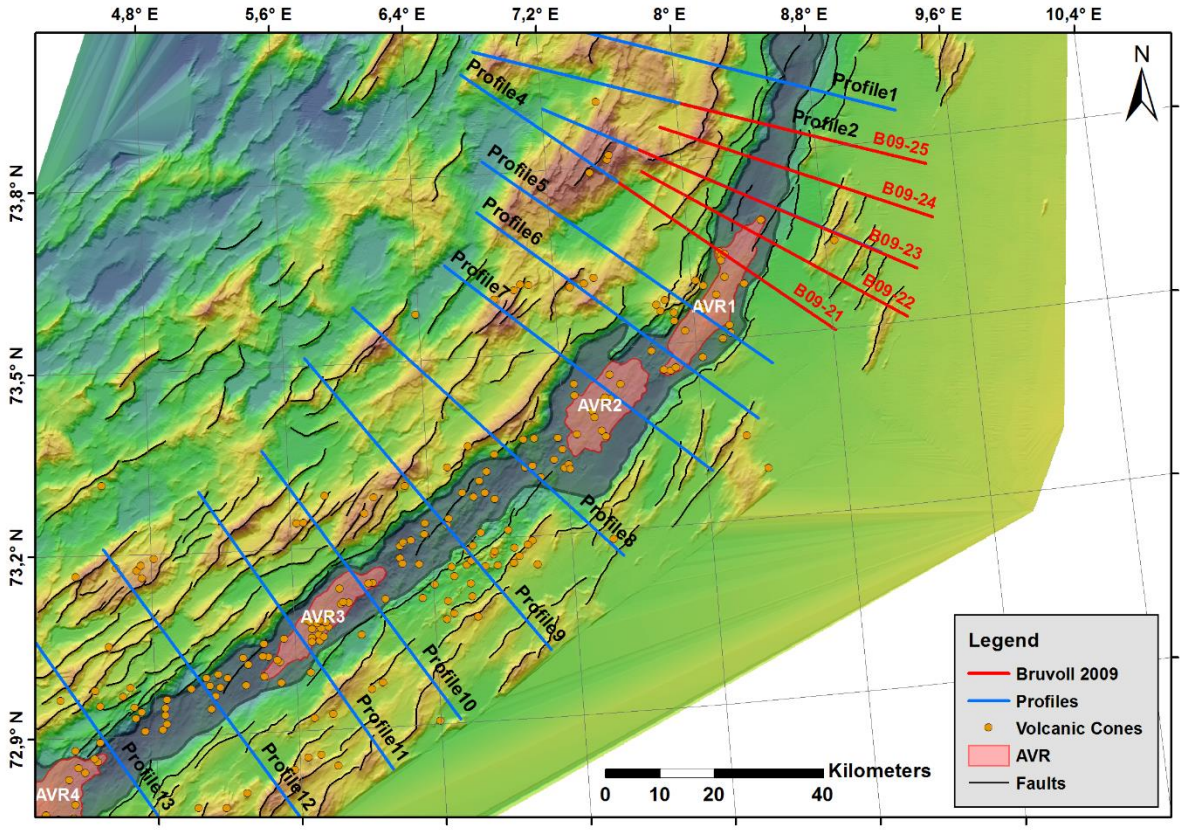

Figure 6.1: *Overview of the axial valley of the study area (shaded area) and features within. Locations of seismic profiles and elevation profiles are marked red and blue, respectively.*

valley walls and mark the transition from valley floor to ridge flank with varying slopes angles, typically ranging from 25 – 40° and 15 – 30°, on the western and eastern sides respectively.

Four prominent AVRs have been identified along the MR axis, termed AVR1 to AVR4 from north to south (Figure 6.1). Contour lines were used to delimit their extent roughly where densely-spaced contours changed to wider-spaced contours, as this approximately represents the area where they transition into the valley floor. The AVRs are elongate features, about 20 – 30 km long and 5 – 10 km wide, arranged in a sinistral en-échelon pattern which is oriented approximately 20 – 30° northward relative to the trend of the axial valley (Figure 6.3). Their properties are displayed in Table 1. On average, they are spaced 30 – 40 km apart, measured from their outer edges, except for AVR1 and AVR2 where the volcanic ridges are very closely spaced, only about 2 – 3 km apart. Larger lineations, visible both on the AVRs and the deeper valley floor, display the same orientations as the ridges before curving into a more parallel orientation when meeting the valley walls. However, identification of features in the central valley is heavily limited by the DTM resolution. The surface morphologies of the AVRs and their immediate surrounding show a clear influence of magmatic activity, resulting in typical volcanic surface expressions with rugged, hummocky and knobby terrain and widespread build-up of volcanic cones.

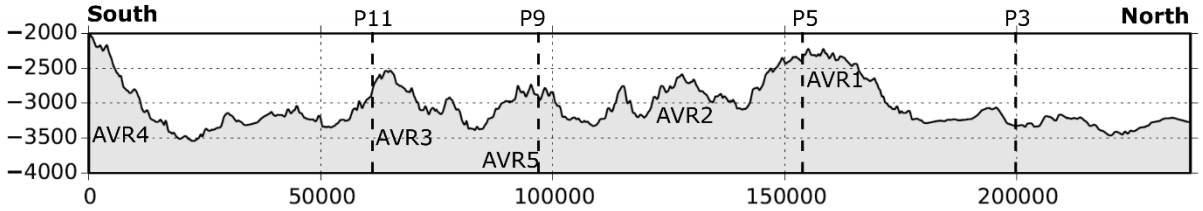

Figure 6.2: *Elevation profile of the axial valley from south (left) to north (right). AVRs represent topographic highs. North of AVR1 the axial valley topography becomes more even as AVRs are no longer present.*

A fifth AVR was identified between AVR 2 and 3(Figure 6.4d), however, it appears to not have been an area of focused magmatic activity in recent time, but rather represents an extinct, fossil AVR, which must have ceased to be volcanically active a considerable time ago given its morphology. The AVR is cut by significant faults on its western side and appears to have subsequently drifted to the ridge flanks, which is evident by the observation that the center of the AVR is subsided relative to its flank-ward segments. Distinct volcanic terrain, with a hummocky texture and volcanic cones, is apparent both on the western and eastern side of the ridge axis where the remnants of the AVR are located.

The sizes, shapes and structures of these cones vary throughout the valley floor; some display planar slopes, while others have convex or concave slopes (Figure 6.4). Some are flat-topped plateaus while others display craters or curved peaks. Sizes vary from a few hundred meters in diameter to a few kilometers, with heights up to more than 100 meters. Unsurprisingly, the occurrence of such volcanic cones is largely confined to areas within the axial valley, with the highest concentration in areas where AVRs are present. Valley floor between the AVRs and toward the valley walls displays a smoother and more regular surface, with less apparent volcanic cones and lava flows. This is for instance very apparent toward the western and eastern valley walls outside of AVR2, where the valley floor shows a much smoother surface with less signs of volcanic influence just outside of the immediate AVR structure (Figure 6.4b).

To the north of AVR1, the valley morphology changes: Throughout the approximately

Name	~Depth (m)	Orientation (°)	~Length (km)	~Width (km)
AVR1	-2100	031	35	5
AVR2	-2400	035	22	8.5
AVR3	-2500	041	29	5.5
AVR4	-1800	039	19*	10
AVR5	-2800	041	18	-

Table 1: *Properties of identified AVRs in the axial valley. Depth and width are measured roughly at the apex and center of the ridges, respectively. * Length of AVR4 is not its total length, as the rest continues outside of the study area.*

80 km that the Knipovich axial valley is visible on the bathymetry, there are no AVRs or other prominent volcanic features whilst they are spaced at around 30 – 40 km within the Mohn axial valley. Instead, the valley morphology is here replaced by smooth seafloor and curved faults (Figure 6.4e). The valley becomes narrower and is bound by a major fault (F3) on its western flank, distinctly visible on seismic profile B09-25 (Figure 6.18). The valley-bounding faults also appear to act differently compared to the MR section: While the MR valley faults and lineations have a slight offset trend within the valley but ultimately curve into a parallel orientation when nearing the valley walls, the valley-bounding faults in the Knipovich valley curve from a semi-axis-parallel orientation trending northward, to an orientation that is much more parallel to the MR axial valley trend than the Knipovich axial trend.

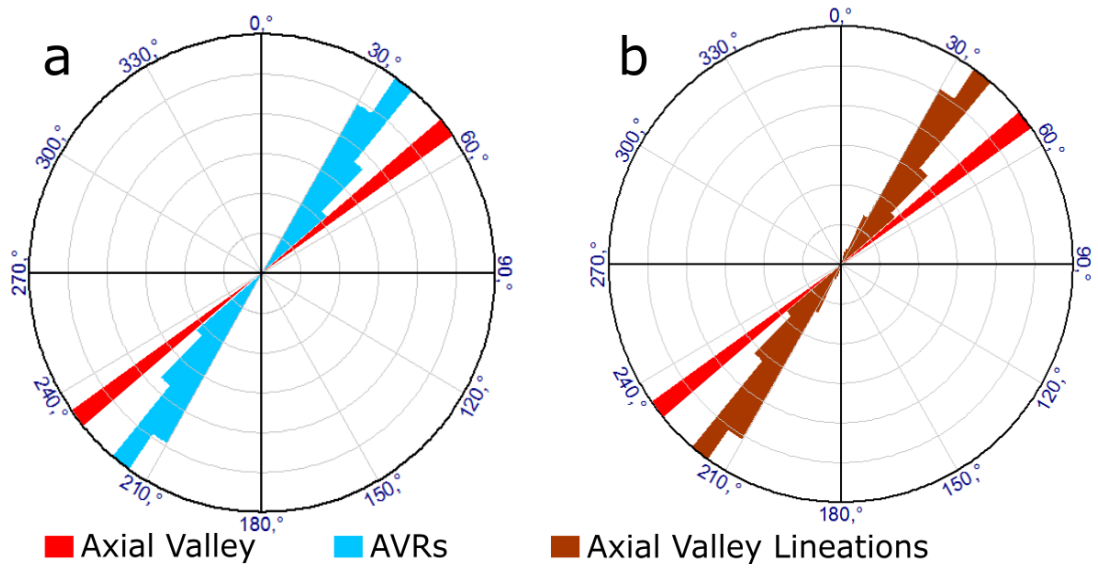

Figure 6.3: *Rose diagrams of the orientations of axial valley features. (**a**) Axial valley trend and AVR trend, showing that the AVRs have a slight northwest offset by ~20-30°. (**b**) Axial valley trend and valley floor lineations. As expected, the lineations have the same 20-30° offset relative to the axial valley trend.*

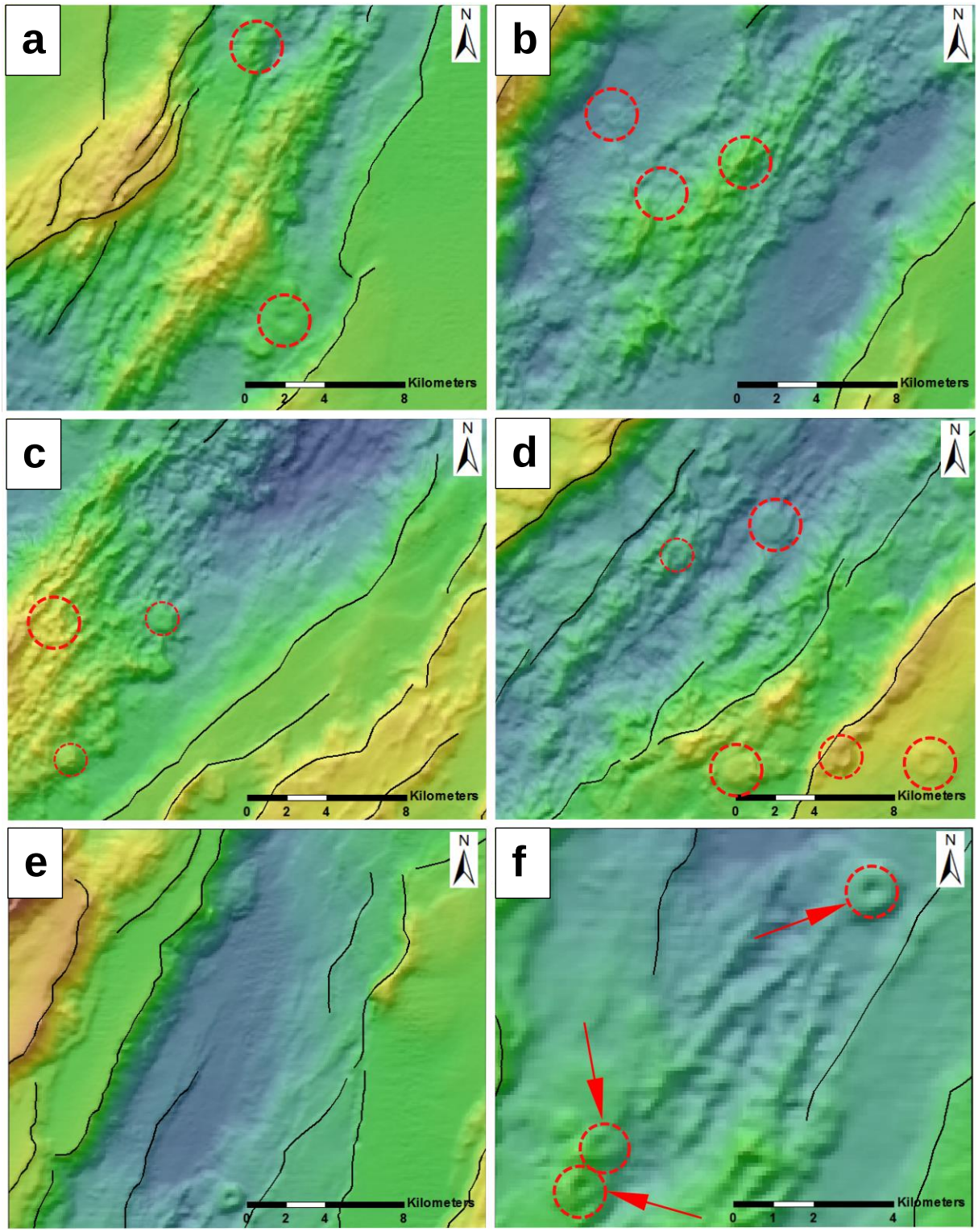

Figure 6.4: *Close-up images of features within of the axial valley. Red circles mark prominent volcanic cones.* ***(a)*** *AVR1 in the Mohn – Knipovich bend,* ***(b)*** *AVR2 located just south of AVR1. This areas shows how the valley floor changes outside of the volcanically affected AVR zones,* ***(c)*** *AVR4, located in the most southern part of the axial valley,* ***(d)*** *the extinct AVR5 located between AVR2 and AVR3, displaying severe faulting, subsidence and uplift of valley floor to the ridge flanks,* ***(e)*** *the rift valley in the transition to the Knipovich axial valley just north of AVR1, showing a smooth surface and very little sign of volcanic influence,* ***(f)*** *close-up of the volcanic cones found around the axial valley of the Mohn's Ridge.*

6.1.2 Western Flank

The western ridge flank is characterized by a rugged surface expression and high topographic relief, with numerous normal faults of varying shapes and sizes, axial volcanic remnants and dome-shaped highs. The morphology changes from north to south, transitioning from more dome-shaped features and outward-facing slopes to steeper inward-facing fault scarps arranged in a parallel fashion, often associated with volcanic structures. Three types of primary geological features have been identified on the western flank: (1) Outward-facing slopes and associated detachment surfaces and core complexes, (2) Major and minor normal faults displaying varying grades of rotation, (3) Abyssal hills, delimited by inward-facing faults scarps and volcanic surface morphologies.

6.1.2.1 Core complexes & Detachment Faulting

Based on the morphological characteristics and criteria outlined in chapter 5.2.3, seven structures have been identified and are proposed to represent core complexes where lower crustal and upper mantle rocks may have been exhumed. They are associated with in total ten linear ridges displaying outward-facing slopes, identified as their corresponding breakaway ridges. Detailed properties can be found in Table 2. The core complexes are exclusively located on the western flank, in the northern part of the MR and the transition into the KR section, within ~60 km of the ridge axis (Figure 6.5). The surfaces of two of these structures (CC1& CC2) have been sampled (Pedersen et al., 2007) and contained gabbros and serpentinites, confirming their lower crustal and upper mantle origin. As such, they proved an excellent morphological reference for the identification of the remaining core complexes.

The first core complex (CC1) (Figure 6.6a) is situated about 20 km west of ARV1 and hosts one of two areas that have been subject to sampling, revealing gabbros and serpentinites. The core complex consists of a central, shallow (13°), inward-dipping detachment surface extending roughly 15 km parallel to the axis before being replaced by branching normal faults on both the northern and southern sides. Toward its off-axis side, the core complex is first delimited by a ~25 km long linear ridge trending 036N with an average outward-facing slope angle of 10°, followed by a parallel and elongate basin measuring approximately 6 x 20 km. The along-axis length of the central core complex surface measures about 20 km, yielding a modest area of ~69 km^2, when compared to some of the other core complexes. From the breakaway ridge to its termination, the central surface is about 4.5 – 5 km long and displays

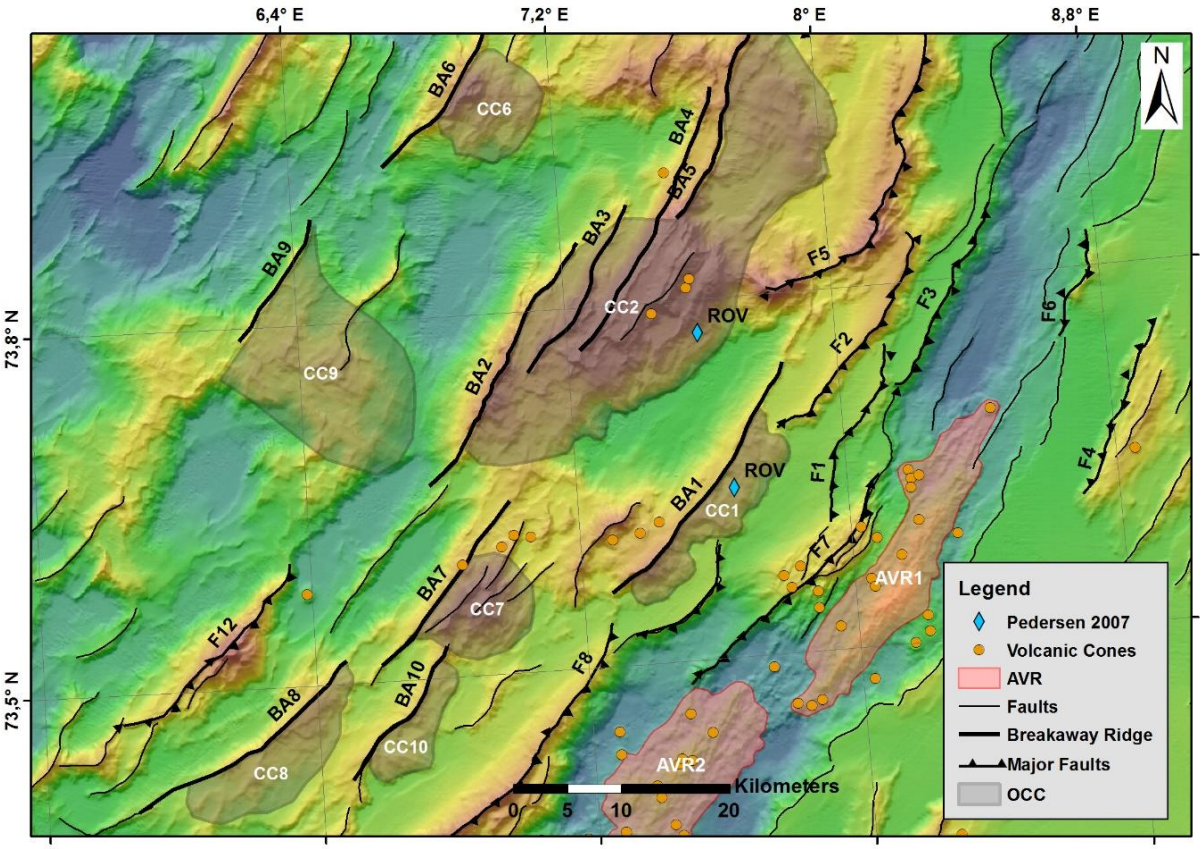

Figure 6.5: *Overview map of identified core complexes. They are marked by a linear breakaway ridge on their off-axis flank and by shallow inward-dipping surfaces. Orange dots mark prominent volcanic cones on the ridge. Blue diamonds mark the areas where drilling has recovered gabbros and serpentinites (Bruvoll et al., 2009).*

weak axis-perpendicular corrugations. No volcanic or other indicators of magmatic activity were identified on this surface.

CC2 (Figure 6.6b), the by far largest of the identified core complexes with a breakaway length of ~ 50 km and an area of approximately 497 km^2, is located just beyond CC1, around 30 km from the ridge axis. Rising more than 1000 m above the surrounding seafloor, the central area peaks at approximately -600 m depth. It has an overall low average inward-facing slope angle of 13° and a rugged surface with a few valley-parallel ridges and lineations at its peak. Weak lineations oriented perpendicular to the valley are present on the lower easternmost sloping side and are interpreted as corrugations. On the outward side of the core complex is a basin running parallel to the ridge axis and the core complex, just as is the case at CC1. The most striking feature of CC2 is that it apparently contains four breakaways, rather than one, as is typically common. The four ridges, termed BA2 – 5 are oriented parallel to each other trending 026 – 035N, are 18 – 28 km long with a spacing of about 2.5 km, and outward-facing slopes ranging from 18 – 28°. From the outermost (BA2) to the innermost ridge (BA5) the breakaways are progressively offset by a few kilometers along their trending direction, leaving

a considerable overlap between them. Toward the axial valley, the southern part of CC2 is terminated by presence of a basin, likely related to formation of CC1. The northern part is terminated by a flat area that could be undergoing rotation related to the large F5 fault further east toward the ridge axis. The surface of CC2 also varies between the southern and northern ends. The southern part around BA4 is very irregular, with large relief variations along its surface and an axis-parallel ridge forming its highest point, interpreted as a rafted block (Figure 6.12). In this area, small semi-circular shapes are present and could be indicators of earlier volcanic activity, before the block was rafted. The most southern parts of CC2 to the east of BA2 display a smoother surface, similar the northern area to the east of BA5, which looks more similar to the "textbook" core complex, displaying a shallow, inward-dipping slope, axis-perpendicular corrugations and relatively rugged, but overall smooth surface. The general morphologies of CC2 in the areas east of BA1 and BA5 are similar to the core complex surface of CC1.

Unfortunately, no sampling has been conducted on any of the other surfaces which could help confirm that they indeed represent core complexes. Thus, the remaining five identified structures are proposed to be core complexes based on observed characteristics in published literature and the morphology of CC1 & CC2. They all share a few common characteristics: (1) they display a breakaway ridge on their outward-facing sides with slopes ranging from $9-18°$, (2) the breakaway ridges typically extend further parallel to the ridge axis than the core complex surfaces are wide, (3) basinal depression features are typically present in the immediate area behind or obliquely to the side of the core complex, and (4) the core complex surfaces are large and dip weakly, between $9-17°$, toward the ridge axis.

There are, however, some differences related to their geometry and surface morphology (Figure 6.7). For instance, CC6 and CC7 are relatively similar, both in size and geometry. Both core complexes are of moderate size (both are ~ 69 km^2), have breakaway ridges that are far longer than the surfaces are wide, and do not have any visible corrugations, but rather axis-parallel lineations, likely representing rafted fault blocks. On the south side of CC7, another breakaway (BA10) and core complex (CC10) are present. The corresponding breakaway (BA10) appears to branch out of CC7, possibly from one of the rafted blocks. Just a few kilometers further west is CC8, a core complex whose surface expression is similar to CC10. Their associated breakaways are outward-facing with dips of 18° and 11°, while the inward-facing surfaces have shallow slope values of 8° and 10°, respectively. While CC8 is more than twice the size, the surfaces are similarly smooth and show no sign of rafted blocks. Weak corrugations are visible on both surfaces. With a length of more than 7 km (Table 2), both

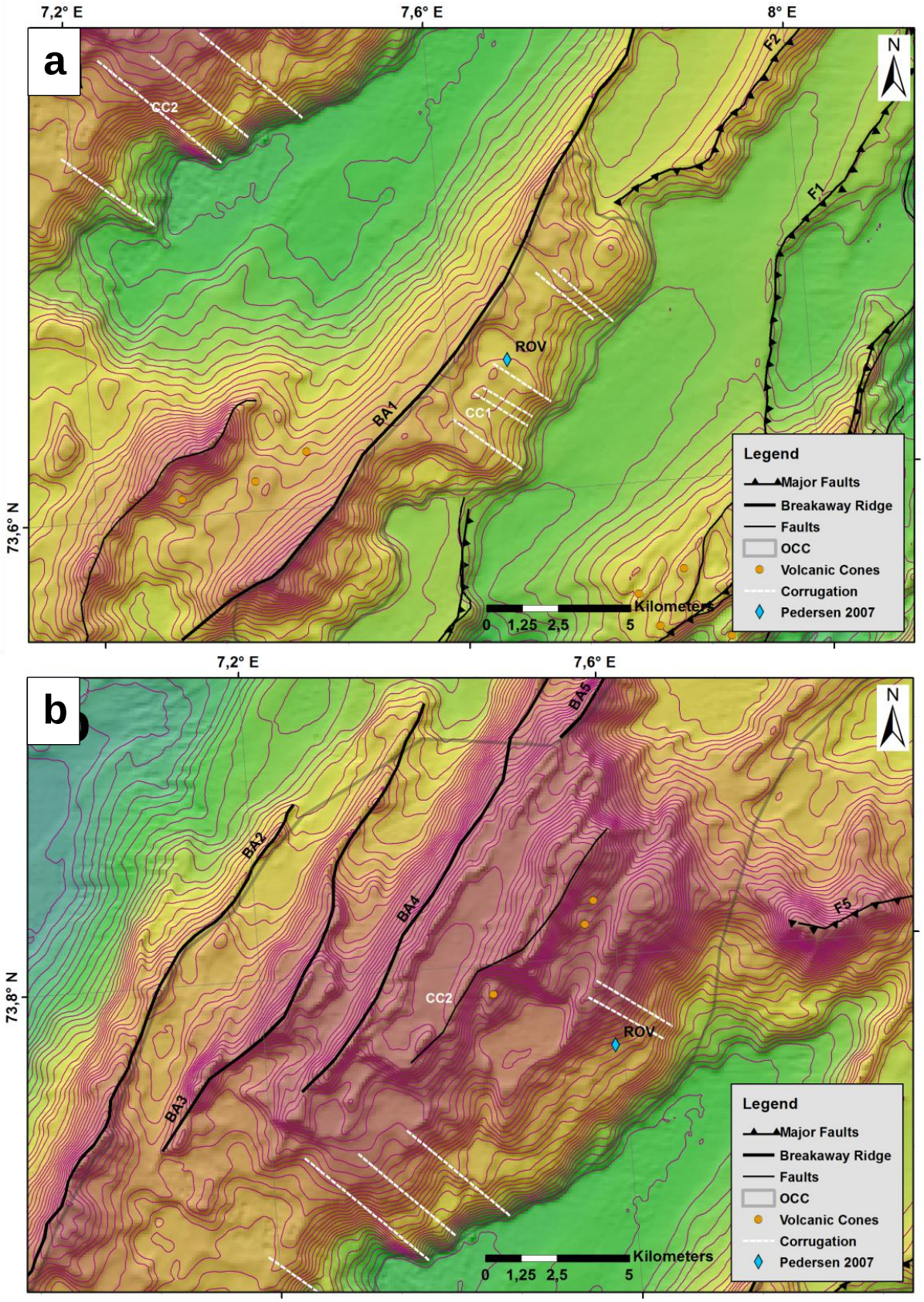

Figure 6.6: *Close-up view of CC1 and CC2. Both show weak axis-perpendicular lineations identified as corrugations and ridge-parallel breakaway ridges. CC2 is capped by blocks displaying signs of volcanic activity, such as circular structures that could be remnants of volcanoes. Contours are at 100 m intervals.*

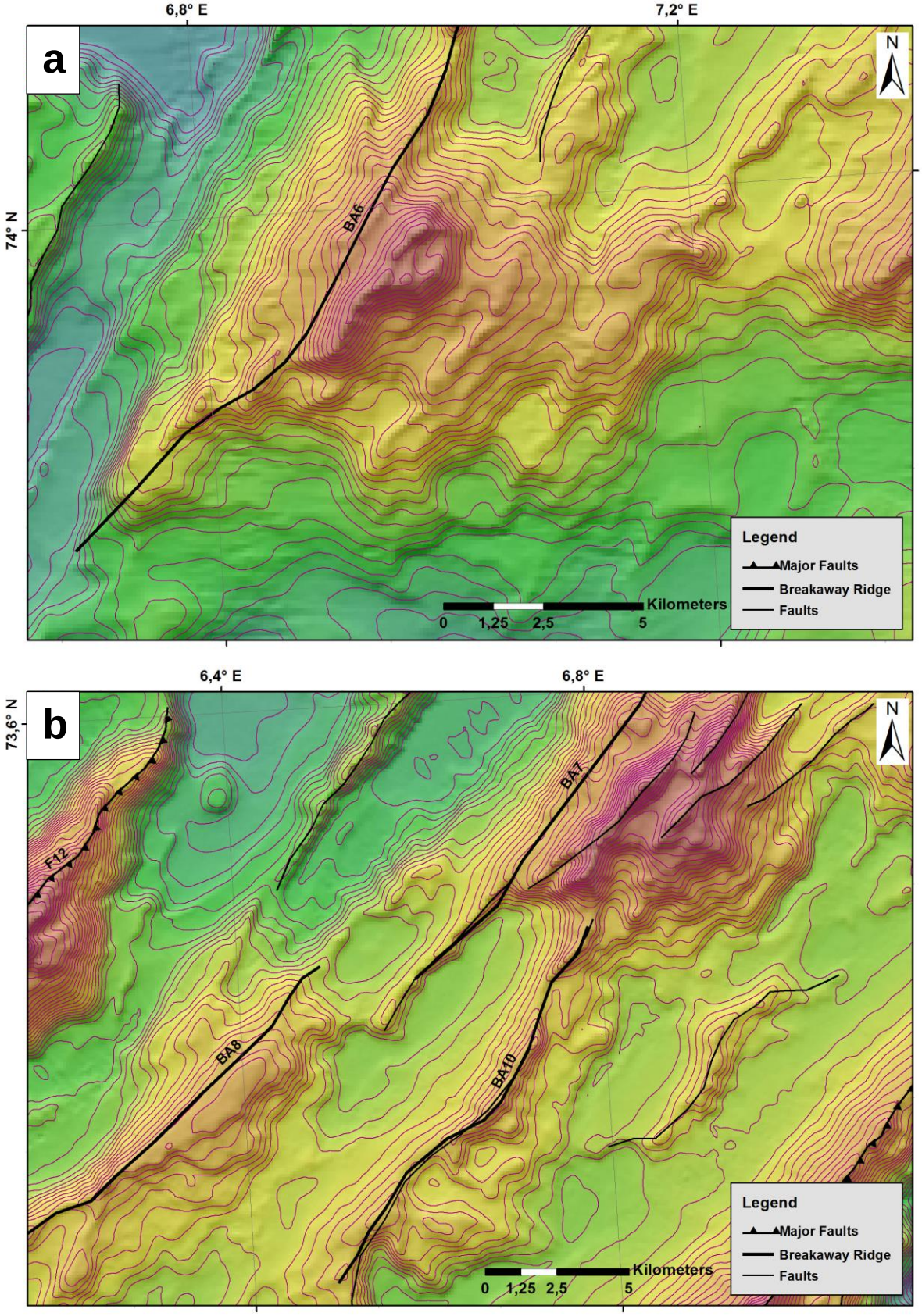

Figure 6.7: *Close-up of CC6* ***(a)*** *and CC7, CC8 and CC10* ***(b)****. They show the characteristic outward-facing slope of the breakaway ridge, followed by a shallower inward-sipping dome-shaped surface. CC6 and CC7 show rafted blocks and volcanic structures on their surfaces, whereas CC8 and CC10 are smoother.*

Break-away	BA Outward Slope (°)	~BA Length (km)	BA Azimuth (°)	Core Complex	OCC Inward Slope (°)	Area (km^2)	~Surface Length (km)	Corru-gations?
BA1	10	27	036N	**CC1**	13	69	4.5	Yes
BA2	18	19	030N	**CC2**	13	497	9|	Yes / No
BA3	23	28	026N	**-**	-	-	9	-
BA4	28	27	031N	**-**	-	-	10	-
BA5	24	18	035N		-	-	10	-
BA6	17	38	016N	**CC6**	13	66	7.8	No
BA7	17	20	038N	**CC7**	17	69	8.3	No
BA8	18	24	054N	**CC8**	8	82	5	Yes
BA9	15	13	030N	**CC9**	9	212	20	Yes
BA10	11	16	035N	**CC10**	10	39	5	Yes

Table 2: *Properties of breakaways and their associated core complexes. Surface length is measured perpendicular from the breakaways to the termination of the surface toward the ridge axis.*

Basins have formed on the outer sides of the breakaway ridges of CC7, CC8 and CC10, oriented parallel to them and the axial valley. CC9 has a rather different surface morphology, with weakly visible corrugations and a rather short breakaway ridge dipping outward at 15°. Determining the actual size of the core complex surface is a challenge here, as there are no clear features that could be used to delimit the extent. The topographic plateau in this area, which CC9 fuses with into one great high, displays a deformed and unstructured texture and it is unclear where exactly the core complex begins, as the breakaway also is not a clear delimiter for a southern boundary. With its current extents, the surface area is 212 km^2, making it the second-largest core complex in the area.

6.1.2.2 Normal Faulting and Abyssal Hills

The western flank is additionally characterized by both major and minor normal faulting, often showing significant rotation of the fault scarps resulting in outward-facing slopes, especially in the northern section where also the core complexes and associated detachment faults are situated. These major normal faults are around 20 – 30 km long and are typically situated within 15 km of the axial valley center, except for F9 – F11 where the distance is up to 20km. These latter three faults are, however, situated in the area belonging to the Knipovich Ridge. Detailed properties can be found in Table 3.

The assumed initially sub-horizontal seafloor at the major faults has been rotated outward to slopes ranging from 9 – 15° over the course of their evolution. Fault scarps are typically larger than 500 m, with some scarps even as large as 1500 m (F8). F7 and F8 are forming as part of the western valley walls with rugged and irregular inward-facing slopes

(Figure 6.8), showing indicators of subsequent internal minor faulting and large-scale mass wasting (F8). The northern section of F8 also hosts the mass wasting plateau where Mohn's Treasure is located. Signs of earlier volcanic activity at these two faults are present in the form of knobby and hummocky terrain on the outside slope of F8 and the general morphological similarity between the surface of F7 and AVR1. Deformed circular and semi-circular shapes are also weakly visible at both F7 and F8, however, thorough identification is limited by the DTM resolution. Major normal faults where rotation occurs are identified in and confined to the same area as the core complexes and their associated detachment faults, and are not found further south of F8. CC1 is terminated on its northern side by F2, a rotated fault branching out of the core complex, suggesting potentially further relationship between the two features. Overall, the rotated major faults are characterized by a change in trend from 030 – 040N at F7 and F8 to 011 – 016N at F9, F10 and F11 further north, (Figure 6.11) likely related to the transition from the MR to the KR and the accompanying change of the axial valley trend.

Further south of F8 and CC8 on the western flank, the normal faults change to become overall smaller and show signs of volcanic activity on their outward-facing slopes. Fault scarp heights are commonly between 300 and 500 m, but may be as large as up to 800 – 900, and are typically steeper than their outward-facing conjugates (Figure 6.9). These ridges are volcanic abyssal hills originally located within the valley before being cut by normal faults and subsequently transported to the flanks.

Two large edifices stand out in this southern section (Figure 6.10). They display similar surface and slope morphology as the valley floor AVRs. Frequent internal fracturing, faulting and remnants of volcanic activity on their surfaces is common. In contrast to the abyssal hill-forming normal faults in the area, these structures do not show signs of an inward-facing major break-up fault that that could act as a mechanism for the transport to the flank, but rather appear to be structurally relatively intact.

Name	Fault Trace (km)	Azimuth (°)	Outward Slope (°)	Distance from Valley (km)
F2	24	033	9	11
F5	34	030	14	12
F7	27	042	8	6.5
F8	35	040	14	12
F9	27	016	8	30
F10	17	012	15	23
F11	33	011	10	19
CHF	15	050	18	6

Table 3: *Properties of major rotated normal faults in the study area. CHF refers to the Copper Hill Fault, see chapter 6.4.*

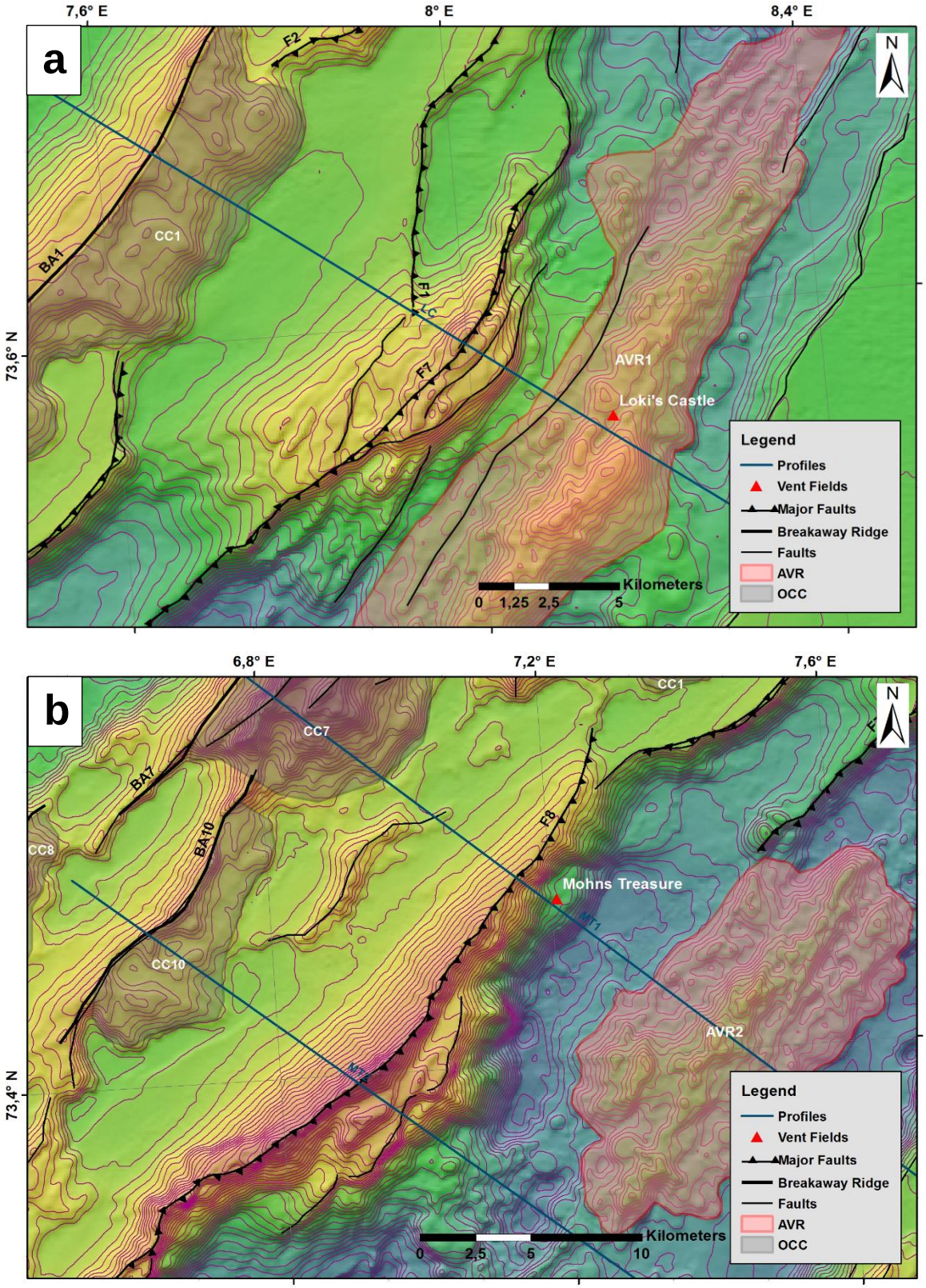

Figure 6.8: *Close-up of major faults F7* ***(a)*** *and F8* ***(b)***. *Both faults show outward-rotation and possible formation of basins behind them. Internal faulting is visible, especially at F7. Another fault is present just ~2.5 km east of F7, at the western edge of AVR1. F8 shows volcanic influence directly in front of its slope, to the south of AVR2. Blue lines mark profiles used in* chapter 7.2.2. *Contours at 50 m intervals.*

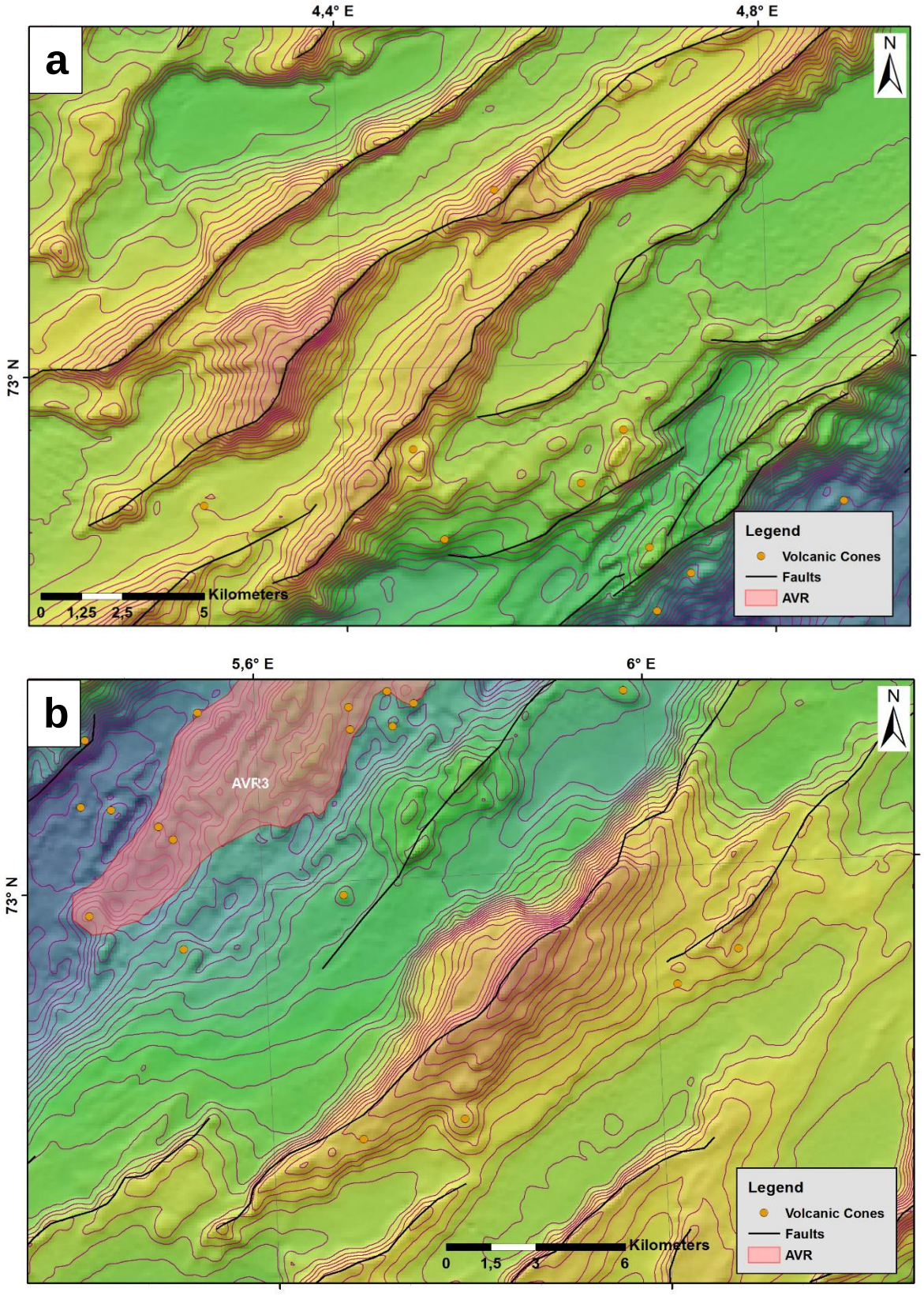

Figure 6.9: *Close-up of typical abyssal hill morphologies.* ***(a)*** *Abyssal hills in the southern part of the western flank. They show steep fault scarps and shallower outward-facing slopes with similar morphology to the AVRs in the axial valley. Scattered circular volcanic features are found on their surfaces and in the surrounding area. An elevation profile of this area is found in* Figure 6.14. ***(b)*** *Large abyssal hill on the eastern flank east of AVR3 shows the same morphological characteristics. Contours are at 50 m intervals.*

6.1.3 Eastern Flank

The eastern flank shows a different surface expression compared to western flank, characterized by parallelly-oriented abyssal hills along its full extent in the study area. These abyssal hills show the same characteristics as their counterparts on the southern western flank, albeit with a more pronounced volcanic morphology on the outward-facing slopes, especially visible in vertical elevation profiles (e.g. Figure 6.14). The fault traces and their accompanying abyssal hills are primarily trending toward 045–060N, with a few shorter faults trending toward a more northward-oriented 030N (Figure 6.11). In the north, the eastern flank consists of flat seafloor, displaying almost no surficial influences of faults except for a few scattered arrays of abyssal hills penetrating the seafloor. One of these areas is to the east of AVR1 where several distinct ridges rise from the seafloor, oriented parallel to each other. These ridges have been imaged by the B09-21 to B09-25 seismic lines (Figure 6.15 to 6.18).

Just as is the case on the southern western flank, the truncating ridges on the eastern flank are typically characterized by steeper inward-facing fault scarps and shallower outward-facing slopes. The geometry of the ridges is similar to the AVR flanks in the axial valley. The seafloor between the array of ridges in the area around the bend is completely flat and indicates significant sedimentation. Further south, the eastern flank attains a surface expression similar to the southern parts of the western flank, although the morphologies of the abyssal hills are more pronounced here. The abyssal hills are up to 30 km long, approximately the same length as the AVRs in the axial valley. Scarp heights are comparable to the heights of abyssal hills on the western side, for the most part ranging from 300–500 m with a few cases up to around 900 m. The outsides-facing slopes display the common knobby and hummocky surfaces associated with volcanic activity. Circular and semi-circular shapes are weakly visible on some of the slopes.

Overall, the study area displays a clear morphological change in flank development from north to south, moving away from a distinctly asymmetrical across-axis topographical expression favoring large-scale faulting and core complex development in the northern part of the western flank, to a more symmetrical expression toward south where both flanks are characterized by similarly sized and spaced faulting and formation of volcanic abyssal hills.

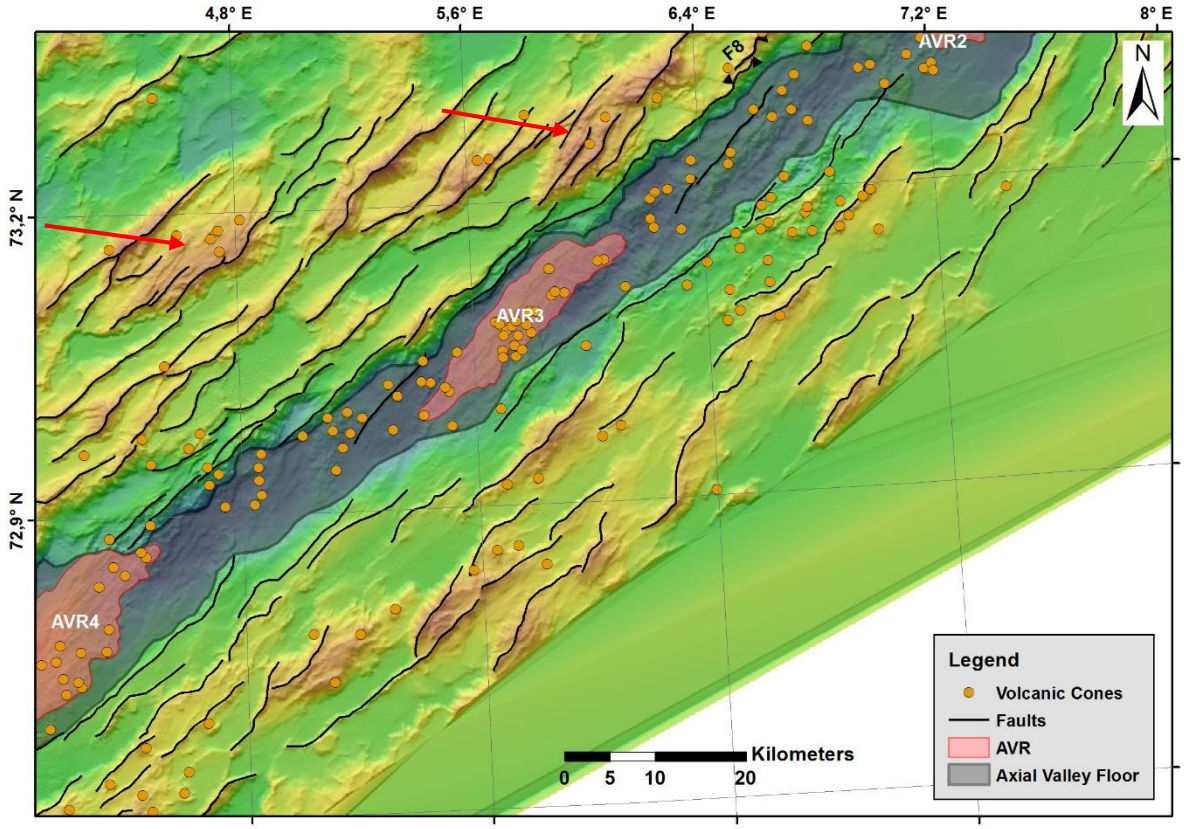

Figure 6.10: *Close-up of the southern part of the study area. On the western flank, the seafloor displays smaller, semi-parallel normal faulting and abyssal hill structures, with outward-facing slopes displaying hummocky and knobby terrain. Particularly on the eastern flank, the abyssal hills display semi-circular volcanic structures. Typically, the faults scarps are much steeper than the outward-facing slopes. Two large edifices (red arrows) of presumably volcanic origin are present on the western flank, likely representing remnants of earlier AVRs.*

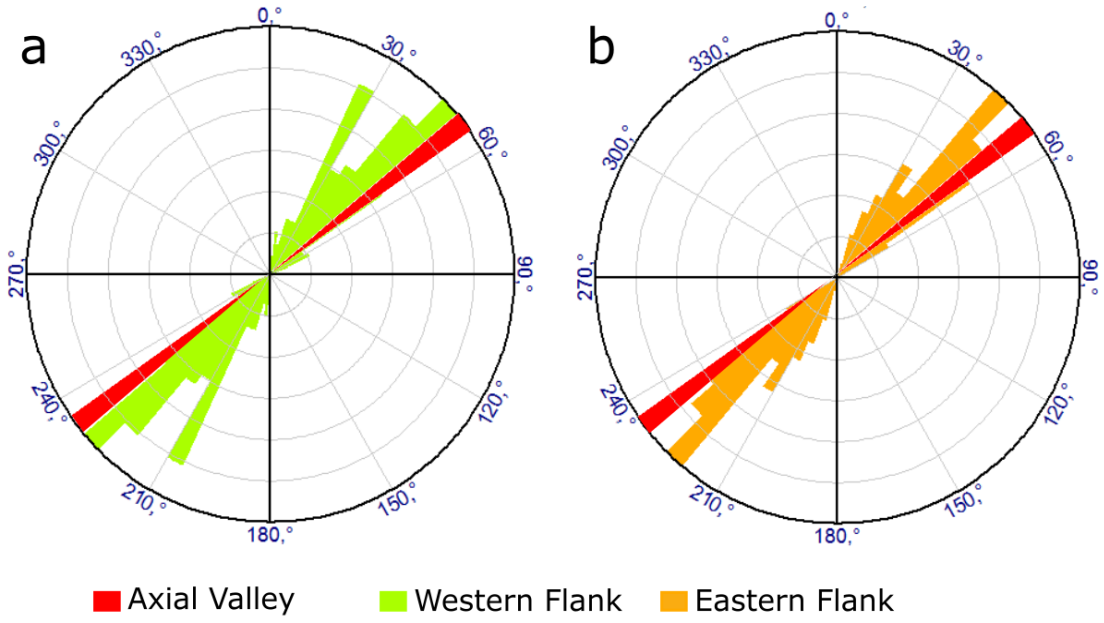

Figure 6.11: *Rose plot of fault traces on the western flank **(a)** and eastern flank **(b)**. Clearly visible on the western flank is a group of faults that have a markedly different strike than the rest, represented by the most northern major faults F9 – F11. The eastern flank display an overall homogenous orientation.*

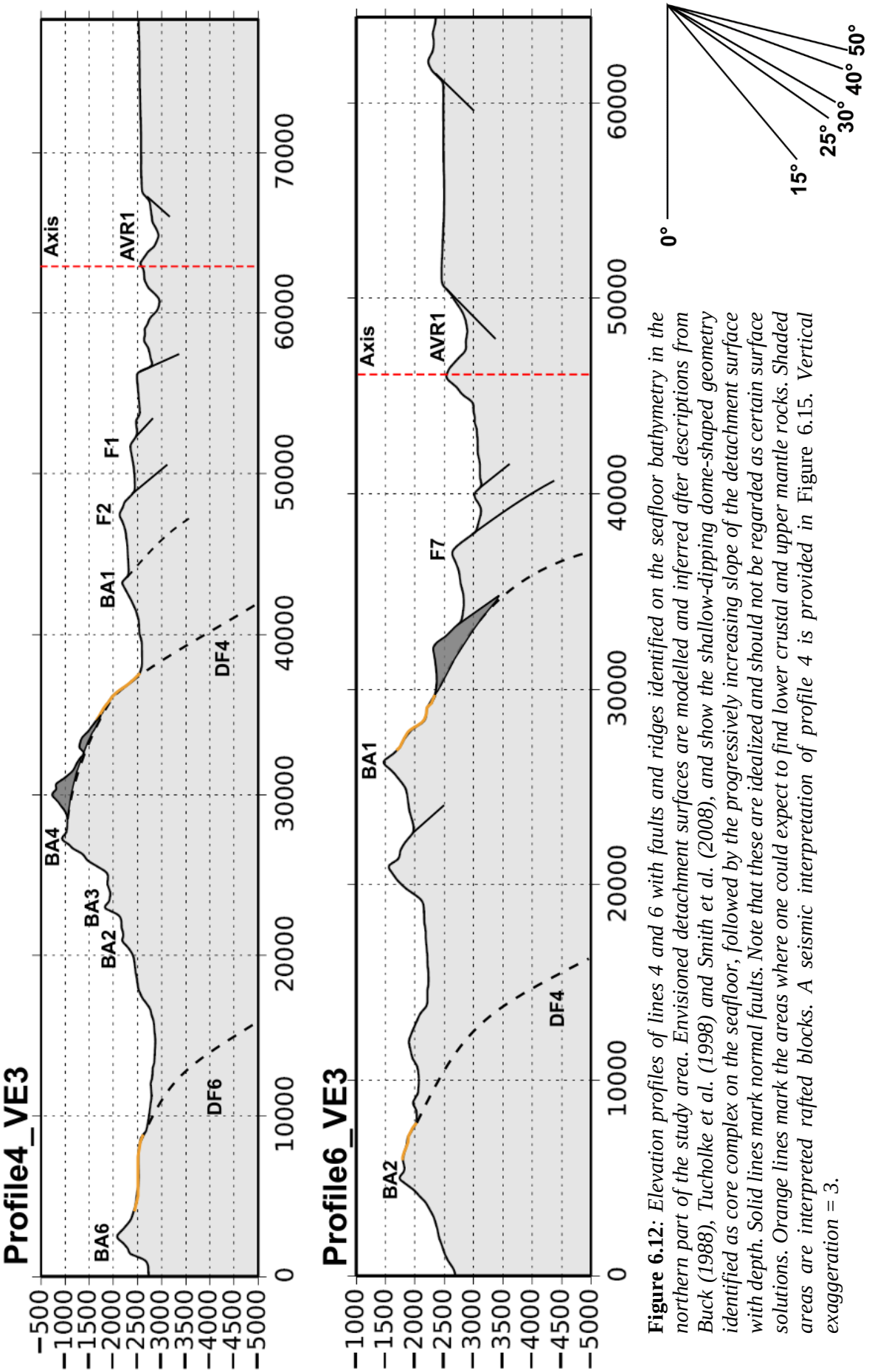

Figure 6.12: *Elevation profiles of lines 4 and 6 with faults and ridges identified on the seafloor bathymetry in the northern part of the study area. Envisioned detachment surfaces are modelled and inferred after descriptions from Buck (1988), Tucholke et al. (1998) and Smith et al. (2008), and show the shallow-dipping dome-shaped geometry identified as core complex on the seafloor, followed by the progressively increasing slope of the detachment surface with depth. Solid lines mark normal faults. Note that these are idealized and should not be regarded as certain surface solutions. Orange lines mark the areas where one could expect to find lower crustal and upper mantle rocks. Shaded areas are interpreted rafted blocks. A seismic interpretation of profile 4 is provided in* Figure 6.15. *Vertical exaggeration = 3.*

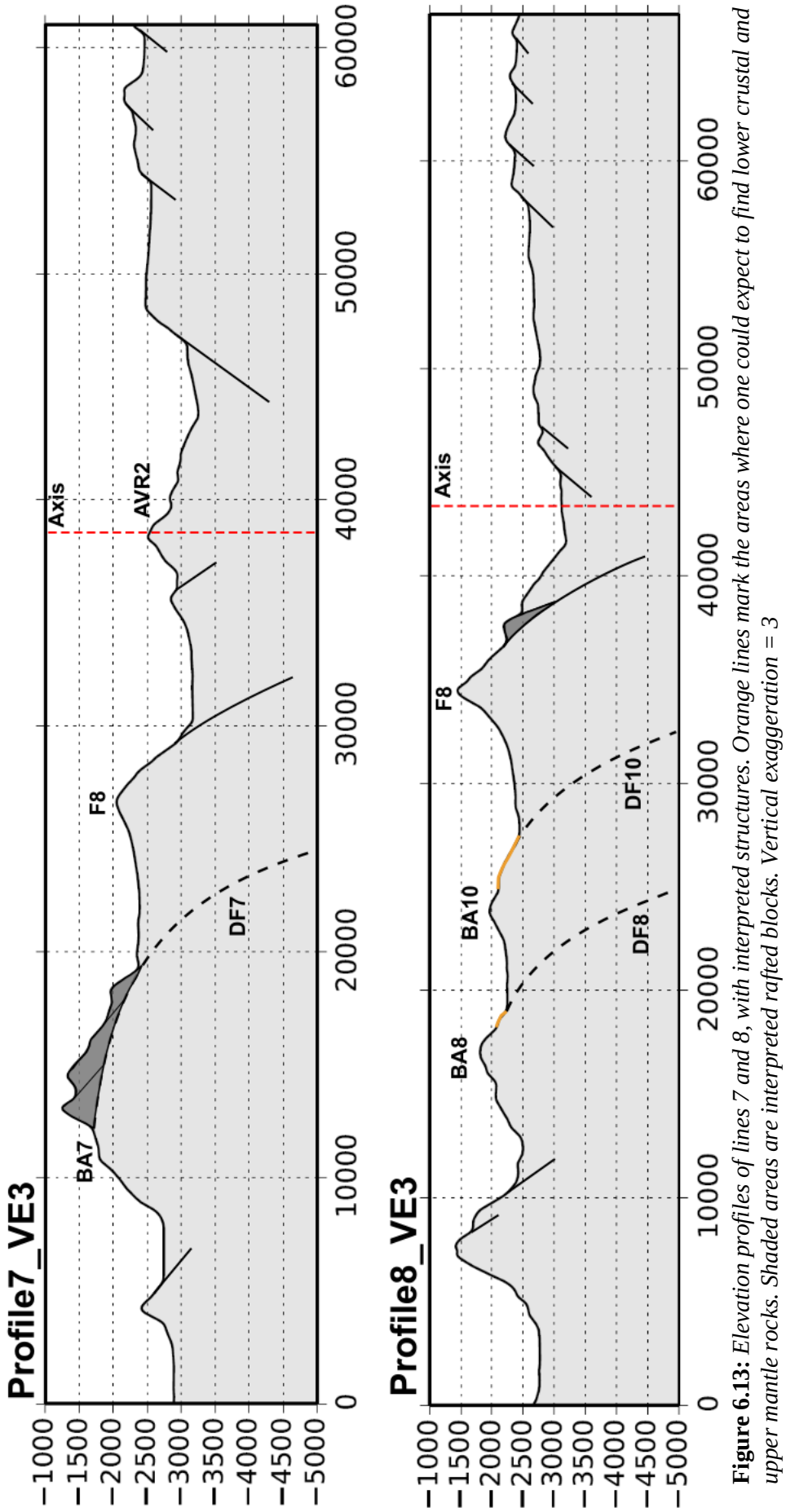

Figure 6.13: *Elevation profiles of lines 7 and 8, with interpreted structures. Orange lines mark the areas where one could expect to find lower crustal and upper mantle rocks. Shaded areas are interpreted rafted blocks. Vertical exaggeration = 3*

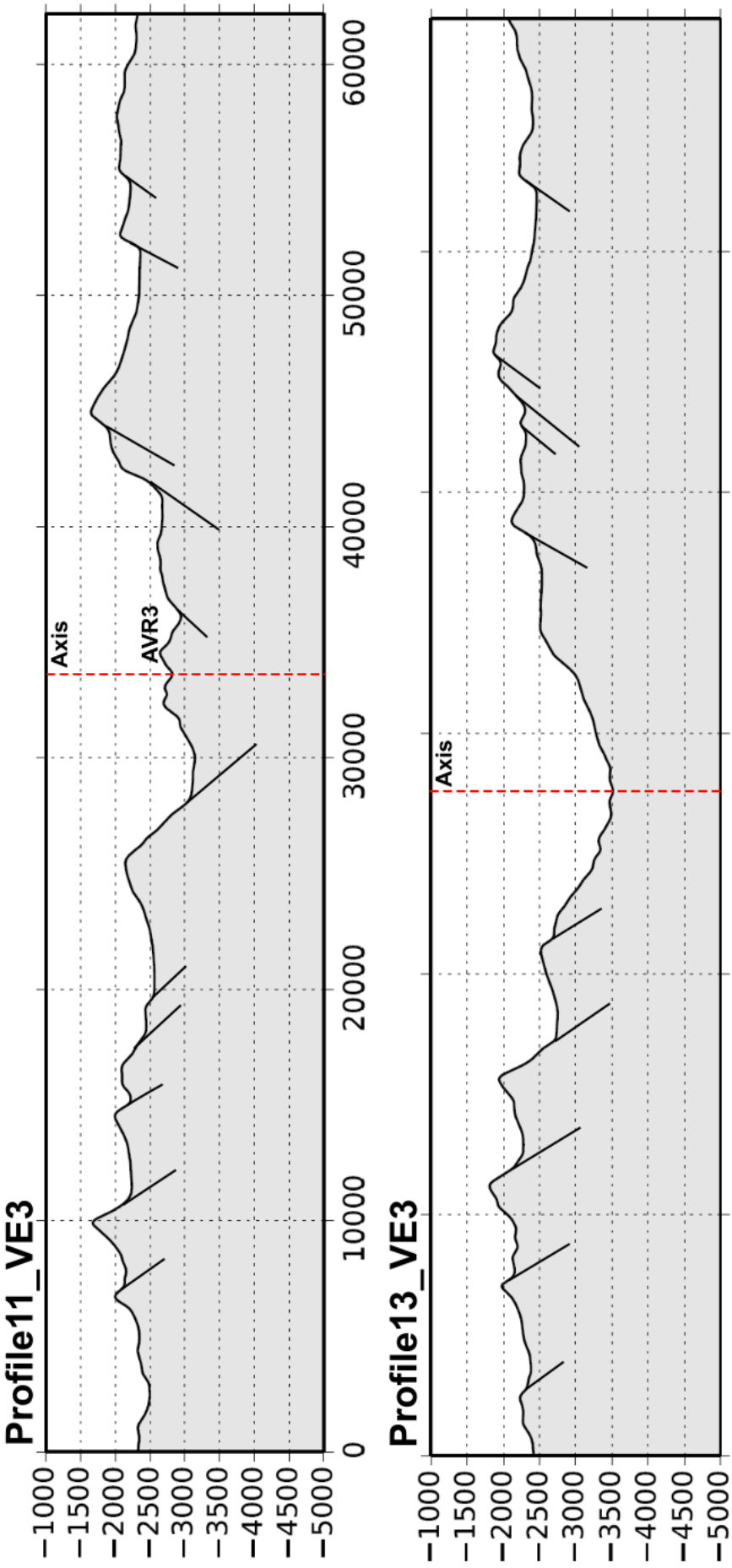

Figure 6.14: *Elevation profiles of lines 11 and 13 in the southern part of the study area. A distinct morphological change of the surface expression is visible when moving from north to south in the study area. Whereas the northern part is dominated by an asymmetrical distribution of large, rotated normal faults, core complexes and their associated detachment faults, the southern area of the ridge exhibits a symmetrical morphology and volcanic abyssal hills on both flanks. The rugged volcanic terrain on the outward-facing slopes and their morphological similarity to the AVRs is pronounced and clearly visible on these cross-sections. Vertical exaggeration = 3, fault lengths are only conceptual and do not necessarily represent their true vertical extent.*

6.2 Seismic Profiles Interpretation

The seismic reflection profiles also show distinct differences in faulting style and history across the flanks. However, where the morphological analysis of the seafloor was limited to surface features, the seismic data gives additional information in the form of sub-surface imaging. For the purpose of this study, two primary seismic horizons are of interest: (1) The seabed reflector and (2) the basement reflector. The seismic data show an overall clear, undisturbed and continuous seabed reflector marked by a positive seismic response caused by the acoustic impedance contrast when transitioning from water to seabed sediments. On the eastern flank, this reflector is flat and undisturbed on profile 21 and 25 (Figure 6.15 and 6.18), while profiles 22 – 24 (Figure 6.15 to 6.17) show how it has been truncated by faults and their fault blocks, or in this case ridges. On the western flank, on the other hand, the faulting severely offsets and disturbs the seabed reflector signature, in many instances resulting in tilted geometries.

The basement is at times challenging to trace as the transition from the sediment package to the basement rock is most often not marked by a clear and distinct reflector. It is instead characterized by chaotic reflections and must be inferred based on vertical offsets marking faults and the chaotic seismic signature, which implies some type of velocity contrast to be present, even though if it appear noisy or distorted. Using these features as guides, a rough basement reflector is traceable on the eastern flank, whereas on the western flank the tracing is hindered by the severe faulting and the subsequent disturbance of the beds. Applying a frequency filter to smooth the image and reduce noise was not very successful, as too much detail is lost during this process.

The sediment package situated between the seabed and basement reflectors displays varying thickness from 100 to 800 m on both flanks, although it is overall thicker on the eastern flank. Larger thicknesses on the western flank are mostly associated with the lowest points of wedge shaped fault blocks. The eastern sediment package is mostly oriented sub-horizontally with only a few sloping sediment layers on the outward-facing slopes of the fault blocks before they are capped by later horizontal layers. The package also appears internally relatively undisturbed, suggesting that there has been no significant tectonic activity during the depositional process. In contrast, the sediments on the western flank show large wedge shapes and highly tilted layers, implying that they are syn-tectonic sediments deposited during fault formation. It is also at these wedges where the largest sediment thicknesses are found on the western flank. Toward the tops of many of the fault blocks, the sediment reflectors gain a less

steep, semi-horizontal orientation, suggesting that rotation has decreased during the sedimentation process.

While the seafloor bathymetry shows the area surrounding the abyssal hills structures to the east of AVR1 as flat and undisturbed, the seismic profiles 21 (Figure 6.15) and 25 show how the abyssal hills continue beneath the post-tectonic sediments. The thickness of the sediment package ranges from about 200 m on top of the abyssal hills to about 800m at the lowest points between hills.

Faulting is frequent on both flanks, but appears to be of contrasting character. For comparative reasons the fault names from Bruvoll et al. (2009) have been carried over to this new interpretation. The eastern faults are smaller and have outward-facing slopes that display a wavy and hummocky morphology, reminiscent of volcanic abyssal hill terrain, while the faults on the western flank display smoother reflectors. A seismic velocity of 1800 m/s (Bruvoll et al., 2009) was used for the sediment package during computation of fault angles. Calculations using different P-wave velocities between 1700 m/s and 2000 m/s only yielded a $2-3°$ difference in the calculated angles.

Fault angles are overall slightly steeper on the eastern flank, with slopes frequently as steep as $35-40°$, even reaching 50° (F4 on Figure 6.16). Faults on the western side display similarly steep angles as well, although not as frequently. Shallower overall fault angles fit the observation of syn-tectonic sedimentation and inferred fault block rotation on the western flank. An interesting observation is that, especially on the western flank, the faults seem to curve slightly in a concave-up fashion, essentially displaying a weak listric geometry at depth. The tracing of faults is unfortunately limited to depths where sediments are present as the seismic data is unable to image faults that continue into the basement. Their total length and geometry further at depth is therefore uncertain and cannot be constrained from the seismic data.

The contrast in faulting style and sediment geometries between the two flanks suggests that the western flank must have undergone major fault formation and rotation during the depositional process while at the same time the eastern flank was affected by only minor faulting and little or no rotation and thus further support and affirm the observed asymmetrical evolution of this northern part of the ridge.

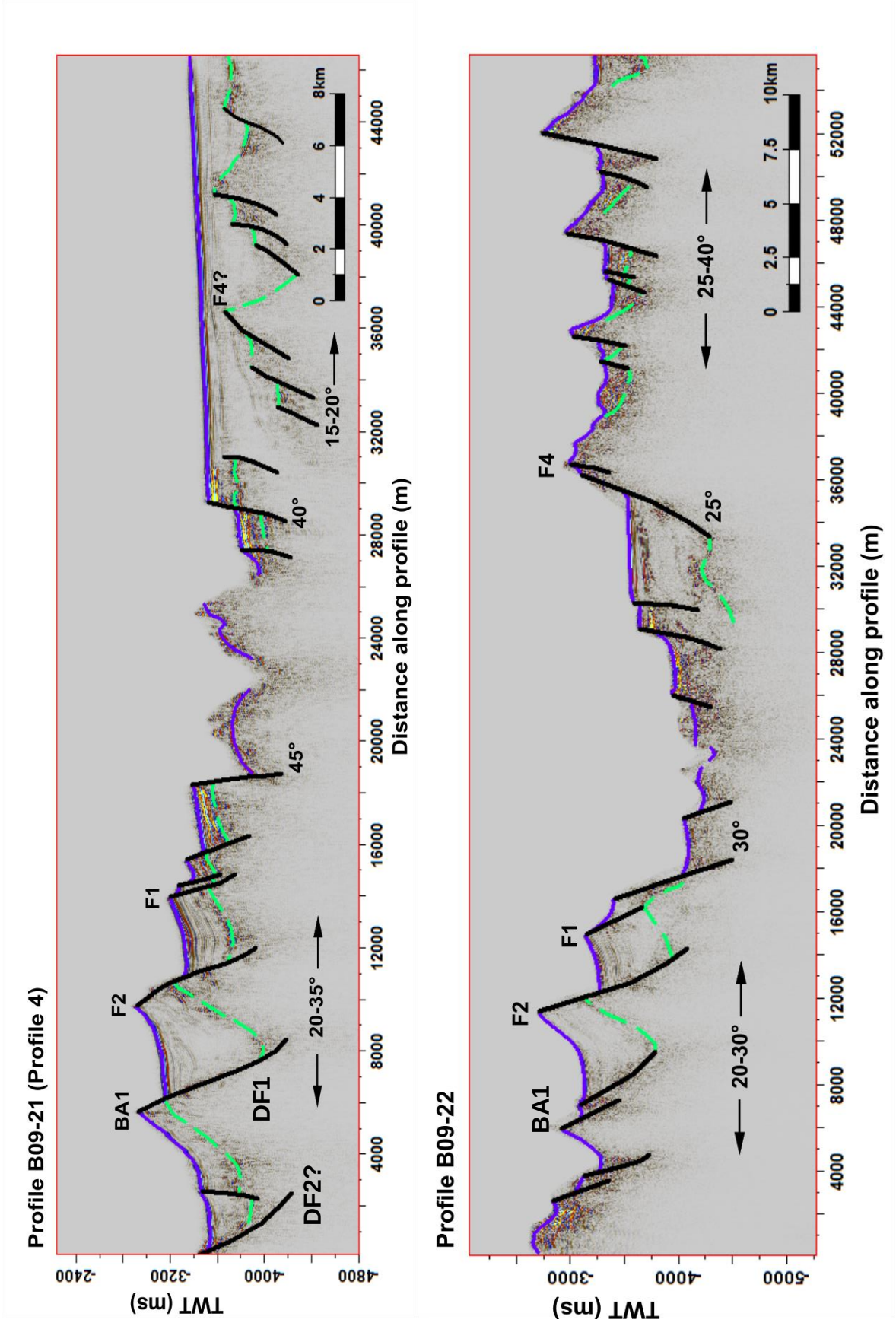
Profile B09-21 (Profile 4)
TWT (ms)
Distance along profile (m)
BA1
F2
F1
DF1
DF2?
F4?
20-35°
15-20°
45°
40°
0 2 4 6 8km
Profile B09-22
TWT (ms)
Distance along profile (m)
BA1
F2
F1
F4
20-30°
25-40°
30°
25°
0 2.5 5 7.5 10km

Figure 6.15: *Interpretation of seismic profile B09-21 and B09-22. The valley bounding faults have similar angles on both flanks, while the fault angles overall are slightly larger on the western flank. DF1, F2 and DF2 to the left of DF1 appear to be curving in a concave-up geometry at depth. The eastern flank is covered by a thick package of sediments. Faults on both flanks show some curvature to their surfaces. Purple line = seabed reflector, green dashed line = rough basement reflector, black lines = interpreted faults, TWT = two-way travel time*

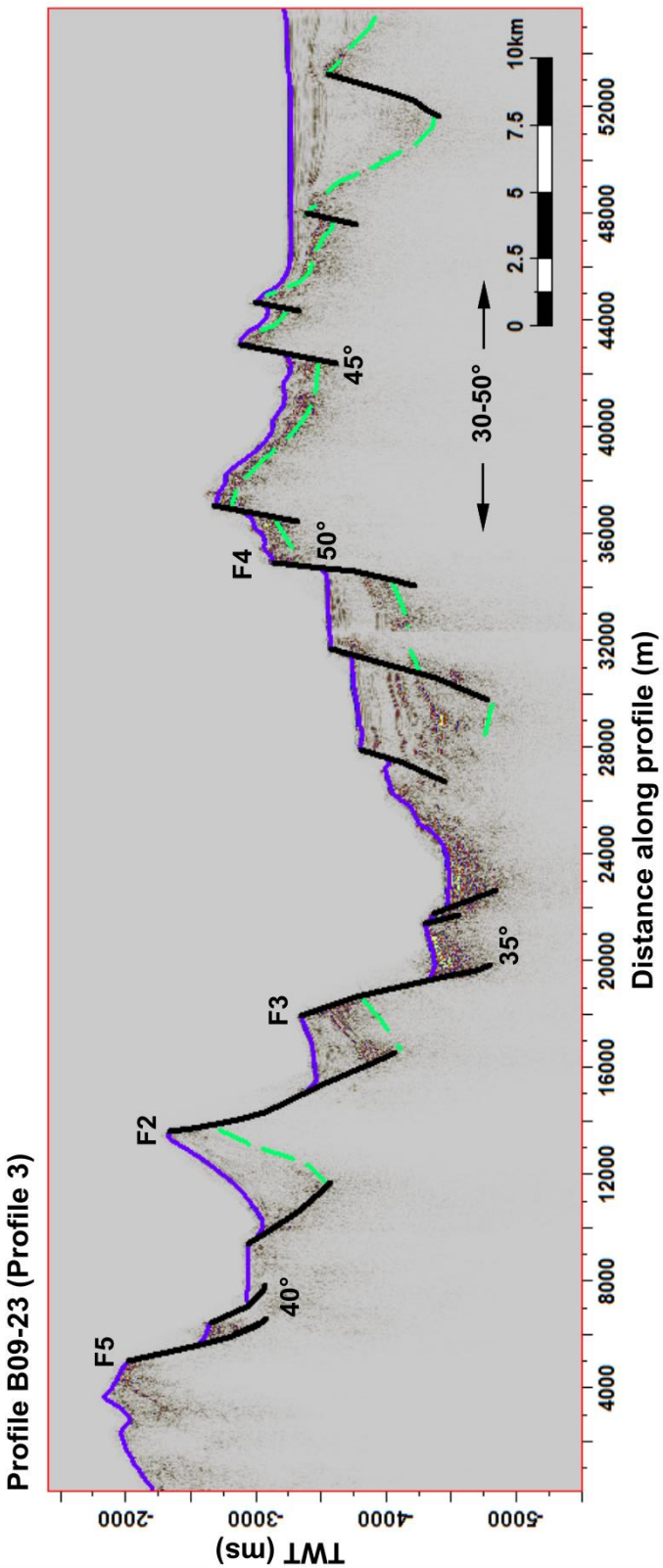

Figure 6.16: *Interpretation of seismic profile B09-23. In this section, the faults on both sides shows similar fault angles although they are overall slightly higher on the eastern flank. On the western flank, F5 appears to be curved at depth in a concave-up geometry. F2 shows major rotation and may intersect with F3 at depth. Purple line = seabed reflector, green dashed line = rough basement reflector, black lines = interpreted faults. TWT = two-way travel time.*

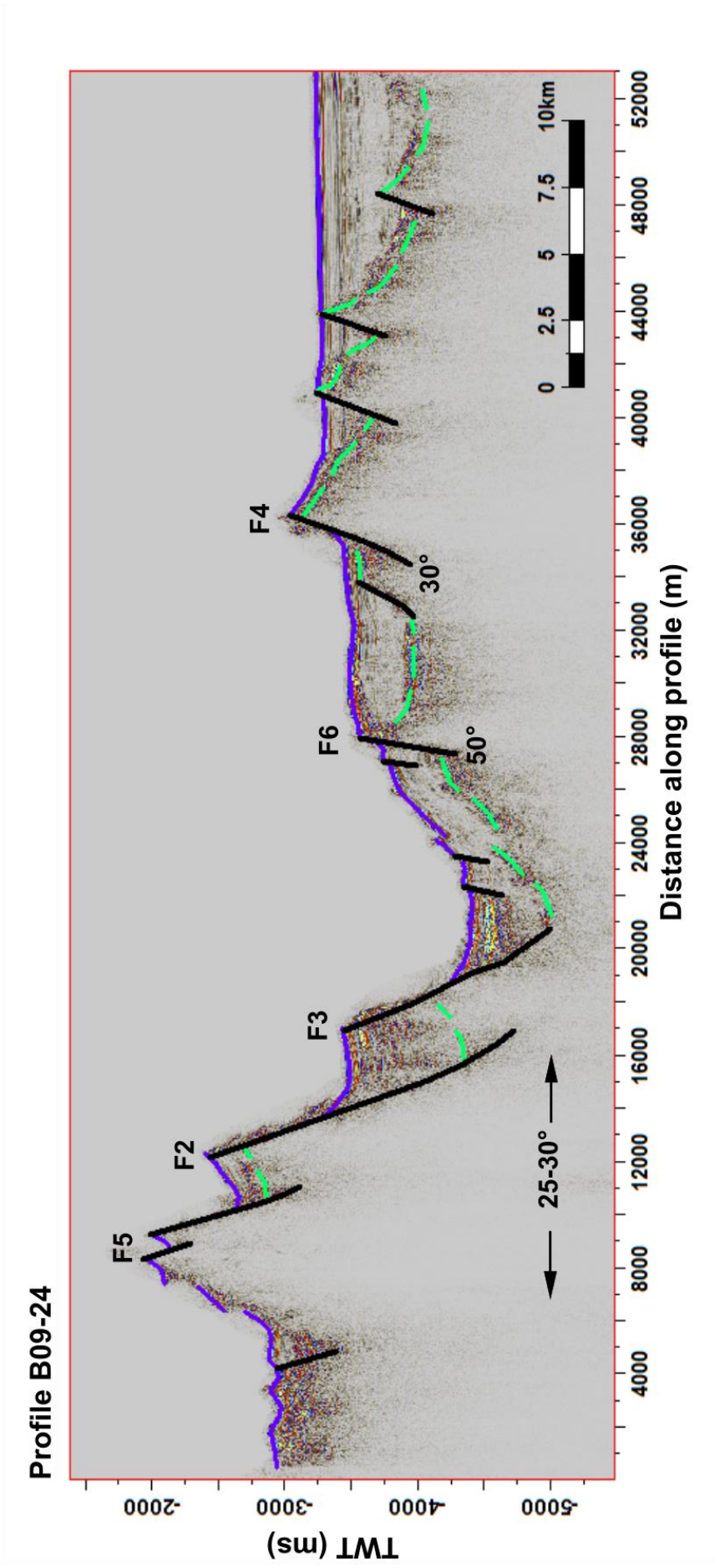

Figure 6.17: *Interpretation of seismic profile B09-24. The western flank displays major faulting compared to the eastern flank, where only minor faulting is present, related to formation of the abyssal hills. Apart from F6, fault angles are overall very similar. F2 is here less visible. Instead, F5 takes over as the dominant fault.*

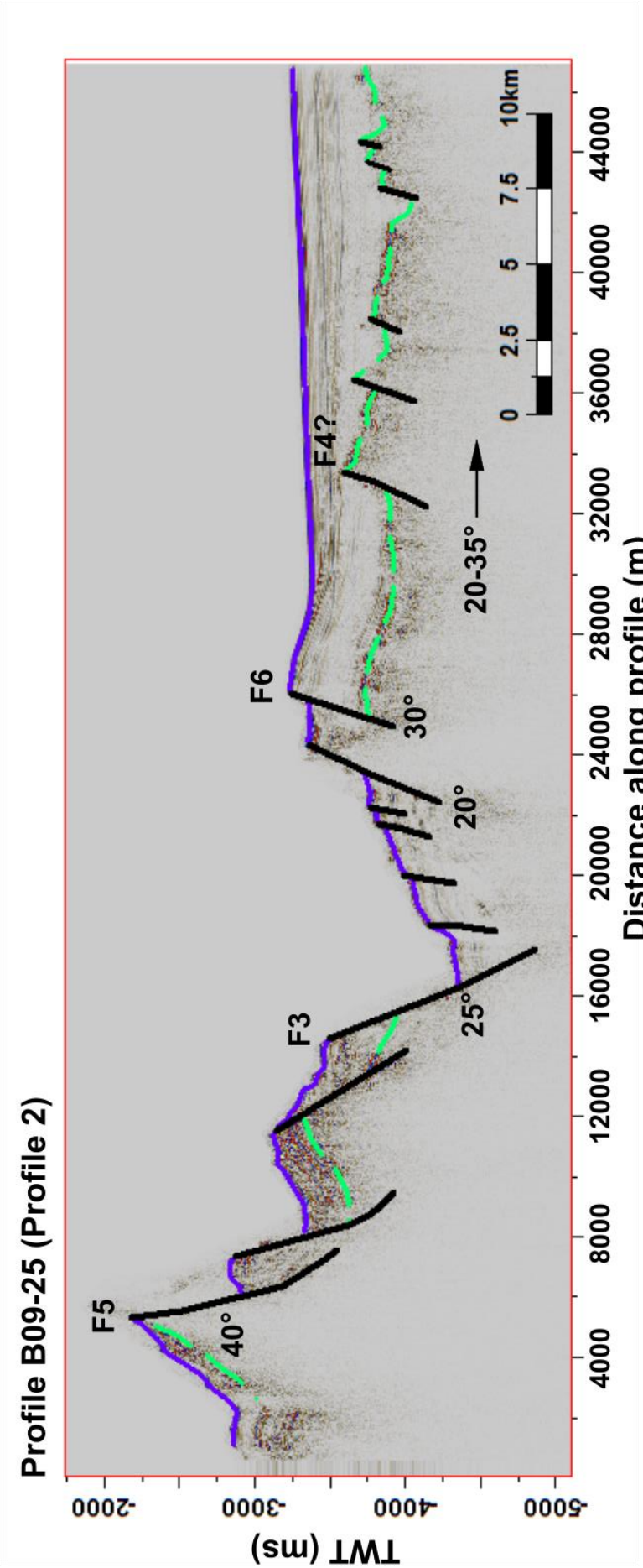

Figure 6.18: *Interpretation of seismic profile B09-25. F5 shows major rotation. F3 is a major valley wall-bounding fault, reaching beneath the axial valley, which here is very narrow. Fault angles on the eastern flank are relatively homogenous. Slight rotation of F6 is inferred by the tilted sediments.*

6.3 Earthquake Data Analysis

442 seismic events from NORSAR's regional earthquake databased were analyzed and potential relationships interpreted. As expected, seismic activity is focused along the ridge axis, however, the recorded events are asymmetrically distributed, favoring occurrence on the eastern flank (Figure 6.19a). Here, events are spread out evenly across the whole flank displaying all magnitudes, whereas events on the western flank occur closer to the valley walls, with only a few outliers. Magnitudes are slightly different as well, displaying mostly intensities above 3 on the western flank. The events with the highest magnitudes (> 4.5), however, do not have a preferred flank, but are overall located close to the axial valley.

Using a distance function (Figure 6.19a), the density and distance between individual events can be visualized. It shows clearly that the overall distance between events on the eastern flank rarely exceeds 5 km, for the most part even staying within $2-3$ km of each other. The western flank, on the other hand, rarely displays distances lower than $5-10$ km, with the highest densities along the valley walls and a scattered cluster around CC1 and CC2.

In order to get a more complete picture, the magnitude values of all events were interpolated and evaluated with respect to the seafloor bathymetry using spatial statistics. This yields a map that highlights areas as a function of magnitude, depending on the intensities of the individual events that occur in the area (Figure 6.19b). The map shows that the area of CC1 and the volcanic edifice southeast of F8 accommodate events with overall higher magnitudes than other areas of the ridge, if only by a small margin, despite the overall number and density of events being much lower than compared to the area and on the opposite side of the valley. It also appears as if the magnitudes on the western flank are overall slightly higher, although this is not as clear from the data. Areas with high magnitudes are found on both sides of the axial valley, but are smaller and less continuous on the eastern flank when compared to the western flank, where they stretch over larger areas.

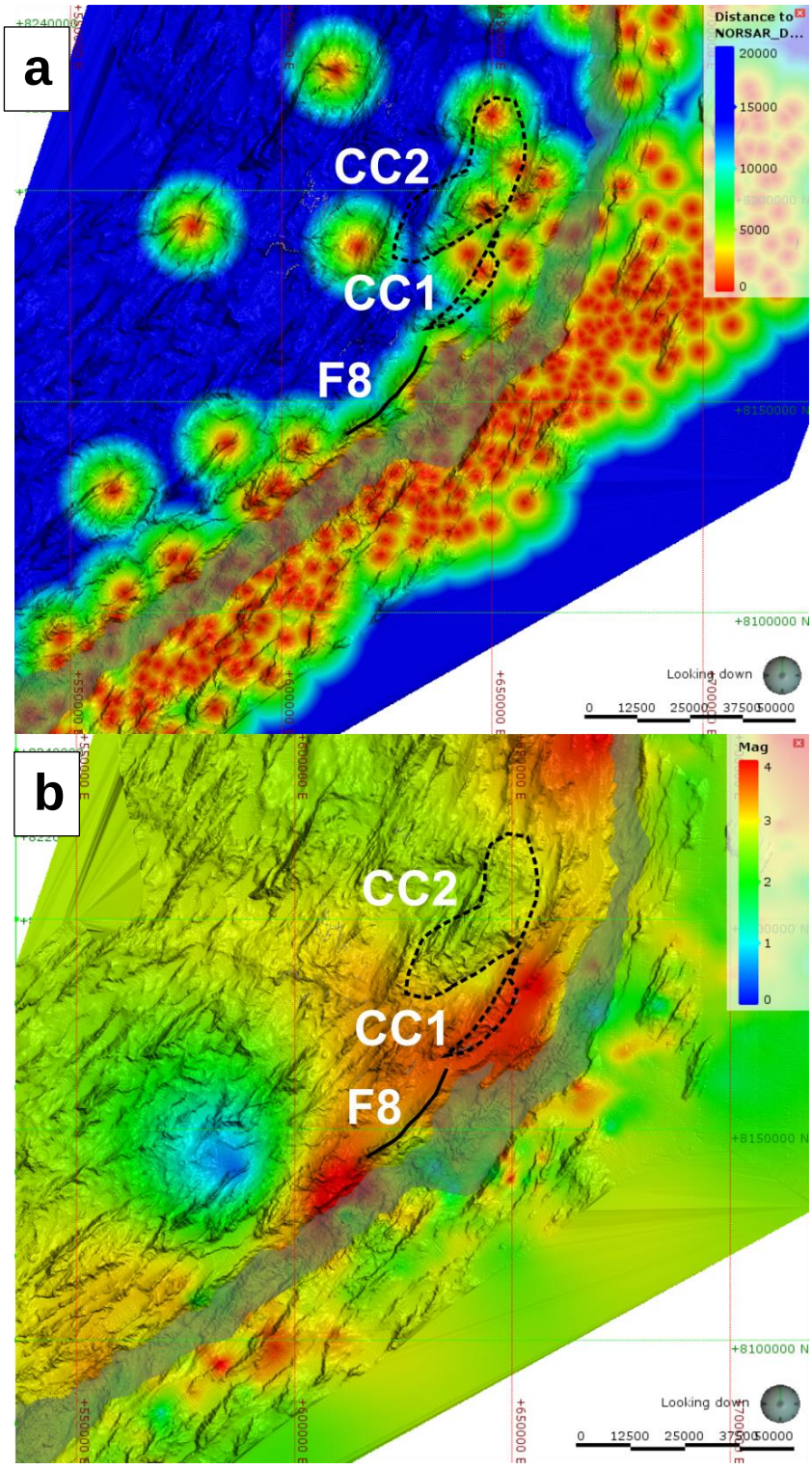

Figure 6.19: *Seismic activity in the Study Area.* ***(a)*** *Distance interpolation of the seismic event data evaluated with respect to the surface bathymetry. The redder an area is, the smaller the distance is between occurrences, making it easy to see how the events are focused on the eastern flank and the close to the valley walls on the western flank.* ***(b)*** *Spatial statistics of magnitude, showing overall higher magnitudes around CC1 and the volcanic edifice southeast of F8. Red spots indicating higher magnitudes are found on the eastern flank as well; however, these are small and disseminated spots. In contrast, large orange and red areas are found on the western flank, indicating overall higher magnitudes, although only weakly. Valley floor is shaded.*

6.4 Copper Hill

The Copper Hill area (Figure 6.20) is located just outside of the primary study area, roughly 70 km and 220 km southwest of AVR4 and Loki's Castle, respectively. Mineralized breccia samples were recovered from the footwall of a major rotated fault (red triangle) which from here on will be termed CHF. The fault displays a marked breakaway ridge sloping outward at about 18°, while trending roughly 050N. The fault is cut off from the axial valley by a newer, large normal fault trending in approximately the same direction. Two AVRs are in close proximity of the CHF, just 15 – 20 km southeast and southwest, residing in the axial valley. They trend in the same direction as the faults on the flank. A volcanic abyssal hill with a steep inward-facing scarp in present between the AVR and the fault off-cutting the CHF.

A dome-shaped structure with a linear ridge is located directly behind CHF, displaying a similar surface texture as CC1 and CC10. Another large ridge is located directly behind this one. About 20 km west of CHF is a large dome-shaped structure with an outward-facing breakaway ridge and shallow inward dipping central section. An elevation profile of the area with interpreted structures is provided in Figure 7.3b.

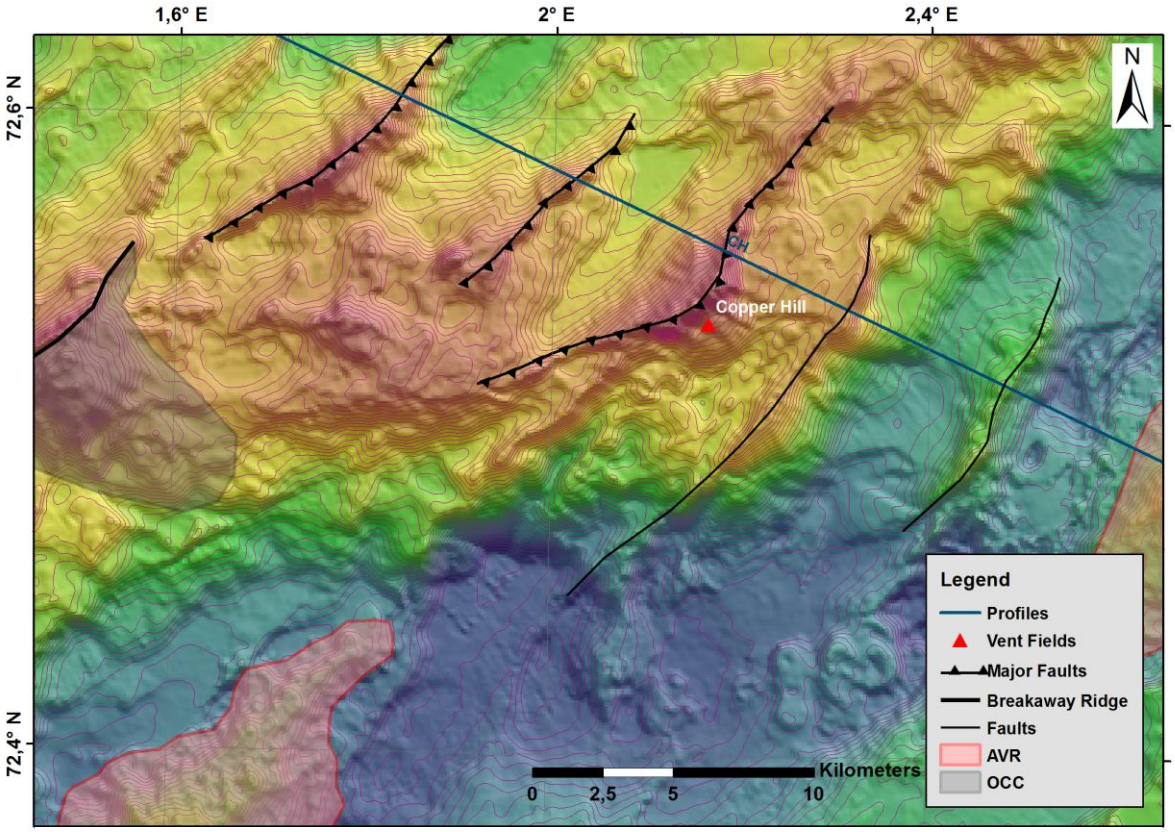

Figure 6.20: *Close-up of the Copper Hill area. The samples were recovered from the inside scarp of a rotated, curvilinear ridge. Multiple dome-shaped structures and ridges are present in the area. A core complex is found 30 km west of Copper Hill. Contours are at 50 m intervals.*

6.5 3D-Modeling of Detachment Faults

For visualization purposes, a 3D-model of the study area was created using the XYZ-DTM source data and LeapfrogGeo, followed by modelling of the detachment surfaces associated with the identified core complexes (Figure 6.21). Cross-sections were then generated for profiles 1 to 9, which cover the area where core complexes have been found. An example is provided in (Figure 6.23). The seven detachment faults were first identified on the surface and their terminations toward the axial valley were then traced in ArcGIS. Initially, the hopes were to use the seismic event data to infer a fault plane in the subsurface, but the data proved to be insufficiently accurate and dense to make such inferences (Figure 6.22). Because no measurements or structural data for surface modelling is available, the models are based on descriptions from available literature (Buck, 1988; Smith et al., 2008; Tucholke et al., 1998). They are therefore purely conceptual and only meant as a means of visualization.

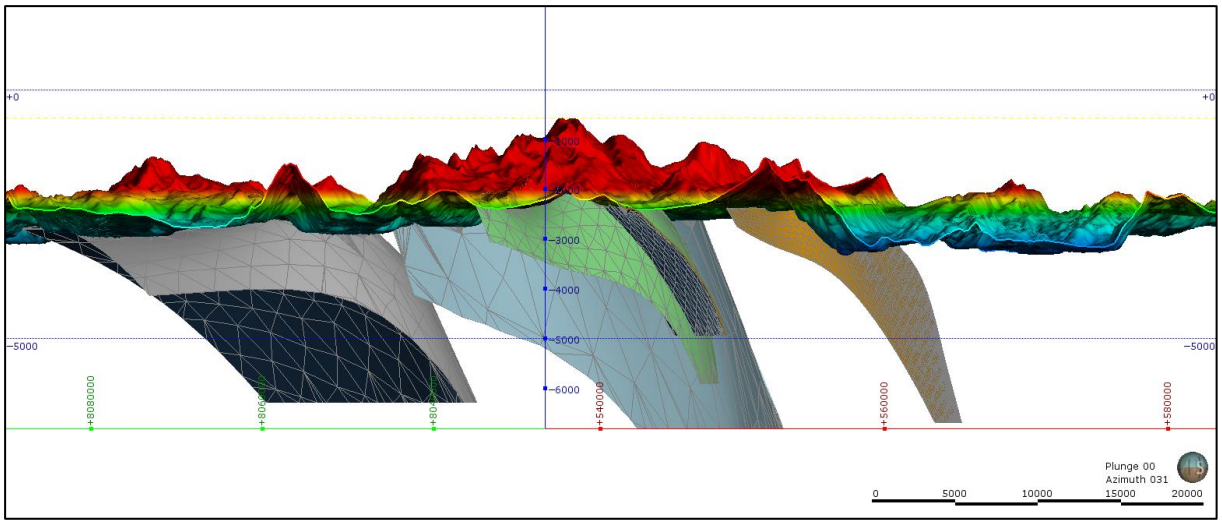

Figure 6.21: *3D model of the seafloor topography and modelled detachment surfaces. Brown = DF1, green = DF7, blue = DF2, grey = DF9. 3x vertical exaggeration.*

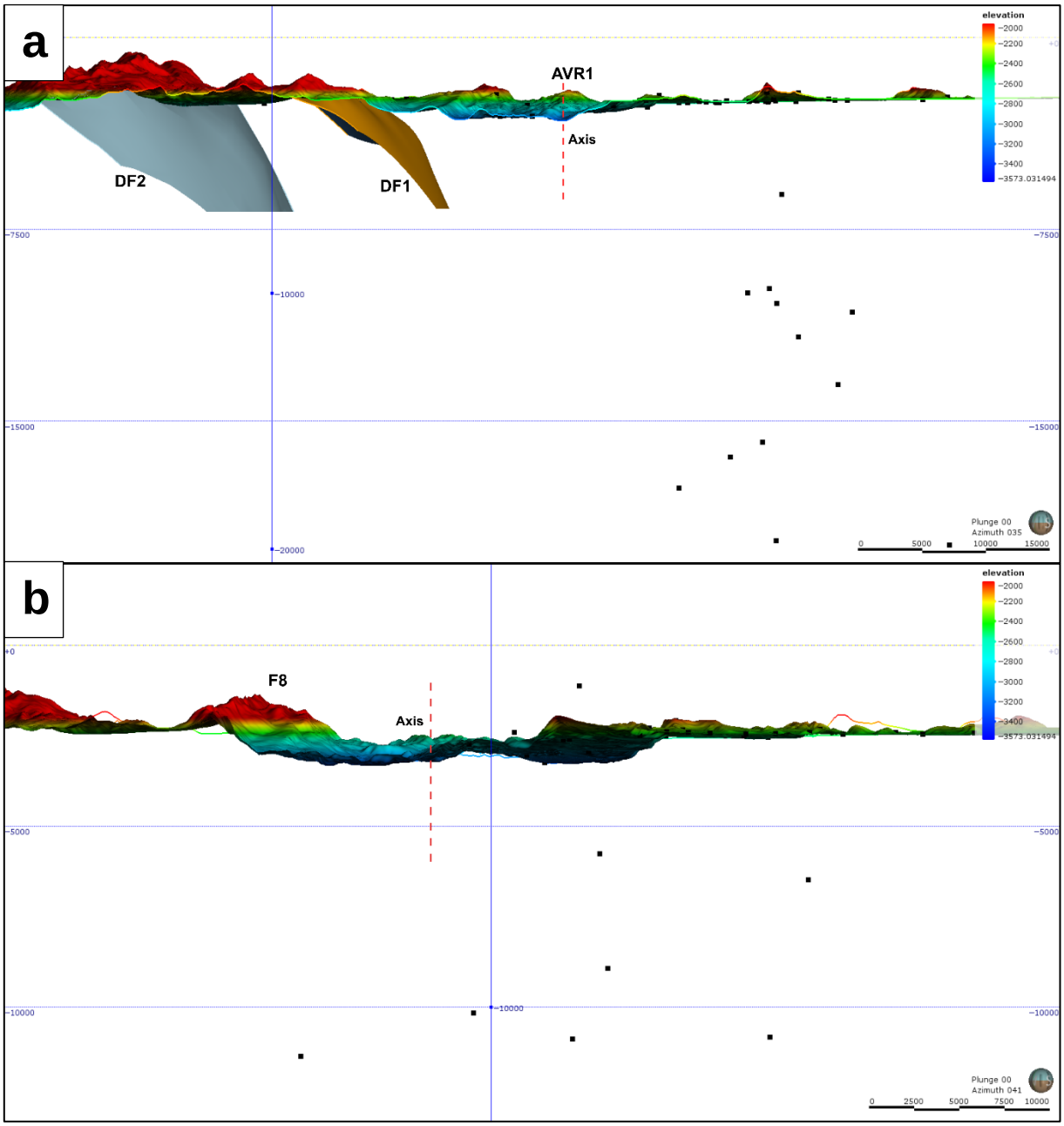

Figure 6.22: Vertical profiles of DF1 and DF2 (a) and F8 (b) showing how scarce and scattered seismic events (black dots) are in the area. The sections are sliced pieces of the bathymetry and are as wide as the respective faults, so they display all events present along the faults' extents. Such events, if sufficiently accurate and dense, could be utilized to infer fault planes. Unfortunately, the available data for this study were not appropriate for this.

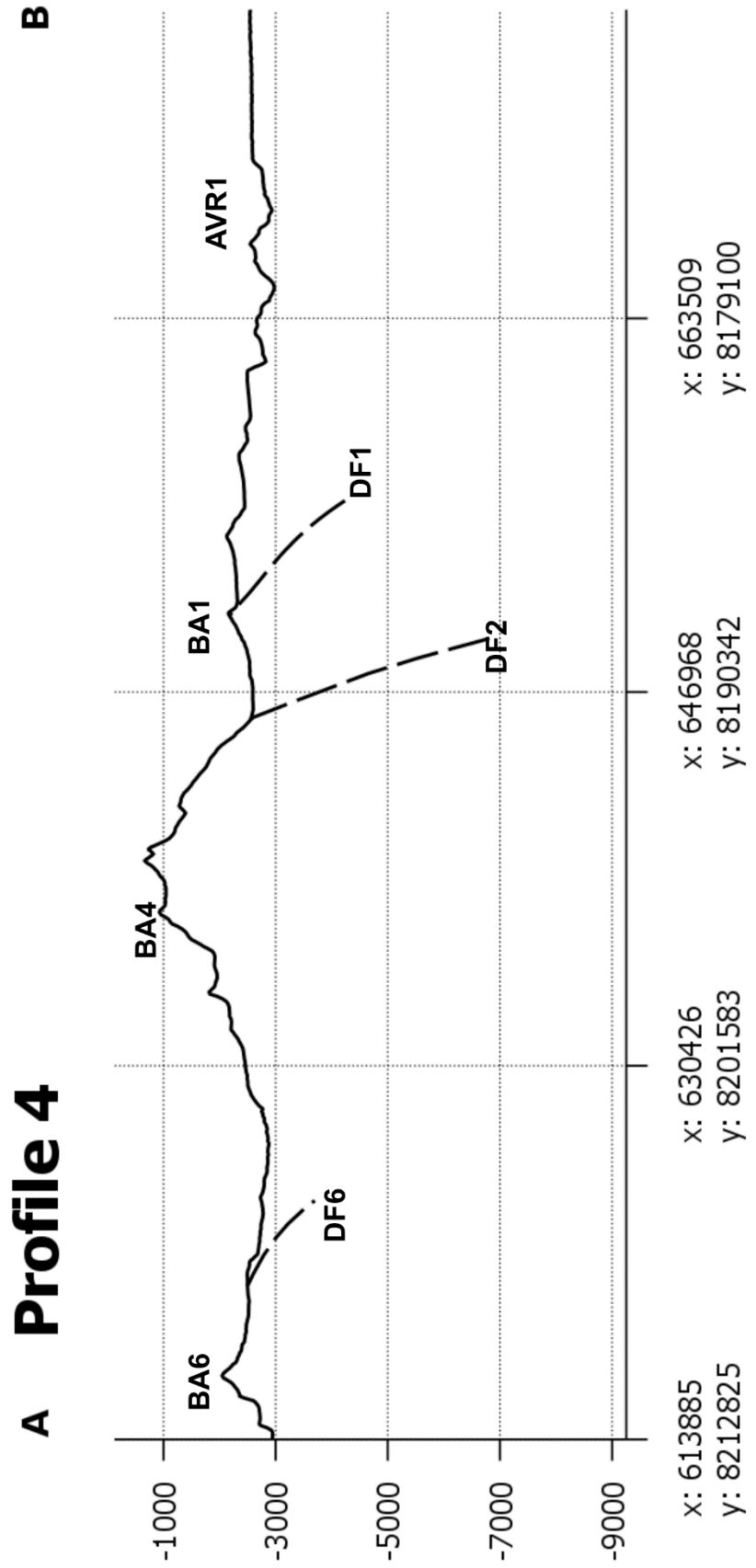

Figure 6.23: *Cross-section of profile 4 generated from a 3D-model of the seafloor topography and detachment surfaces using LeapfrogGeo. The remaining cross-sections can be found in Appendix B.*

7. Discussion

7.1 Magma Supply along the Ridge

The overall, and comparative, morphology of the ridge flanks changes from north (profile 4) to south (profile 13), which has implications for the overall geological environment in which they formed. As outlined in chapter 4.1.1, this environment is often described and derived based on the amount of available magma supply beneath the ridge axis and the associated mode of spreading (Buck et al., 2005; Schouten et al., 2010; Tucholke et al., 2008). Accordingly, the change from a distinctly asymmetrical distribution of structural relief and faults in the north to a far more symmetric division across the axis in the south and frequent abyssal hills, interpreted as remnants of earlier AVRs, suggests an overall increase of magmatic influence from north to south.

Formation of detachments faults is believed to be directly related to the amount of available magma beneath the ridge axis and the amount of lithospheric accretion accommodated by magmatic processes (denoted as $M = 0-1$). Values between $M = 0.3-0.5$ are reported (Buck et al., 2005; Tucholke et al., 2008) as the optimal balance between magmatic and tectonic processes to facilitate long-term slip and development of detachment faults. It has, however, also been shown through modeling (Schouten et al., 2010) that periodically very low magmatic components, even as low as $M \approx 0$, are possible during detachment fault formation. In this latter model, M is regarded as variable through time, an aspect not taken into account in previous models, which were based on a constant value of M (Buck et al., 2005; Tucholke et al., 2008). Despite this, it also seems clear from the modelling results of Schouten et al. (2010) that periods of higher magmatic activity are still required, and when considering the overall formation process, average amounts of $M = 0.3-0.5$ seem adequate for long-term slip and formation of detachment large-scale detachment faulting.

Under such conditions, an initiated detachment fault will accommodate roughly half of the plate separation, while the remainder is taken up by magmatism. Thus, the asymmetric morphology of the northern section of the study area, coupled with the distribution of identified core complexes and large, rotated normal faults, suggests a significant tectonic component. The area, however, also implies a magmatic component, as is evident by the presence of the AVR in the axial valley. Bruvoll et al. (2009) suggested that sediment deposition in the area in the surrounding area initiated around 1.3 My ago, but also described observations where sediments in the rift valley appeared to be overprinted by recent lava flows, implying that volcanism must

have occurred recently. Furthermore, the youngest sediments in the axial valley around the AVR were deposited in the last 0.2 My, whereas the top of the AVR shows no sediment cover (Bruvoll et al., 2009), suggesting that the recent, uppermost lava flows were formed in the last 0.2 My.

The active high-temperature black smoker field at Loki's Castle also implies a sufficient heat source beneath AVR1 in order to form the black smoker deposits. Overall, however, the observed features suggest that the northern area around AVR1-2 experiences co-occurring magmatic and tectonic extension and therefore precludes complete tectonic dominance. An average magmatic component of $M = 0.3 - 0.5$ as suggested by Tucholke et al. (2008) and Buck et al. (2005) should therefore be a reasonable assumption (Figure 7.1b).

At $M > 0.5$, most of the lithospheric accretion is accommodated by magmatic processes and faults will migrate off-axis, eventually becoming inactive due to formation of newer faults because the fault strength increases as the lithosphere cools (Buck et al., 2005; Tucholke et al., 2008). Faulting should then take the form of volcanic abyssal hills distributed roughly symmetrical across the ridge flanks (Tucholke et al., 2008), as is observed in the lower parts of the study area, around AVR3 – 4. The frequent occurrence of volcanic abyssal hills on both flanks and the complete absence of core complexes or major, rotated normal faults as found further north, indicates a higher magmatic influence in this area ($M > 0.5$). Models by (Tucholke et al., 2008) using $M = 0.7$ produce a comparable ridge morphology as observed in profile 11 and 13 (Figure 7.1a).

Models from the MAR show that the ridge can be divided into segments that, on the scale of 10 – 100 km, are more magmatically active toward their centers and less magmatically active toward their ends (Shaw & Lin, 1993). Less magmatic influence will change the isotherms below the ridge axis, thus deepening the brittle-ductile transition and favoring stronger tectonic processes (Harper, 1985; Shaw & Lin, 1993). Associated with this division is a widening and deepening of the axial valley toward segment ends and a narrowing and shallowing toward segment centers (Shaw & Lin, 1993). As such, each segment is thought to have its own focused mantle upwelling in the center where magmatism dominates. Further, the observation of core complexes at the inside corners of such segment ends near transform faults has been correlated to the indicated tectonic dominance (e.g. Tucholke et al., 1998; Tucholke & Lin, 1994).

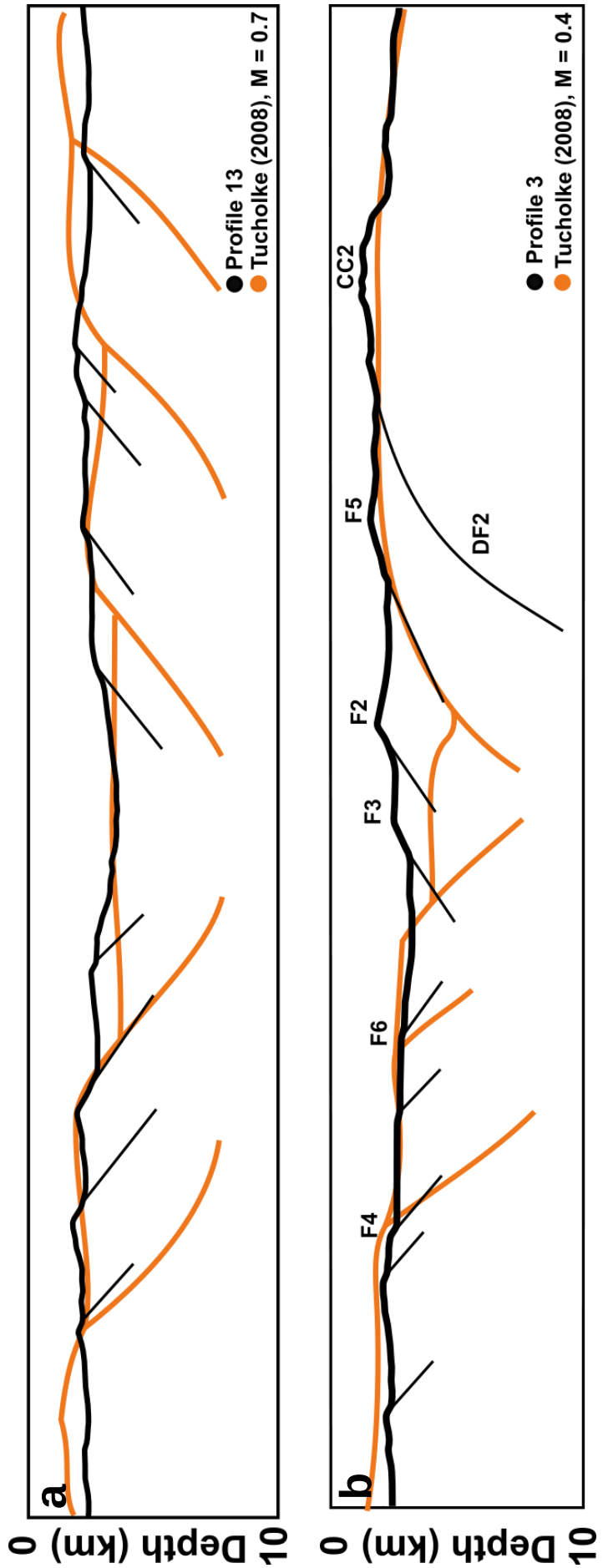

Figure 7.1: *Comparison of the Mohn's Ridge (black) and models generated as a function of M (orange) (Tucholke et al. (2008). No vertical exaggeration. Profile modified from Tucholke et al. (2008)* ***(a)*** *Profile 13 in the south compared to topography modelled using M = 0.7: The topographical expressions of the two profiles are comparable, both showing consecutive inward-facing fault blocks and similar fault angles, effectively forming a "staircase-morphology". New seafloor will in this scenario be formed dominantly by magmatic accretion in the axial ridge center, after which the magmatic seafloor will be progressively transported off-axis by new faulting.* ***(b)*** *Profile 3 compared to topography modelled with M = 0.4: The topographies are comparable, both showing a major detachment fault on one flank and smaller, consecutive faulting on the other flank. The difference here is that the (inferred) DF2 fault at depth no longer roots beneath the valley, as inward-jumping of later faults cut off the detachment fault and made it inactive. Note that profile 3 has been mirrored in order to achieve matching flank orientations.*

Following this theory, each AVR should represent a segment center where the axial width is small, followed by progressively less magmatic influence with distance and a wider axial valley. The identified AVRs in the study area display lengths about 20 – 35 km with roughly the same distance between them (a notable exception here is the distance between AVR1 and AVR), so the scale should be sufficient for such segmentation. The discontinuous nature of the AVRs marking focused mantle upwelling, along with the en-échelon behavior caused by non-transform offsets should be an appropriate segmentation criterion. However, no widening of the axial valley is observed and intermittent magmatic activity is visible on the valley floor between AVRs. Still, a transition from an overall major tectonic component and asymmetric spreading in the north to dominantly magmatic and symmetric spreading in the south is clearly present.

7.2 Faulting Style and Link to Hydrothermal Activity

7.2.1 Detachment Faulting

Deep-rooted detachment faults are believed to play an important role in the circulation of hydrothermal fluids and formation of sulfide deposits at mid-ocean ridges. The active TAG hydrothermal field, for instance, is located in the hanging wall of an active detachment fault, where the fault is thought to scavenge heat from large depths beneath the ridge axis (~ 7 km) (de Martin et al., 2007), and the ultramafic rock-associated Logatchev hydrothermal field is likely related to a detachment fault which focuses heated fluids away from the axis (Petersen et al., 2009). Further, McCaig et al. (2007) have demonstrated that detachment faults have the ability to focus large amounts of heated black smoker fluids and proposed that they should be able to produce different types of hydrothermal fields, both close to the axis (e.g. TAG), and further off-axis as ultramafic-hosted fields (e.g. Rainbow, Logatchev) as the detachment fault evolves. The model proposes an early stage in which heated circulation is driven by gabbroic intrusions below the detachment footwall close to the ridge axis followed by discharge through permeable basaltic lavas in the hanging wall, leading to a TAG-type deposit. As the detachment matures, the gabbroic bodies will cool and move off-axis, after which point flow and discharge will happen through an ultramafic-rich footwall, resulting in a Rainbow-type deposit (McCaig et al., 2007).

The identified core complexes and detachment faults in the study area are all located off-axis, cut-off from the valley by newer normal faults, which are variably rotated. The

combination of the flattening of the central dome and the cut-off by later normal faults suggests that the detachment faults likely are all inactive. However, even though a detachment fault may be inactive, this does not necessarily mean that it cannot continue to act as a fluid pathway, as circulation at mid-ocean ridges is suggested to only gradually decrease, until a crustal age of around 10 My due to fracture sealing and reduced thermal gradients (Klingelhöfer et al., 2000). At the Mohn's Ridge, the location of this crustal age is inferred from the study of Klingelhöfer et al. (2000), and is roughly at around 50 km from the ridge axis at the central section of the ridge. Accordingly, the further off-axis, the less permeable the fault and crust are, meaning that core complexes and detachment faults well within this range (e.g. CC1, CC7 and CC10) could still focus hydrothermal fluids even if they have been cut off from the valley by newer faults.

Corrugations may indicate more mature core complexes, as they are thought to be made visible when the detachment faults is exhumed (Smith et al., 2006; Tucholke et al., 2008), an observation that has been used to explain and support the young age of the non-corrugated TAG area (de Martin et al., 2007). The origin of corrugations is still debated, but has been linked to "continuous casting", or molding, of a weaker footwall by a stronger hanging wall as the fault emerges (Spencer, 1999), and an irregular brittle-ductile transition related to the distribution of magma intrusions beneath the ridge axis (Tucholke et al., 2008). In the latter case, the initial fault will be planar at the surface but corrugated at depth, meaning that exposed corrugations at the seafloor should indicate a degree of maturity and longevity of the detachment fault. In this case, if a detachment surface displays corrugations, it should indicate that the fault has rooted in the brittle-ductile transition. It also means that magmatism should be present during detachment fault formation, an idea that is supported by the intermediate levels of magmatism ($M = 0.3 – 0.5$) that are likely required to form detachment faults (Buck et al., 2005; Tucholke et al., 2008). Once the corrugations have been established by the irregular transition zone, Tucholke et al. (2008) further suggested that the cooler hanging wall could continue to mold the footwall as per the "continuous casting" concept introduced by Spencer (1999).

In contrast to the basalt-hosted TAG-field, the ultramafic-hosted Rainbow-field should, according to the previously mentioned evolutionary deposit model for detachment faults (McCaig et al., 2007), be relatively mature. If this is the case, then corrugated detachment surfaces located off-axis could indicate mature core complexes, which in turn could host ultramafic hydrothermal fields, given that fluid circulation has been taking place.

In this context, CC1 and CC2 are of particular interest, as sampling from their exposed surfaces has already confirmed that their footwalls indeed host ultramafic rocks. The presence of serpentinites indicates a fluid component, hydrating peridotite at temperatures up to 400 °C

and promoting serpentinization (Früh-Green, 2005). If this process took place while the detachment fault was active, it could indicate focusing of hydrothermal circulation during detachment fault formation and potential formation of deposits. On the other hand, it has also been suggested that the lower-than-average upper mantle velocities beneath the Mohn's Ridge axis may be caused by a volume fraction of about 10 – 40 % serpentinite within the lower crust and upper mantle (Klingelhöfer et al., 2000). A detachment fault could therefore potentially exhume already serpentinized lower crust and upper mantle without the need to focus heated fluids along its surface. However, even if that is the case, the amount of serpentinization (10-40 %) indicates significant hydrothermal circulation, meaning that widespread and deep fracturing must have taken place. Deeply-rooted detachment faults have the ability to provide the required pathways and facilitate this circulation (McCaig et al., 2007). The approximate length of the detachment surfaces of CC1, CC2 and CC10 (4 km, >10 km and 5 km, respectively) (Table 2) are sufficient to reach the brittle-ductile transition, as the lower crust is located at roughly 1.6 km depth and the upper mantle at around 4 km (Klingelhöfer et al., 2000). Considering that the now off-axis detachment faults once likely were located closer to the valley walls and rooted beneath the axial valley at a time when they were actively accommodating extension, that corrugations likely indicate interaction in the brittle-ductile transition and that serpentinites were recovered from the surfaces of CC1 and CC2, it suggests that both detachment surfaces have experienced hydrothermal interaction during their lifespan.

Additionally, detachment faults often are accompanied by rafted blocks covering their surfaces, as is the case for instance with CC2, CC6 and CC7 (Figure 6.6b and Figure 6.7). Generally, rafted blocks can be explained by the flexural rotation model (Buck, 1988) as subsequent faults that form after the maximum rotation angle of the active part of the detachment fault has been exceeded. As such, the rafted blocks are parts of the original hanging wall, or valley floor, that has been cut-off by later faults before being transported off-axis and ultimately laid to rest on the detachment surface (Schouten et al., 2010). Later, a more significant period of magmatism may lead to the eventual termination of the detachment fault (Tucholke et al., 1998). The interpreted rafted block on CC2 displays indications of magmatic activity in the form of volcanic cones and craters (Figure 6.6b) supporting the idea that it once was part of the valley floor. Similar features are visible on CC6 and CC7 as well, although not as pronounced. The presence of these features suggests a magmatic influence during detachment formation which could have provided a heat source for potential hydrothermal circulation. If this is the case, then detachment faults with rafted blocks that display volcanic constructions could pose an attractive feature to look for in the search for hydrothermal SMS

deposits.

7.2.2 Large Rotated Normal Faults

Large-scale normal faults could play a similar in the formation of SMS deposits, given their dimensions and location close to the axial valley, often as part of the valley walls. In the study area, two major normal faults (F7 and F8) stand out due to their overall dimensions, role as part of forming the valley wall and their proximity to axial volcanic ridges. On the seafloor bathymetric map, F8 immediately stands out as a major high-relief topographic element as part of the western valley wall, roughly 10 km west of AVR2 (Figure 6.8b). The scarp of this fault is about 1500 m tall at its central high, measured from the valley floor. The fault is severely outward-rotated and the flat area behind it shows a slight depression and could develop into a flexural basin. Additionally, a mass wasting plateau in the footwall of F8 hosts the inferred Mohn's Treasure sulfide deposit, and the fault plane has earlier been proposed as a likely fluid path way during its formation (Pedersen et al., 2013). Although, given the very steep termination of the ledge, it is probable that the ledge is a product of mass wasting in combination with tectonic, as also described by (Ludvigsen et al., 2017). The enormous size of the fault scarp in combination with the large amount of rotation of the outward-facing slope and its position in the valley wall suggests that the fault is an immature detachment fault, which eventually might develop a central dome-shaped core complex if the fault is allowed accommodate further extension. The presence of multiple core complexes (CC7, CC8, CC10) to the west of F8 demonstrates that the area is prone to formation of these structures.

In the case that F8 is an incipient detachment fault, it may be deep-seated and could thus be able to extract sufficient heat to facilitate hydrothermal circulation to form a sulfide deposit in its vicinity (Figure 7.2). Smaller-scale lineations, interpreted as internal faulting, are present on the inside scarp and could add further permeability to allow easier and more widespread fluid circulation. Additionally, volcanic cones are present on the valley floor and the fault scarp. The analysis of sulfide samples recovered from the Copper Hill area (Nygård 2004, as cited in Pedersen et al. 2013) demonstrated that such faults on the MR have the ability to focus hydrothermal fluids at black smoker temperatures during their formation. Given the similarities of the two areas, the idea that similar circumstances may result in hydrothermal circulation is not too distant. The observations from ROV and AUV dives to AVR2 during the 2016 MarMine cruise support this idea, as widespread pillow lavas and only little sedimentation were observed, suggesting that recent magmatic activity has occurred. If this is the case, then this could provide a heat source for the hydrothermal fluids. It is, however, not possible to constrain the age of the

lava flows with the currently available data, although the observation of volcanic structures on the inside slope and valley floor in front of the F8 fault scarp, indicate that some magmatic activity must have occurred during fault formation.

The activity of the fault could be relevant for current hydrothermal activity, as ongoing deformation may open new fractures to further facilitate active fluid circulation. Despite the seismic data not yielding an as-definitive indication for potential concentration and focused swarms of activity as was initially hoped, the F8 fault is probably still active. The overall higher magnitudes of earthquakes in the area of CC1 and a few kilometers south of F8 could indicate that high intensity brittle deformation is taking place close to the western valley walls in this area. The fact that F8 is a major fault located within this area could mean that the overall higher intensity of events is connected to the faulting process, as earthquake magnitudes decrease rapidly with decreasing dimensions of the structural feature (Rundquist & Sobolev, 2002). Seismic activity will be focused along the fault plane dipping beneath the axis as it accommodates extension (Rundquist & Sobolev, 2002). The observation that the seismic activity appears to be focused on the inside scarp of the fault and not further out on the ridge flank, coupled with an overall higher intensity in this area, suggests that the fault is active. The depth of the events could therefore theoretically be used to infer the approximate geometry and orientation of the fault surface (de Martin et al., 2007; Escartín et al., 2008), if they are sufficiently accurate.

It should, however, be noted that the highest magnitude events do not occur on the fault itself, but rather to the north and south of it. This could either be because the fault is inactive and brittle deformation therefore does not take place or because of poor positioning accuracy, as teleseismic earthquake epicenter constraint is very inaccurate, typically on the order of 10 – 20 km (Rundquist & Sobolev, 2002). In this situation, it is likely that the latter is the case, as is also clear from the seismic event metadata, where the median errors for the major axis, minor axis and overall error ellipsoid of the epicenters are 44.5 km, 17 km and 2400 km^2, respectively, thus adding a significant amount of uncertainty to the location of the events. The observation, however, that the fault has not yet been cut-off by later faulting and that high-magnitude seismic events are occurring in the general area may support the idea that it is still active.

One final question to answer with regard to Mohn's Treasure is where the actual sulfide deposit is located. Expeditions that investigated the nature of the area have only been able to infer a deposit based sampling of small amounts of sulfides and fragments with fluids channels from the mass wasting area (Ludvigsen et al., 2016; Pedersen et al., 2013). However, no conclusive indications have been found that would allow us to determine from where they

originate. It is entirely possible that the mass wasting event has destroyed a previous deposit, or that only parts of it were affected and that the deposit can be found at other locations along the fault scarp. At present point in time, however, without more information, it is entirely speculative to try to determine where the deposit is, or was, located. A 3 meter long gravity core sample was taken on the ledge during the 2016 MarMine cruise. The core logging results will yield more insight into what is find deeper beneath the surface, but the results are still pending.

The situation for the mineralized sulfide breccia at Copper Hill is comparable to the circumstances at F8 and Mohn's Treasure (Figure 6.20). The sulfide samples were recovered from the footwall of a major rotated normal fault, here termed CHF, beneath a curve-linear ridge (Pedersen et al., 2013) displaying an outward-facing slope dipping at 18°. The amount of rotation implies that the fault probably steepens at depth (Buck, 1988) and that it therefore may represent an incipient detachment fault. Behind the fault is a dome-shaped structure that in its surface morphology resembles CC1 and CC10, with an outward-facing slope and smooth inward-facing central slope. This structure, along with another massif approximately 30 km west of Copper Hill has been interpreted as core complexes (Pedersen et al., 2013). The CHF fault from which the sulfides were recovered is cut-off by a parallel fault toward the ridge axis. Given the rotation and the inferred convex-up geometry at depth, it is possible that the two faults intersect at their nucleation point (Buck, 1988), and that the cutting fault could have develop into a rafted block if accommodation of extension had continued (Figure 7.3b). Pedersen et al. (2013) have suggested that the CHF fault represents an incipient detachment fault which is either still active and thus very young or that is has been aborted, possibly due to activity from the AVR further to the east. Only about 5 km west of the AVR is an elongate ridge, displaying distinctly hummocky terrain and a steep inward-facing scarp and it is therefore likely that the CHF detachment fault was aborted in favor of this rifted AVR slice.

The similarities of the environments in which Copper Hill and Mohn's Treasure reside are comparable. Both are likely related to major normal faults which have been rotated as a result of continuous tectonic accommodation of extension, both environments feature core complex terrain and both are located in near proximity to an AVR. They only distinguish themselves by the sulfides that have been recovered from them, mostly chalcopyrite at Copper Hill and pyrite at Mohn's Treasure, and the probability that the Copper Hill fault likely has been aborted, while the F8 fault is still active.

F7 represents to be another major fault located in the western valley wall, about 5 km west of AVR1 and has formed a dome-shaped structure, along with a possibly rotated

breakaway ridge and a shallow basin behind (Figure 7.3a). However, the small amount of rotation and the frequent cross-cutting by smaller internal faults makes it unclear if this is an incipient or aborted detachment fault or simply an area uplifted by normal faulting. Roughly 2.5 km east of F7 is a larger normal fault, which may provide additional fluid pathways for the Loki's Castle field (Pedersen et al., 2013).

Despite this, the overall circumstances here are similar to the Copper Hill and Mohn's Treasure areas, namely a major normal fault that makes up the western valley wall, displays some internal faulting and is close to an AVR. The differences compared to the other two examples are the extreme proximity to the AVR and that the fault only displays minor amounts of rotation. Additionally, sulfide minerals have not been recovered from the fault, but rather from the active Loki's Castle black smoker site located on the AVR only a few kilometers away. There are some important aspects to consider in this area, the main one being that Loki's Castle is the only known active black smoker field known on the Mohn's Ridge. Furthermore, its location in the neo-volcanic zone means that it is volcanically hosted, which implies that an active magma chamber must present beneath the ridge, as is also evident from the recent lava flows on the AVR surface (Bruvoll et al., 2009). At first glance, this may seem similar to Copper Hill and Mohn's Treasure, but what makes it different is the fact that fluids at black smoker temperatures and compositions are currently being channeled through the crust of the neo-volcanic zone. The dimensions of F7 and the cross-cutting of smaller normal faults may have provided a fractured crust in this area, which could enable hydrothermal circulation if the fault manages to scavenge heat and fluids from beneath the AVR.

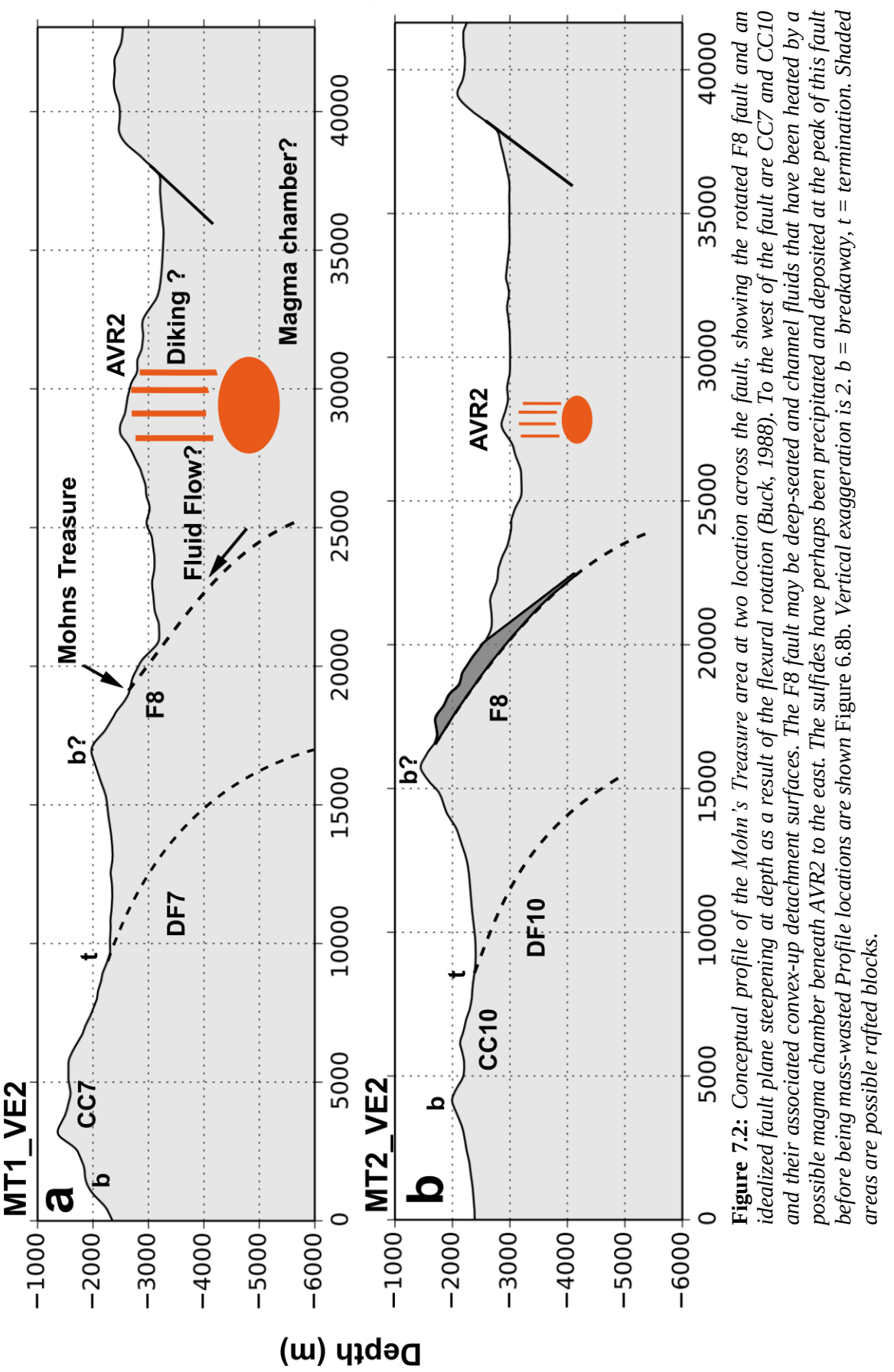

Figure 7.2: *Conceptual profile of the Mohn's Treasure area at two location across the fault, showing the rotated F8 fault and an idealized fault plane steepening at depth as a result of the flexural rotation (Buck, 1988). To the west of the fault are CC7 and CC10 and their associated convex-up detachment surfaces. The F8 fault may be deep-seated and channel fluids that have been heated by a possible magma chamber beneath AVR2 to the east. The sulfides have perhaps been precipitated and deposited at the peak of this fault before being mass-wasted Profile locations are shown* Figure 6.8b. *Vertical exaggeration is 2. b = breakaway, t = termination. Shaded areas are possible rafted blocks.*

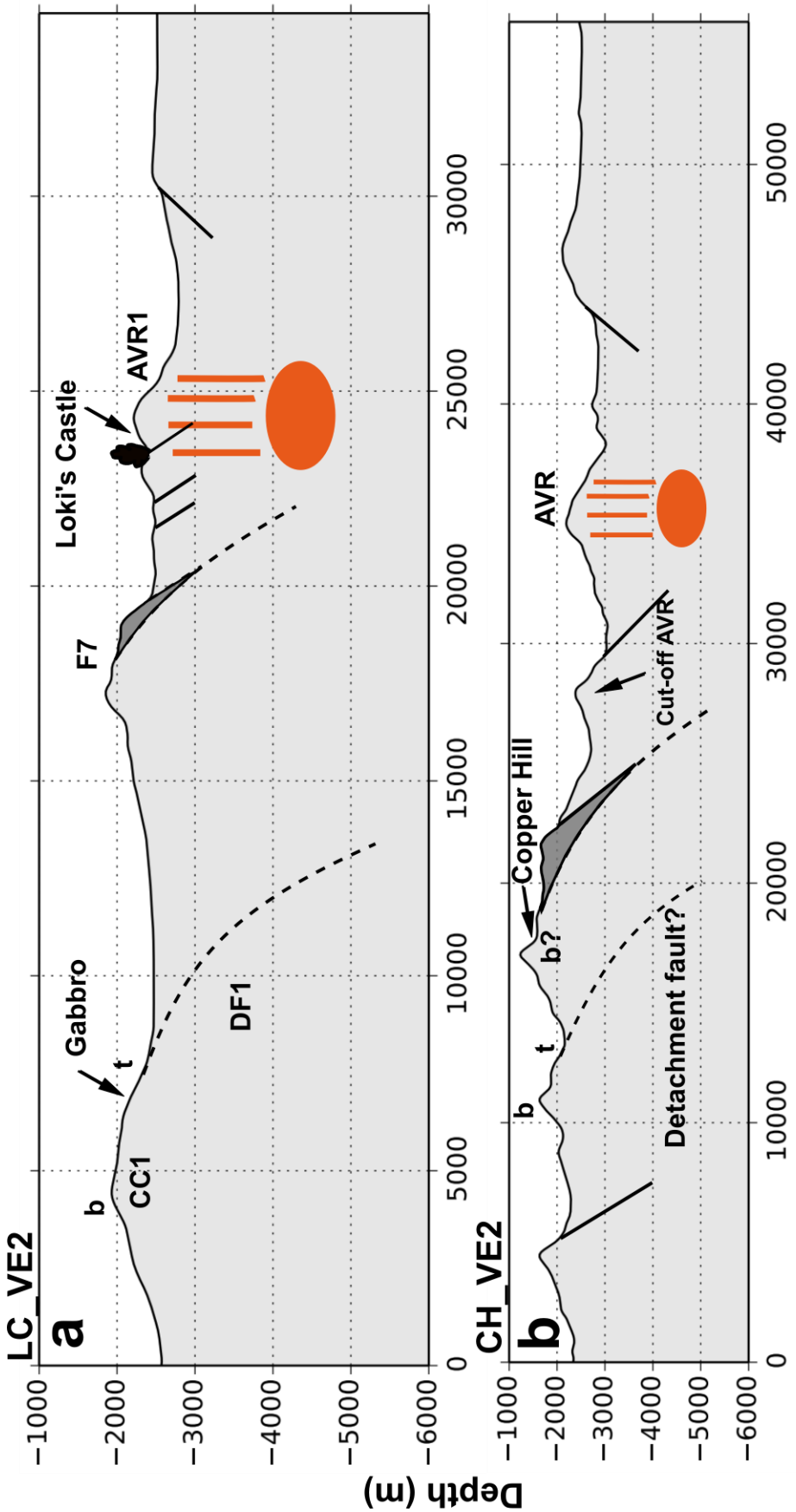

Figure 7.3: *Conceptual profile over the Loki's Castle* ***(a)*** *and Copper Hill areas* ***(b)****, showing the possible relationships between present structures. LC_VE2 visualizes the rotation of F7 and its proximity to the black smoker field on the AVR. The Copper Hill profile shows the possible rotated breakaway, followed by a rafted block and probable termination due to rifting of the AVR in the central valley. Profile locations are shown in* Figure 6.8a and Figure 6.20. *Vertical exaggeration is 2. b = breakaway, t = termination. Shaded areas are possible rafted blocks.*

7.3 Listric Faulting

7.3.1 Origin and Meaning

In its original form, as introduced by Eduard Suess, the term listric simply describes a curved fault plane, which he referred to as *listric planes* (Suess, 1909). Today, it seems the term *listric fault* carries additional implications with it, potentially making it challenging to use the term in certain situations. Listric faulting is nowadays often mentioned in association with curved faults flattening into a basal décollement (Allaby, 2013a; Bally et al., 1981; Wernicke & Burchfiel, 1982). In his original work, however, Suess did not mention any horizontal surfaces into which the faults flatten, perhaps because he simply did not have sufficient information to arrive at such a conclusion. However, since then, it might appear as if the term has evolved, to more or less include the associated structures, primarily an underlying horizontal detachment fault, or décollement. Nevertheless, this means that the term listric in its inception simply referred to a curved fault plane, as a distinction to the default fault planes, which were typically identified.

The challenge then, lies in determining at which point a planar fault can be deemed a listric fault. One could argue that listric and planar faults represent endmembers, where the former implies a curved fault flattening in to a basal décollement, along with its associated structures (e.g. Allaby, 2013a; Shelton, 1984; Wernicke & Burchfiel, 1982). The latter, on the other hand, would represent the typical planar and steep normal fault forming at angles $> 45°$, in accordance with Andersons Fault Theory (Anderson, 1905).

If, however, normal faults unavoidably become listric at depth (Jackson & McKenzie, 1983), then accordingly, all normal faults should essentially also be listric faults. The question then, is how faults falling in between the two endmember categories should be termed, and at which point a normal fault becomes a listric fault. Given a normal fault which is initially planar for a significant distance, but at depth displays decreasing dip, as could be the case for many faults in the study area, it would be counter-productive to immediately label it a *listric fault*, as this may also imply the presence of a basal décollement and associated structures. A possible description could simply be a “normal fault with a listric geometry” or a “listric plane”, in order to not give wrong impressions about the actual present circumstances.

The uncertainty about the termination of faults at depth adds an additional layer of complexity to this discussion, because it is often unknown how they behave and are terminated at depth. Harper (1985) suggested that they could either simply continue aseismically beneath

the brittle-ductile transition or flatten into a horizontal detachment, or décollement, above the mantle. Similar theories have also been suggested Shelton (1984). Accordingly, even though a fault shows only slight curvature on e.g. seismic imaging, it is very well possible that this weak curvature may continue until the fault eventually flattens out horizontally, or just "dies out". Unless this is known, however, and it is indeed the case that all normal faults inevitably will show a listric geometry at depth, then it would be appropriate to establish a distinction between listric faults that visibly and knowingly flatten into a basal horizon, and normal faults that simply show varying degrees of curvature at depth due to rheological constraints. Because, unless there is information or evidence to show how faults behaves at depth, it is simply uncertain and speculative to derive their eventual termination.

In summary, caution should be used when labeling and describing fault types and systems, so as not to cause confusion which may result from potential implications carried with the terms. Accordingly, in the following discussion, faults will be only be termed *listric faults* if they display significant curvature and their terminations, e.g. an underlying décollement surface, are known or inferable. Where this is not the case, normal faults displaying varying amounts of curvature will be described as faults with a listric geometry or listric fault planes, as originally introduced by Suess.

7.3.2 Listric Faulting in the Study Area

Listric normal faulting has been linked to extensional regimes, both oceanic and continental as an important factor which potentially could explain many observations, such as the presence of tilted dikes and frequent sampling of gabbros and peridotites (Karson & Rona, 1990; Roberts et al., 1993; Verosub & Moores, 1981). In the present study, three primary types of faulting structures were identified on the surface of the Mohn's Ridge: (1) Large-scale detachment faults with their associated core complexes, (2) Major rotated normal faults, and (3) Minor normal faults and fault-bounded volcanic abyssal hills. The challenge then is to determine to what extent these are listric, a problem which the following discussion aims to address.

The theory of Jackson & McKenzie (1983) regarding the behavior and geometry of normal faults at depth is here very central. Accordingly, practically all normal faults will at some point curve and become listric because of the inevitable rheological contrasts of the lithosphere, where shallow sections are more brittle and deeper section more ductile. Additionally, the geometrical constraint that no voids should form during rotation of the blocks (Jackson & McKenzie, 1983) further strengthens this theory. From this follows that normal

faults should be listric, especially if they are rotated.

Weakly curved surfaces which, if extrapolated, could be described as listric planes are visible on both ridge flanks on the interpreted seismic profiles. The fault blocks, especially on the western flank, also show signs of rotation, as is evident from the syn-tectonic sediment infill. Unfortunately, the seismic profiles do not penetrate through the basement, thus there is no imaging of the fault structures beneath. Also, the reflections close to the basement transition are often distorted and noisy, making a clear identification of horizons and discontinuities challenging.

On the western flank of Profile B09-24 (Figure 6.17), F5, F2 and F3 are stacked behind each other in a half graben arrangement, displaying similar rotation and fault dips. The planes have a listric geometry, and one could speculate, although this is not clear from the seismic, that the fault plane of F5 may intersect with F2, and perhaps even F3, if extrapolated. In that case, they would surely constitute a listric fault system. On the other hand, further north on profile B09-25 (Figure 6.18), F5 shows large amounts of rotation and an outward-facing ridge. Following Buck (1988), this should imply that its geometry beneath the surface might steepen, rather than flatten. As such, it may intersect with the next fault to the east before steepening, effectively forming a rafted block.

F3 displays only little to no rotation on both B09-24 and B09-25, but is weakly curved toward its visible termination beneath the ridge axis, and has clearly slipped on the F2 fault plane as is evident from the downward drag of the sediments. F2 shows a clear listric fault plane and, given the present (and extrapolated) curvature and the slipped F3 block on its surface, F2 would constitute a listric fault. However, given its position in the tectonically dominated segment to the north of AVR1, the fault will probably eventually rotate and move farther off-axis, just like F5. It is therefore likely, that the now listric planes of F2 and F3 will inverse and steepen if the amount of rotation is sufficient.

It is well documented that outward rotation of normal faults is a common feature at slow and ultraslow-spreading ridges (Cann et al., 2015; Dick et al., 2003; Laughton & Searle, 1979; Smith et al., 2006, 2008). Large amounts of such rotation, if resulting in an outward-facing ridge, are generally explained to be caused by flexural rotation, a process resulting in an overall steepening (convex-up) geometry (Buck, 1988; Lavier et al., 1999; Smith et al., 2008). The same should also apply to major rotated normal faults, such as F8, F7 and CHF. As they might be incipient or aborted detachment faults, they should be steepening rather than flattening at depth. This may be especially true if they show signs of basinal structures behind their fault ridges, an indicator that flexural rotation is or may have taken place, and thus no predominantly

listric faulting should be required to achieve the rotation (Buck, 1988). It is therefore possible that the large-scale block rotation at the Troodos Ophiolite, proposed by Verosub & Moores (1981) to be caused by listric faulting, could actually be the result of flexural rotation during extension.

The frequent sampling of peridotites and gabbros at spreading center, which Roberts et al. (1993) proposed could be explained by extension along listric normal faults during times of limited magma supply, is not entirely in accordance with generally accepted knowledge about oceanic detachment faults and exhumation of lower crustal and upper mantle lithologies (Lavier et al., 1999; Smith et al., 2008; Tucholke et al., 1998). They are indeed likely to be related to periods of limited magma supply as Roberts et al. (1993) have proposed (Buck et al., 2005; Schouten et al., 2010; Tucholke et al., 2008), but are uplifted by deep-seated and rotated detachment faults, instead of listric normal faults.

The last abundant structure on the ridge are the normal fault-bounded volcanic abyssal hills, formed by faulting and cutting of the AVRs in the center valley. They typically show steeper inward-facing scarps than outward-facing slopes and their geometries resemble that of the AVRs, as can be seen on the elevation profiles. They are also stacked in half graben arrangements where the scarp and slope differences, along with similar geometries and orientations as the concurrent AVRs, suggest that only minor rotation has taken place. This is easily seen on the seismic profiles, where mostly steeper fault scarps and shallower dipping outward-facing slopes define the structures on the eastern flank (Figure 6.13 and 6.14). As the abyssal hills in the north captured by the seismic profiles are morphologically comparable to the ones found on both flanks in the southern study area, it is reasonable to assume that the latter will display similar subsurface geometries as the former.

How faults eventually are terminated at depth is uncertain, but generally they are believed to either flatten out into a basal décollement or be simply terminated in the ductile rocks, which deform by ductile flow (Harper, 1985; Shelton, 1984). The presence of magma chambers beneath the ridge axis would raise the brittle-ductile transition (Harper, 1985), potentially favoring a curving of the faults at depth in accordance with the inferred strength contrasts resulting from it (Harper, 1985; Jackson & McKenzie, 1983). This could make low-angle and/or listric faulting possible in the upper few hundred meters of the crust (Karson & Rona, 1990). The information about the subsurface is limited, however, and derived conclusions about potential geometries and terminations at depths would therefore be largely speculative.

Based on the available data, there is no straightforward evidence that significant listric

faulting is occurring in the study area, as information about the depth is scarce or absent. Despite this, several faults around AVR1 captured by the seismic profiles show indications of varying curvature at depth. The combination of the likely presence of a magma chamber beneath the axis in this area, and the nature of faults at depth as proposed by Jackson & McKenzie (1983), leads to the conclusion that normal faults displaying curvature at depth may not be uncommon in the study area. Seeing how the normal faults on the eastern flank are tightly stacked and show varying degrees of curvature at depth, it is entirely possible that they may flatten into a common surface, possibly between layer 2 and 3 as proposed by Varga & Moores (1985), made possible by magma intrusions and a weaker crust (Karson & Rona, 1990). Without further subsurface data, however, this is entirely speculative. As such, based strictly on the meaning of the term *listric*, some faults in the study area can be described as faults with a listric geometry at depth, or *listric planes*; however, their continued nature at depth is uncertain.

7.3.3 Relevance for Hydrothermal Activity

Listric faulting has been connected to hydrothermal activity, leading to the question about the potential relationship. Karson & Rona (1990) identified a segment of listric faulting in the in the eastern valley walls of the TAG vent field, bordered by a segment of planar faulting. In the boundary zone between these two segments they identified east-west trending escarpments running perpendicular to the ridge axis and faults on the ridge flank. These escarpments were identified as transfer faults, and it is those which they proposed to be responsible for the primary facilitation of hydrothermal circulation (Karson & Rona, 1990). The reasoning behind this was that this transfer zone enables the two different styles of faulting to border each other, by allowing differential extension and rotation, resulting in increased permeability (Karson & Rona, 1990). As such, it is not the presence of listric faulting itself which is intrinsically responsible or connected to the hydrothermal activity, but rather the fact that two different types of faulting are bordering each other through a transfer fault. This makes transfer faults potentially attractive features to look for when exploring for hydrothermal activity in the axial valley, as has also been described by Baker & German (2004).

Similar faults are present on the Mohn's Ridge in the form of non-transform offsets (NTOs), resulting in the en-échelon pattern in the ridge valley, which is especially pronounced in the central parts of the ridge (Dauteuil & Brun, 1993). As seafloor spreading takes place roughly perpendicular to the en-échelon pattern (Géli, 1993), these faults have an orientation perpendicular to the AVRs and parallel to the spreading direction. Unfortunately, identifying strike-slip structures from bathymetric data is challenging. The transfer faults in the TAG area

described by Karson & Rona (1990) have scarp heights of typically < 20 m and are partially buried by rubble, meaning that bathymetry resolution is a major factor when analyzing for these structures. A discrete faulting zone was also not found on the surface, so it is mostly inferred based on mechanical requirements needed for the separation of the two fault segments (Karson & Rona, 1990) If, on the other hand, the strike-slip faults cut other structures, such as previously formed normal faults, then they can be inferred from the resulting displacement, given that the structures are not completely covered by sediments (Dauteuil, 1995). On the MR, however, NTOs are potentially relatively simple to identify as they mark the oblique offsets of the AVRs. This is relatively easy seen on the central MR, for instance around the two AVRs at Copper Hill (Figure 6.20), where the sinistral relationship between the two visible AVRs is caused by a non-transform offset. Still, in order to say something more concrete about the potential role played by transfer faulting on the MR, more research has to be conducted.

8. Methodological Considerations

8.1 Bathymetric Analysis

There are obvious limitations to the analysis of the seafloor bathymetry as performed in this study, the primary being the level detail and dimensions of structures that can be identified from it. In this study, the structures of interest were of the size of several kilometers and as such, the 100x100 m resolution of the bathymetric data is very appropriate. However, it also means that structures at the size of a few hundred meters will be very little detailed. Additionally, it is difficult to thoroughly identify lineations within the alley floor, as smaller-scale faulting (vertical offsets < 10 m) , or the 20 m high throws of the transfer fault zone at the TAG field would not be resolved on a 100 m grid (Escartín et al., 2017). This is also the reason why analysis of faulting within the axial valley was limited in this thesis.

8.2 Deriving Fault Angles from DTMs and Seismic Profiles

Fault and slope angles derived from DTMs should be used with caution, as there are several factors that can influence the accuracy of the values. For instance, a slope's gradient may be lowered if plotted on a coarse DTM grid by averaging areas that would otherwise be caught be a finer grid. An additional source of error is potential erosion of the fault scarp, which may deposit material from the scarp top as talus at the scarp base, smoothing the surfaces and effectively lowering the apparent slope values (Dauteuil, 1995; Sloan & Patriat, 2004). This is an important factor to consider when investigating smaller fault scarps, as most or all of the scarp could be covered by eroded material, effectively making the fault appear smaller than it actually is.

This factor is also apparent when comparing fault angles derived from the DTM with fault angles derived from the seismic profiles, where often discrepancies are present. The seismic data has the advantage that fault angles are not influenced by potential talus deposits or erosion of the slope. At this point it should be noted that the angles derived from the seismic profiles are calculated using an averaged seismic velocity for the complete sediment package, rather than adjusting the velocities for each package, as was done by Bruvoll et al. (2009). However, using velocities from 1700 – 2000 m/s only yielded a 2 – 3° difference, and the calculated values and thicknesses of the packages should therefore be sufficiently accurate.

8.3 3D-Modeling of Detachment Surfaces

One advantage of a 3D-model is the opening of new possibilities when it comes to visualization of the topography and being able to look at structures from different perspectives. The purpose behind the 3D modeling was purely based on interest in how such surfaces may look beneath the seafloor, an aspect much better handled by 3D-modelling than simple fault interpretation in 2D-cross-sections. Additionally, modelling structures in 3D gives the added advantage that creating cross-sections is a simple task because all visible features on the cross-sections will be evaluated from the modelled surfaces and will thus yield a much more coherent result. Another aspect is more freedom when placing profiles using 3D modelled features. Profiles can be placed anywhere and because the modelled surfaces are continuous, creating cross-sections is a simple task. In contrast, using 2D-discontinous profiles will create discontinuous cross-sections with no information of what lies between them.

Since the seismic events data were not sufficiently accurate to be used to infer fault planes below the seafloor, no depth information was available for the modelling of the 3D planes. The modelled fault planes are therefore purely conceptual, in order to convey an approximation of how these structures look in 3D-space. For the modelling procedure, the flexural model of Buck (1988) was very central, as it essentially provided the geometry of the finished models. Due to a lack of local and regional references, the dimensions of the TAG detachment fault (de Martin et al., 2007) (Figure 4.4) were used. A such, the rotated, shallow-dipping inactive part of the fault stretches for about 10 km before steepening to an approximate dip of 60°. The overall sizes of the core complexes on the surface are taken into account, so that the dimensions of the detachment faults may vary based on the size of the core complexes.

9. Conclusions

The Morphology of the northern Mohn's Ridge has been investigated and analyzed for structural elements and their relationship to SMS mineralizations. Digital terrain analysis of bathymetric data is a very powerful tool for the identification of surface features. The following conclusive points can be made from this study:

- The northern Mohn's Ridge has an asymmetrical morphology with large variations in topographic relief on the western flank and more regular relief on the eastern flank, caused by significant one-sided tectonic accommodation of extension.
- The western flank is characterized by several core complexes where lower crustal and mantle rocks have been exhumed. Multiple major rotated normal faults have been identified and are inferred to be incipient or aborted detachment faults. The eastern flank shows an overall even distribution of volcanic abyssal hills.
- The degree of magmatic influence during spreading has likely been greater in the southern parts compared to the northern parts. The ridge morphology is comparable to magmatic components of $M \approx 0.7$ and $M = 0.3 - 0.5$, respectively.
- The seismic event data was not sufficiently accurate to indicate smaller-scale areas of increased tectonic activity or to derived subsurface fault geometries.
- Normal faults that display a listric geometry at depth are probably common in the study area. How they are eventually terminated at depth, however, remains uncertain. F5, F3 and F2 are faults which could constitute a listric fault system, but without additional subsurface data this is speculative.
- Major rotated normal faults located in or near the valley walls and in close proximity to AVRs (e.g. F7 and F8) indicate a significant potential for channeling fluids and building ore deposits, and should therefore be taken into consideration in future exploration.
- Detachment faults in the study area are likely not active any longer, as they are all cut off from the axial valley by newer, rotated normal faults. However, because they once were located in the valley walls, it is likely that some of them may have channeled fluids. Deposits could therefore potentially be found on their surfaces or nearby.
- Non-Transfer faults are indicated as significant contributors to hydrothermal circulation, but it should be confirmed in further studies what role they may play as a prospecting tool.

10. Further work

To decrease uncertainty and help in the future of identification and exploration of seafloor-massive sulfide deposits on the Mohn's Ridge, more information and knowledge is required. Below follow a few ideas for further work regarding this topic:

- **Ocean bottom seismometers (OBS)** across a smaller area for higher-accuracy and lower magnitude measurements. Such data can be linked to changes in hydrothermal flow rates (Crone et al., 2010), magmatic diking source (Rundquist & Sobolev, 2002) and has been shown to be able to indicate active detachment faults beneath the surface (de Martin et al., 2007), because the fault will focus a large number of the seismicity in the area (Escartín et al., 2008). Further, links between hydrothermal activity and seismic activity has been inferred from studies involving arrays of OBS (Crone et al., 2010; Sohn et al., 1998).
- **High-resolution bathymetric data** will increase the detail and accuracy with which structures may be visualized. The MarMine 2016 cruise (Ludvigsen et al., 2016) has already begun its gathering of such data, with resolutions of down to 1x1, with varying results. The obvious limitations with such high resolutions is that significantly smaller areas are coverable, which is why smaller favorable areas have to be identified prior to acquisition of high-resolution bathometry. More detailed bathymetric data may also be helpful in resolving smaller-scale and NTO structures in the axial valley.
- **Geophysical investigations**, such as additional seismic profiles across areas of interest, e.g. major normal faults or core complexes. Magnetotelluric (MT) studies are able to measure subsurface electrical conductivity and have the ability to infer mineral deposits (Corseri et al., 2017). Such studies are currently being considered by the NTNU.

References

Allaby, M. (2013a). “listric fault.” In M. Allaby (Ed.), *A Dictionary of Geology and Earth Sciences* (4th ed., p. 343). Oxford, UK: “Oxford University Press.” https://doi.org/10.1093/acref/9780199653065.013.4812

Allaby, M. (2013b). Oceanic crust. In M. Allaby (Ed.), *A Dictionary of Geology and Earth Sciences* (4th ed., pp. 406–407). Oxford, UK: Oxford University Press.

Allen, P. A., & Allen, J. R. (2005a). Compositional Zonation of the Earth. In *Basin Analysis: Principles and Applications* (2nd ed., pp. 4–6). Blackwell Science Ltd.

Allen, P. A., & Allen, J. R. (2005b). The Physical State of the Lithosphere. In *Basin Analysis: Principles and Applications* (2nd ed., pp. 20–51). Blackwell Science Ltd.

Alletti, M., Baker, D. R., Scaillet, B., Aiuppa, A., Moretti, R., & Ottolini, L. (2009). Chlorine Partitioning Between a Basaltic Melt and H20-CO2 fluids at Mount Etna. *Chemical Geology*, *263*(1–4), 37–50. https://doi.org/<10.1016/j.chemgeo.2009.04.003

Anderson, E. M. (1905). The dynamics of faulting. *Transactions of the Edinburgh Geological Society*, *8*(3), 387–402. Retrieved from http://trned.lyellcollection.org/content/8/3/387.short

Arrell, K. E., Fisher, P. F., Tate, N. J., & Bastin, L. (2007). A fuzzy c-means classification of elevation derivatives to extract the morphometric classification of landforms in Snowdonia, Wales. *Computers and Geosciences*, *33*(10), 1366–1381. https://doi.org/10.1016/j.cageo.2007.05.005

Baker, E. T., & German, C. R. (2004). On the Global Distribution of Hydrothermal Vent Fields. In *Mid-Ocean Ridges* (pp. 245–266). American Geophysical Union. https://doi.org/10.1029/148GM10

Bally, A., Bernoulli, D., Davis, A., & Montadert, L. (1981). Listric normal faults. *Oceanologica Acta, Special Issue (0399-1784)*, 87–101.

Blackman, D. K., Cann, J. R., Janssen, B., & Smith, D. K. (1998). Origin of extensional core complexes: Evidence from the Mid-Atlantic Ridge at Atlantis Fracture Zone. *Journal of Geophysical Research: Solid Earth*, *103*(B9), 21315–21333. https://doi.org/10.1029/98JB01756

Bruvoll, V., Breivik, A. J., Mjelde, R., & Pedersen, R. B. (2009). Burial of the Mohn-Knipovich seafloor spreading ridge by the Bear Island Fan: Time constraints on tectonic evolution from seismic stratigraphy. *Tectonics*, *28*(4), 1–14. https://doi.org/10.1029/2008TC002396

Buck, R. W. (1988). Flexural Rotation of Normal Faults. *Tectonics*, *7*(5), 959–973. https://doi.org/10.1029/TC007i005p00959

Buck, R. W., Lavier, L. L., & Poliakov, A. N. B. (2005). Modes of faulting at mid-ocean ridges. *Nature*, *434*(7034), 719–723. Retrieved from http://dx.doi.org/10.1038/nature03358

Canales, J. P., Tucholke, B. E., & Collins, J. A. (2004). Seismic reflection imaging of an oceanic detachment fault: Atlantis megamullion (Mid-Atlantic Ridge, 30°10′N). *Earth and Planetary Science Letters*, *222*(2), 543–560. https://doi.org/http://dx.doi.org/10.1016/j.epsl.2004.02.023

Cann, J. R. (1997). Corrugated slip surfaces formed at ridge-transform intersections on the Mid-Atlantic Ridge. *Nature*, *385*, 329–332. https://doi.org/doi:10.1038/385329a0

Cann, J. R., Smith, D. K., Escartín, J., & Schouten, H. (2015). Tectonic evolution of 200 km of Mid-Atlantic Ridge over 10 million years: Interplay of volcanism and faulting. *Geochemistry, Geophysics, Geosystems*, *16*(7), 2303–2321. https://doi.org/10.1002/2015GC005797

Cannat, M., Sauter, D., Escartín, J., Lavier, L. L., & Picazo, S. (2009). Oceanic corrugated surfaces and the strength of the axial lithosphere at slow spreading ridges. *Earth and Planetary Science Letters*, *288*(1–2), 174–183. https://doi.org/http://dx.doi.org/10.1016/j.epsl.2009.09.020

Cherkashov, G. A., Andreev, S., Petukhov, S., Poroshina, I., & Zayonchek, A. (2013). *Identification of SMS prospective areas at the mid-ocean ridges within the Norwegian EEZ based on analysis of multibeam bathymetry data, Report to the NTNU*. Saint-Petersburg, RU.

Connelly, D. P., German, C. R., Asada, M., Okino, K., Egorov, A., Naganuma, T., … Tamaki, K. (2007). Hydrothermal activity on the ultra-slow spreading southern Knipovich Ridge. *Geochemistry, Geophysics, Geosystems*, *8*(8), n/a-n/a. https://doi.org/10.1029/2007GC001652

Corseri, R., Senger, K., Selway, K., Abdelmalak, M. M., Planke, S., & Jerram, D. A. (2017). Magnetotelluric evidence for massive sulphide mineralization in intruded sediments of the outer Vøring Basin, mid-Norway. *Tectonophysics*, *706–707*, 196–205. https://doi.org/https://doi.org/10.1016/j.tecto.2017.04.011

Crone, T. J., Wilcock, W. S. D., & McDuff, R. E. (2010). Flow rate perturbations in a black smoker hydrothermal vent in response to a mid-ocean ridge earthquake swarm. *Geochemistry, Geophysics, Geosystems*, *11*(3), n/a-n/a. https://doi.org/10.1029/2009GC002926

Dauteuil, O. (1995). Fault pattern from seabeam processing: The western part of the Blanco Fracture Zone (NE pacific). *Marine Geophysical Researches*, *17*(1), 17–35. https://doi.org/10.1007/BF01268049

Dauteuil, O., & Brun, J.-P. (1993). Oblique rifting in a slow-spreading ridge. *Nature*, *361*(6408), 145–148. Retrieved from http://dx.doi.org/10.1038/361145a0

Dauteuil, O., & Brun, J.-P. (1996). Deformation partitioning in a slow spreading ridge undergoing oblique extension: Mohns Ridge, Norwegian Sea. *Tectonics*, *15*(4), 870–884. https://doi.org/10.1029/95TC03682

de Martin, B. J., Reves-Sohn, R. A., Canales, J. P., & Humphris, S. E. (2007). Kinematics and geometry of active detachment faulting beneath the Trans-Atlantic geotraverse (TAG) hydrothermal field on the Mid-Atlantic Ridge. *Geology*, *35*(8), 711–714. https://doi.org/10.1130/G23718A.1

Dick, H. J. B., Lin, J., & Schouten, H. (2003). An ultraslow-spreading class of ocean ridge. *Nature*, *426*(6965), 405–412. https://doi.org/10.1038/nature02128

Dubinin, E. P., Kokhan, A. V., & Sushchevskaya, N. M. (2013). Tectonics and magmatism of ultraslow spreading ridges. *Geotectonics*, *47*(3), 131–155. https://doi.org/10.1134/S0016852113030023

Ellefmo, S. L., Sinding-Larsen, R., & Søreide, F. X. (2014). Marine Minerals and Oceans Mining Potentail in the North Atlantic. In *The 43rd Conference of the Underwater Mining Institute, September 21-28, 2014, Lisbon, Portugal*.

Escartín, J., Mével, C., Petersen, S., & Garcia, R. (2017). Tectonic structure, evolution, and the nature of oceanic core complexes and their detachment fault zones (13°20'N and 13°30'N, Mid Atlantic Ridge). *Geochemistry, Geophysics, Geosystems, In Press*. https://doi.org/10.1002/2016GC006775

Escartín, J., Smith, D. K., Cann, J. R., Schouten, H., Langmuir, C. H., & Escrig, S. (2008). Central role of detachment faults in accretion of slow-spreading oceanic lithosphere. *Nature*, *455*(October), 790–794. https://doi.org/10.1038/nature07333

ESRI. (2016). ArcGIS Desktop Help 10.4, Raster Functions. Retrieved November 8, 2016, from http://desktop.arcgis.com/en/arcmap/latest/manage-data/raster-and-images/apparent-reflectance-function.htm

Evans, I. S. (2005). General geomorphometry. In A. Goudie (Ed.), *Geomorphological Techniques* (2nd ed., pp. 49–62). New York, USA: Taylor & Francis e-Library. https://doi.org/10.4324/9780203430590

Florinsky, I. V. (1996). Quantitative topographic method of fault morphology recognition. *Geomorphology*, *16*(2), 103–119. https://doi.org/10.1016/0169-555X(95)00136-S

Florinsky, I. V. (2012). *Digital Terrain Analysis in Soil Science and Geology* (1st ed.). Kidlington, Oxford, UK: Academic Press, Elsevier.

Francheteau, J., Needham, H. D., Choukroune, P., Juteau, T., Seguret, M., Ballard, R. D., … Hekinian, R. (1979). Massive deep-sea sulphide ore deposits discovered on the East Pacific Rise. *Nature*, *277*(5697), 523–528. Retrieved from http://archimer.ifremer.fr/doc/00000/5278/

Früh-Green, G. L. (2005). The Lost City 2005 Expedition: Serpentinization. Retrieved April 13, 2017, from http://oceanexplorer.noaa.gov/explorations/05lostcity/background/serp/serpentinization.html

Galley, A. G., Hannington, M. D., & Jonasson, I. R. (2007). Volcanogenic Massive Sulfide Deposits. *Mineral Deposits of Canada: A Synthesis of Major Deposit-Types, District Metallogeny, the Evolution of Geological Provinces, and Exploration Methods*, (5), 141–161. https://doi.org/10.1016/0169-1368(95)00022-4

Géli, L. (1993). Volcano-tectonic event and sedimentation since Late Miocene times at the Mohn's Ridge near 72° in the Greenland-Greenland Sea. *Tectonophysics*, *222*, 417–444.

German, C. R., Petersen, S., & Hannington, M. D. (2016). Hydrothermal exploration of mid-ocean ridges: Where might the largest sulfide deposits be forming? *Chemical Geology*, *420*(January), 114–126. https://doi.org/10.1016/j.chemgeo.2015.11.006

Goff, J. A., Tucholke, B. E., Lin, J., Jaroslow, G. E., & Kleinrock, M. C. (1995). Quantitative analysis of abyssal hills in the Atlantic Ocean: A correlation between inferred crustal thickness and extensional faulting. *Journal of Geophysical Research: Solid Earth*, *100*(B11), 22509–22522.

https://doi.org/10.1029/95JB02510

Grandell, L., Lehtilä, A., Kivinen, M., Koljonen, T., Kihlman, S., & Lauri, L. S. (2016). Role of critical metals in the future markets of clean energy technologies. *Renewable Energy*, *95*, 53–62. https://doi.org/http://doi.org/10.1016/j.renene.2016.03.102

Hannington, M. D., De Ronde, C. E. J., & Petersen, S. (2005). Sea-floor tectonics and submarine hydrothermal systems. (F. A. O. of the UN, Ed.). Retrieved from http://oceanrep.geomar.de/6271/1/EN_1162_Hannington et al_2005_Econ Geol 100th.pdf

Hannington, M. D., Jamieson, J., Monecke, T., Petersen, S., & Beaulieu, S. (2011). The abundance of seafloor massive sulfide deposits. *Geology*, *39*(12), 1155–1158. Retrieved from http://geology.gsapubs.org/content/39/12/1155.abstract

Hannington, M. D., Jamieson, J., & Petersen, S. (2015). Seafloor massive sulfide deposits: Continuing efforts toward a global estimate of seafloor massive sulfides. *OCEANS 2015 - Genova*. https://doi.org/10.1109/OCEANS-Genova.2015.7271526

Harper, G. D. (1985). Tectonics of Slow Spreading Mid-Ocean Ridges and Consequences of a Variable Depth To the Brittle/Ductile Transition. *Tectonics*, *4*(4), 395–409. https://doi.org/10.1029/TC004i004p00395

Heywood, I., Cornelius, S., & Carver, S. (2006). *An Introduction To Geographical Information Systems* (3rd ed.). Harlow, Essex: Pearson Education Limited.

Hirt, C. (2014). Digital Terrain Models BT - Encyclopedia of Geodesy. In E. Grafarend (Ed.) (pp. 1–6). Cham: Springer International Publishing. https://doi.org/10.1007/978-3-319-02370-0_31-1

Humphris, S. E., Herzig, P. M., Miller, D. J., Alt, J. C., Becker, K., Brown, D., … Zhao, X. (1995). The internal structure of an active sea-floor massive sulfide deposit. *Nature*. https://doi.org/10.1038/377713a0

Humphris, S. E., & Tivey, M. K. (2000). A synthesis of geological and geochemical investigations of the TAG hydrothermal field: Insights into fluid-flow and mixing processes in a hydrothermal system. *Geological Society of America Special Papers* , *349*, 213–235. Retrieved from http://specialpapers.gsapubs.org/content/349/213.abstract

Humphris, S. E., Tivey, M. K., & Tivey, M. A. (2015). The Trans-Atlantic Geotraverse hydrothermal field: A hydrothermal system on an active detachment fault. *Deep Sea Research Part II: Topical Studies in Oceanography*, *121*, 8–16. https://doi.org/http://dx.doi.org/10.1016/j.dsr2.2015.02.015

Jackson, J., & McKenzie, D. (1983). The geometrical evolution of normal fault systems. *Journal of Structural Geology*, *5*(5), 471–482. https://doi.org/http://dx.doi.org/10.1016/0191-8141(83)90053-6

Karson, J. A., & Rona, P. A. (1990). Block-tilting, transfer faults, and structural control of magmatic and hydrothermal processes in the TAG area, Mid-Atlantic Ridge 26??N. *Geological Society of America Bulletin*, *102*(12), 1635–1645. https://doi.org/10.1130/0016-7606(1990)102<1635:BTTFAS>2.3.CO;2

Klingelhöfer, F., Géli, L., Matias, L., Steinsland, N., & Mohr, J. (2000). Crustal structure of a super-slow spreading centre: A seismic refraction study of Mohns Ridge, 72°N. *Geophysical Journal International*, *141*(2), 509–526. https://doi.org/10.1046/j.1365-246X.2000.00098.x

Laughton, A., & Searle, R. C. (1979). Tectonic Processes on Slow Spreading Ridges. In M. Talwani, C. G. Harrison, & D. E. Hayes (Eds.), *Deep Drilling Results in the Atlantic Ocean: Ocean Crust* (pp. 15–32). American Geophysical Union. https://doi.org/10.1029/ME002p0015

Lavier, L. L., Buck, R. W., & Poliakov, A. N. B. (1999). Self-consistent rolling-hinge model for the evolution of large- offset low-angle normal faults. *Geology*, *27*(12), 1127–1130. https://doi.org/10.1130/0091-7613(1999)027<1127

Ludvigsen, M., Søreide, F. X., Aasly, K., Ellefmo, S. L., Zylstra, M., & Pardey, M. (2017). ROV based drilling for deep sea mining exploration - Submitted to. In *OCEANS 2017, Aberdeen*.

Ludvigsen, M., Aasly, K., Ellefmo, S. L., Hilário, A., Ramirez, E. L., Søreide, F. X., … Sture, Ø. (2016). *Marmine Cruise Report Arctic Mid-Ocean Ridge 15.08.2016 - 05.09.2016, NTNU, Norway*. Retrieved from https://brage.bibsys.no/xmlui/handle/11250/2427715

Macdonald, K. C. (2001). *Mid-Ocean Ridge Tectonics, Volcanism, and Geomorphology*. *Encyclopedia of Ocean Sciences* (1st ed., Vol. 3). Elsevier Ltd. https://doi.org/10.1016/B978-012374473-9.00094-1

Mallast, U., Gloaguen, R., Geyer, S., Rödiger, T., & Siebert, C. (2011). Derivation of groundwater flow-

paths based on semi-automatic extraction of lineaments from remote sensing data. *Hydrol. Earth Syst. Sci.*, *15*(8), 2665–2678. https://doi.org/10.5194/hess-15-2665-2011

McCaig, A. M., Cliff, R. A., Escartín, J., Fallick, A. E., & MacLeod, C. J. (2007). Oceanic detachment faults focus very large volumes of black smoker fluids. *Geology*, *35*(10), 935 LP-938. Retrieved from http://geology.gsapubs.org/content/35/10/935.abstract

Mutter, J. C., & Karson, J. A. (1992). Structural Processes at Slow-Spreading Ridges. *Science*, *257*(5070), 627 LP-634. https://doi.org/10.1126/science.257.5070.627

NORSAR. (n.d.). NORSAR Reviewd Regional Seismic Bulletin. Retrieved from http://www.norsardata.no/NDC/bulletins/regional/

Okino, K., Matsuda, K., Christie, D. M., Nogi, Y., & Koizumi, K. (2004). Development of oceanic detachment and asymmetric spreading at the Australian-Antarctic Discordance. *Geochemistry, Geophysics, Geosystems*, *5*(12), n/a-n/a. https://doi.org/10.1029/2004GC000793

Olsen, B. R., Økland, I. E., Thorseth, I. H., Pedersen, R. B., & Rapp, H. T. (2016). *Environmental challenges related to offshore mining and gas hydrate extraction*. Retrieved from http://www.miljodirektoratet.no/no/Publikasjoner/2016/April-2016/Environmental-challenges-related-to-offshore-mining-and-gas-hydrate-extraction/

Onorati, G., Ventura, R., Poscolieri, M., Chiarini, V., & Crucillà, U. (1992). The Digital Elevation Model of Italy for geomorphology and structural geology. *Catena*, *19*(2), 147–178. https://doi.org/10.1016/0341-8162(92)90022-4

Pedersen, R. B., & Bjerkgård, T. (2016). Seafloor Massive Sulphides In Arctic Waters. In B. Rognvald, T. Bjerkgård, B. Nordahl, & H. Schiellerup (Eds.), *Mineral Resources In The Arctic* (1st ed., pp. 209–216). Geological Survey Of Norway.

Pedersen, R. B., Rapp, H. T., Thorseth, I. H., Lilley, M. D., Barriga, F. J. a S., Baumberger, T., … Jorgensen, S. L. (2010). Discovery of a black smoker vent field and vent fauna at the Arctic Mid-Ocean Ridge. *Nature Communications*, *1*(May), 126. https://doi.org/10.1038/ncomms1124

Pedersen, R. B., Thorseth, I. H., Hellevang, B., Schultz, A., Taylor, P., Knudsen, H. P., & Steinsbu, B. O. (2005). Two vent felds discovered at the ultraslow spreading Arctic Ridge System. *EOS Transactions, American Geophysical Union, Fall Meet. Suppl., Abstract OS21C-01*, *86*(52).

Pedersen, R. B., Thorseth, I. H., Nygård, T. E., Lilley, M. D., & Kelley, D. S. (2013). Hydrothermal Activity at the Arctic Mid-Ocean Ridges. *Diversity of Hydrothermal Systems on Slow Spreading Ocean Ridges*, 67–89. https://doi.org/10.1029/2008GM000783

Pedersen, R. B., Thorseth, I. H., Olson, E. J., Hellevang, H., Okland, I., Baumberger, T., … Haflidason, H. (2007). Hydrothermal activity and core complex formation at the Arctic Mid?Ocean Ridge: An overview of preliminary results of the H2DEEP expedition to the southern Knipovich Ridge at 73N. *Amercian Geophysical Union, Fall Meeting 2007, Abstract #OS41C-05*, 5–7.

Petersen, S., Krätschell, A., Augustin, N., Jamieson, J., Hein, J. R., & Hannington, M. D. (2016). News from the seabed – Geological characteristics and resource potential of deep-sea mineral resources. *Marine Policy*, *70*, 1–13. https://doi.org/10.1016/j.marpol.2016.03.012

Petersen, S., Kuhn, K., Kuhn, T., Augustin, N., Hékinian, R., Franz, L., & Borowski, C. (2009). The geological setting of the ultramafic-hosted Logatchev hydrothermal field (14°45′N, Mid-Atlantic Ridge) and its influence on massive sulfide formation. *Lithos*, *112*(1–2), 40–56. https://doi.org/http://dx.doi.org/10.1016/j.lithos.2009.02.008

Pike, R. J. (2002). *A Bibliography of Terrain Modeling (Geomorphometry), the Quantitative Representation of Topography*.

Podobnikar, T. (2005). Production of integrated digital terrain model from multiple datasets of different quality. *International Journal of Geographical Information Science*, *19*(1), 69–89. https://doi.org/10.1080/13658810412331280130

Robb, L. (2005). *Introduction to Ore-Forming Processes* (1st ed.). Oxford: Blackwell Science Ltd.

Roberts, S., Andrews, J. R., Bull, J. M., & Sanderson, D. J. (1993). Slow-spreading ridge-axis tectonics: evidence from the Lizard complex, UK. *Earth and Planetary Science Letters*, *116*(1–4), 101–112. https://doi.org/10.1016/0012-821X(93)90047-D

Rundquist, D. V., & Sobolev, P. O. (2002). Seismicity of mid-oceanic ridges and its geodynamic implications: A review. *Earth-Science Reviews*, *58*(1–2), 143–161. https://doi.org/10.1016/S0012-8252(01)00086-1

Schouten, H., Smith, D. K., Cann, J. R., & Escartín, J. (2010). Tectonic versus magmatic extension in

the presence of core complexes at slow-spreading ridges from a visualization of faulted seafloor topography. *Geology*, *38*(7), 615–618. Retrieved from http://geology.gsapubs.org/content/38/7/615.abstract

Searle, R. C., Murton, B. J., Achenbach, K., LeBas, T., Tivey, M. K., Yeo, I., … Waters, C. (2010). Structure and development of an axial volcanic ridge: Mid-Atlantic Ridge, 45°N. *Earth and Planetary Science Letters*, *299*(1–2), 228–241. https://doi.org/http://dx.doi.org/10.1016/j.epsl.2010.09.003

Shaw, P. R., & Lin, J. (1993). Causes and consequences of variations in faulting style at the Mid-Atlantic Ridge. *Journal of Geophysical Research: Solid Earth*, *98*(B12), 21839–21851. https://doi.org/10.1029/93JB01565

Shelton, J. W. (1984). Listric Normal Faults: an Illustrated Summary. *American Association of Petroleum Geologists Bulletin*, *68*(7), 801–815. https://doi.org/10.1306/AD461426-16F7-11D7-8645000102C1865D

Sloan, H., & Patriat, P. (2004). Generation of morphotectonic fabric on the Mid-Atlantic Ridge flanks, 28° to 29°N: Implications for the limits of tectonic deformation and abyssal hill formation. *Geochemistry, Geophysics, Geosystems*, *5*(2), n/a-n/a. https://doi.org/10.1029/2003GC000584

Smith, D. K., Cann, J. R., & Escartín, J. (2006). Widespread active detachment faulting and core complex formation near 13 degrees N on the Mid-Atlantic Ridge. *Nature*, *442*(7101), 440–3. https://doi.org/10.1038/nature04950

Smith, D. K., Escartín, J., Schouten, H., & Cann, J. R. (2008). Fault rotation and core complex formation: Significant processes in seafloor formation at slow-spreading mid-ocean ridges (Mid-Atlantic Ridge, 13°–15°N). *Geochemistry, Geophysics, Geosystems*, *9*(3), n/a-n/a. https://doi.org/10.1029/2007GC001699

Smith, D. K., Humphris, S. E., Tivey, M. A., & Cann, J. R. (1997). Viewing the morphology of the Mid Atlantic Ridge from a new perspective. *EOS Transactions, American Geophysical Union*, *78*(26), 256. Retrieved from file://localhost/Users/jescartin/WORK/Referencias/pdfs/Smith1997.pdf

Sohn, R. A., Fornari, D. J., Von Damm, K. L., Hildebrand, J. A., & Webb, S. C. (1998). Seismic and hydrothermal evidence for a cracking event on the East Pacific Rise crest at 9[deg][thinsp]50[prime][thinsp]N. *Nature*, *396*(6707), 159–161. Retrieved from http://dx.doi.org/10.1038/24146

Spencer, J. E. (1999). Geologic continuous casting below continental and deep-sea detachment faults and at the striated extrusion of Sacsayhuamán, Peru. *Geology*, *27*(4), 327–330. Retrieved from http://geology.gsapubs.org/content/27/4/327.abstract

Suess, E. (1909). *The Face of the Earth: Das Antlitz der Erde, Vol.4*. Oxford, UK: Clarendon Press.

Talwani, M., & Eldholm, O. (1977). Evolution of the Norwegian-Greenland Sea. *Geological Society of America Bulletin*, *88*(7), 969 LP-999. Retrieved from http://gsabulletin.gsapubs.org/content/88/7/969.abstract

Talwani, M., Windisch, C. C., & Langseth, M. G. (1971). Reykjanes ridge crest: A detailed geophysical study. *Journal of Geophysical Research*, *76*(2), 473–517. https://doi.org/10.1029/JB076i002p00473

Tivey, M. K. (2007). Generation of Seafloor Hydrothermal Vent Fluids and Associated Mineral Deposits. *Oceanography*, *20*. Retrieved from http://dx.doi.org/10.5670/oceanog.2007.80

Tucholke, B. E., Behn, M. D., Buck, R. W., & Lin, J. (2008). Role of melt supply in oceanic detachment faulting and formation of megamullions. *Geology*, *36*(6), 455–458. https://doi.org/10.1130/G24639A.1

Tucholke, B. E., & Lin, J. (1994). A geological model for the structure of ridge segments in slow spreading ocean crust. *Journal of Geophysical Research: Solid Earth*, *99*(B6), 11937–11958. https://doi.org/10.1029/94JB00338

Tucholke, B. E., Lin, J., & Kleinrock, M. C. (1998). Megamullions and mullion structure defining oceanic metamorphic core complexes on the Mid-Atlantic Ridge. *Journal of Geophysical Research: Solid Earth*, *103*(B5), 9857–9866. https://doi.org/10.1029/98JB00167

Varga, R. J., & Moores, E. M. (1985). Spreading structure of the Troodos ophiolite, Cyprus. *Geology*, *13*(12), 846–850. https://doi.org/10.1130/0091-7613(1985)13<846:SSOTTO>2.0.CO;2

Verosub, K. L., & Moores, E. M. (1981). Tectonic rotations in extensional regimes and their paleomagnetic consequences for oceanic basalts. *Journal of Geophysical Research: Solid Earth*,

86(B7), 6335–6349. https://doi.org/10.1029/JB086iB07p06335

Wernicke, B., & Burchfiel, B. C. (1982). Modes of extensional tectonics. *Journal of Structural Geology*, *4*(2), 105–115. https://doi.org/http://dx.doi.org/10.1016/0191-8141(82)90021-9

White, R. S., Bown, J. W., & Smallwood, J. R. (1995). The temperature of the Iceland plume and origin of outward-propagating V-shaped ridges. *Journal of the Geological Society*, *152*(6), 1039–1045. https://doi.org/10.1144/GSL.JGS.1995.152.01.26

White, R. S., McKenzie, D., & O'Nions, R. K. (1992). Oceanic crustal thickness from seismic measurements and rare earth element inversions. *Journal of Geophysical Research*, *97*(B13), 19683–19715. https://doi.org/10.1029/92JB01749

Whitney, D. L., Teyssier, C., Rey, P., & Buck, R. W. (2013). Continental and oceanic core complexes. *Bulletin of the Geological Society of America*, *125*(3–4), 273–298. https://doi.org/10.1130/B30754.1

Appendix A: Elevation Profiles

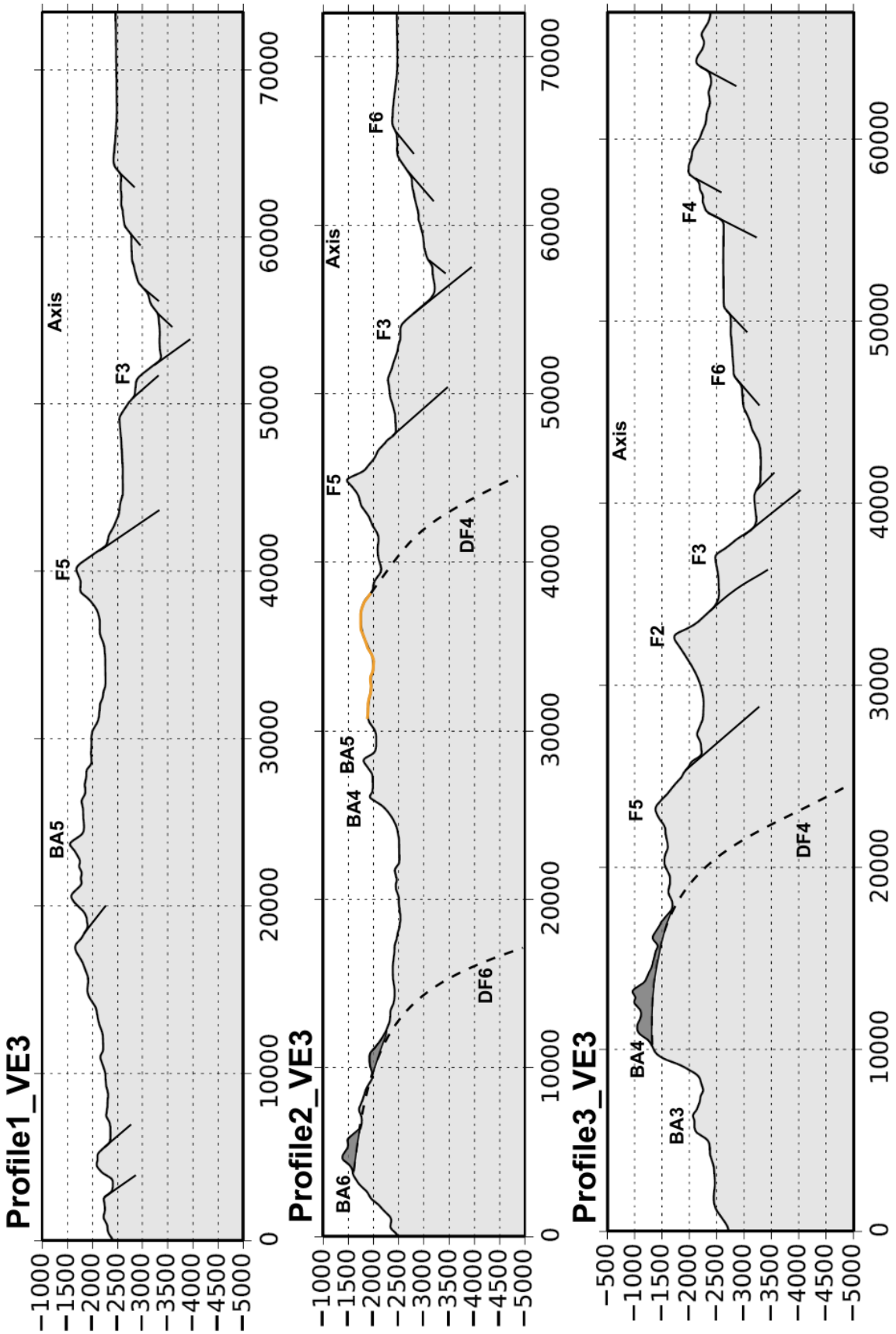

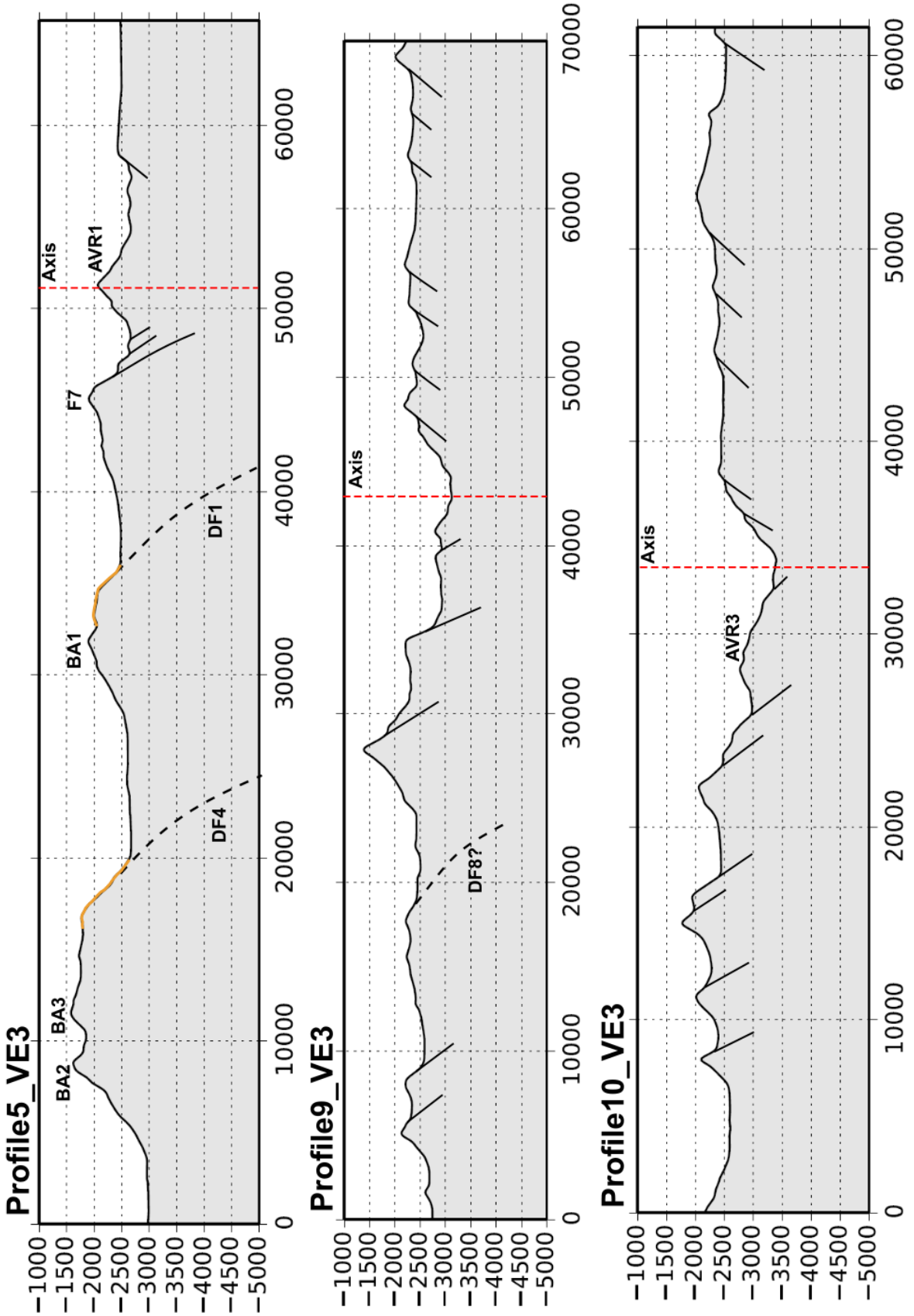
Profile5_VE3
Axis
AVR1
F7
DF1
BA1
DF4
BA3
BA2
Profile9_VE3
Axis
DF8?
Profile10_VE3
Axis
AVR3

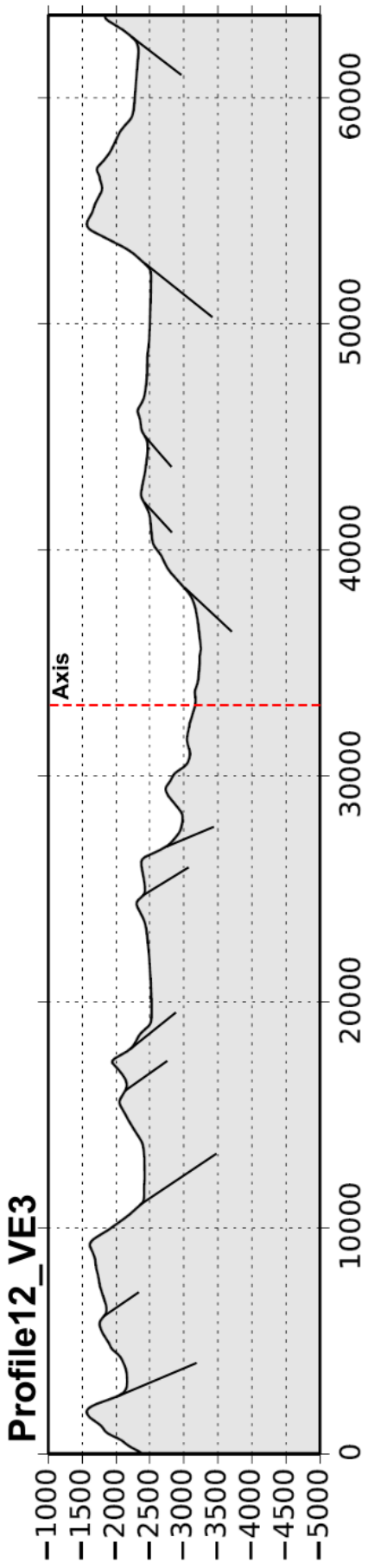
Profile12_VE3
Axis
0
10000
20000
30000
40000
50000
60000
−1000
−1500
−2000
−2500
−3000
−3500
−4000
−4500
−5000

Appendix B: 3D-Model Profiles

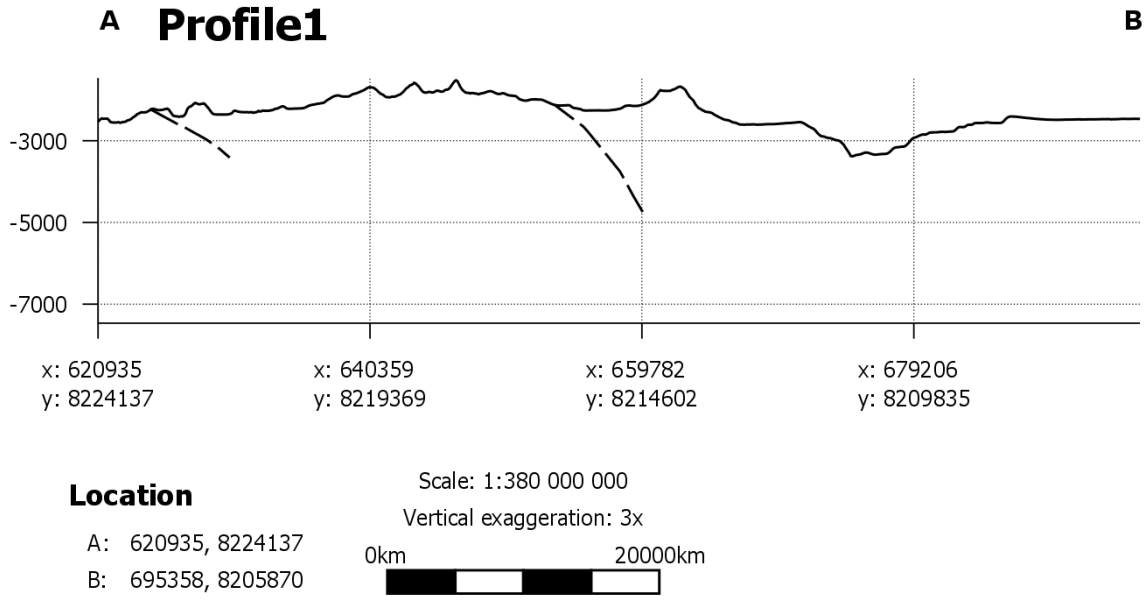

Location

A: 620935, 8224137
B: 695358, 8205870

Scale: 1:380 000 000
Vertical exaggeration: 3x
0km 20000km

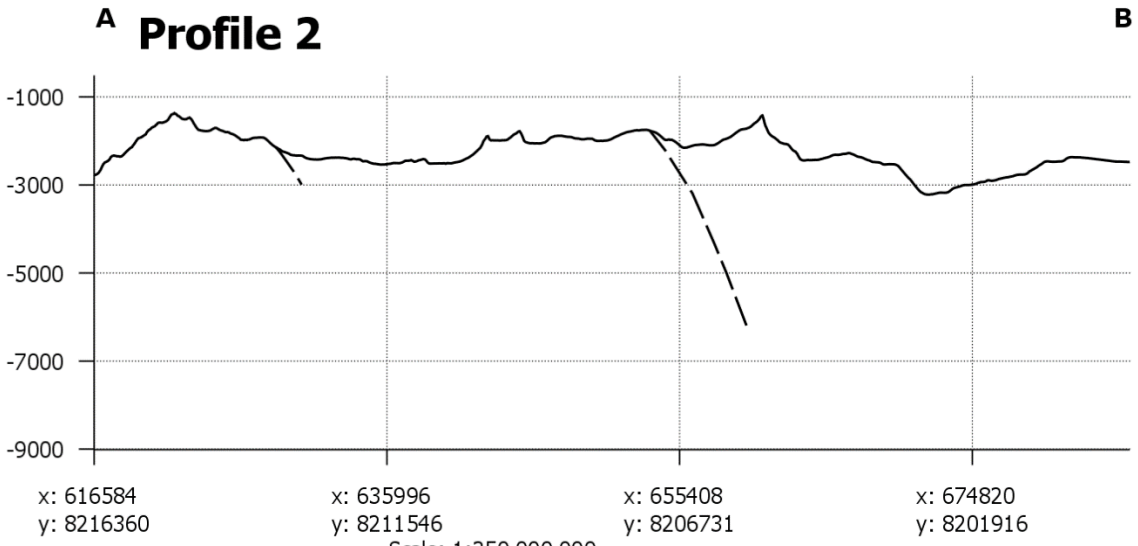

Location

A: 616584, 8216360
B: 685262, 8199326

Scale: 1:350 000 000
Vertical exaggeration: 3x
0km 20000km

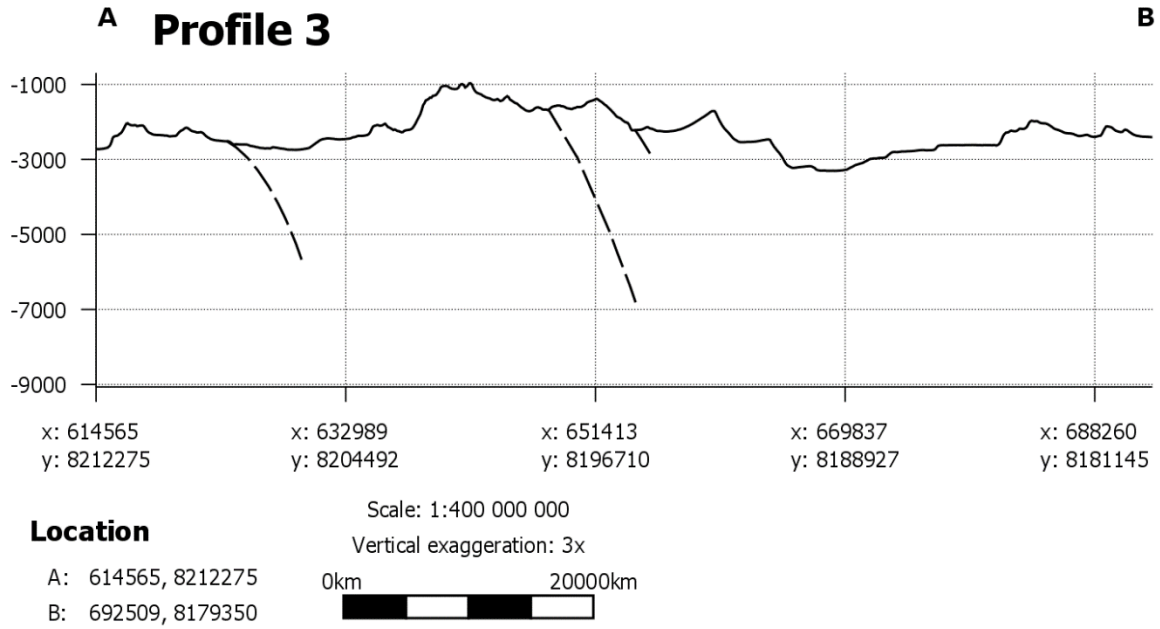
A
Profile 3
B
-1000
-3000
-5000
-7000
-9000
x: 614565
y: 8212275
x: 632989
y: 8204492
x: 651413
y: 8196710
x: 669837
y: 8188927
x: 688260
y: 8181145
Location
A: 614565, 8212275
B: 692509, 8179350
Scale: 1:400 000 000
Vertical exaggeration: 3x
0km
20000km

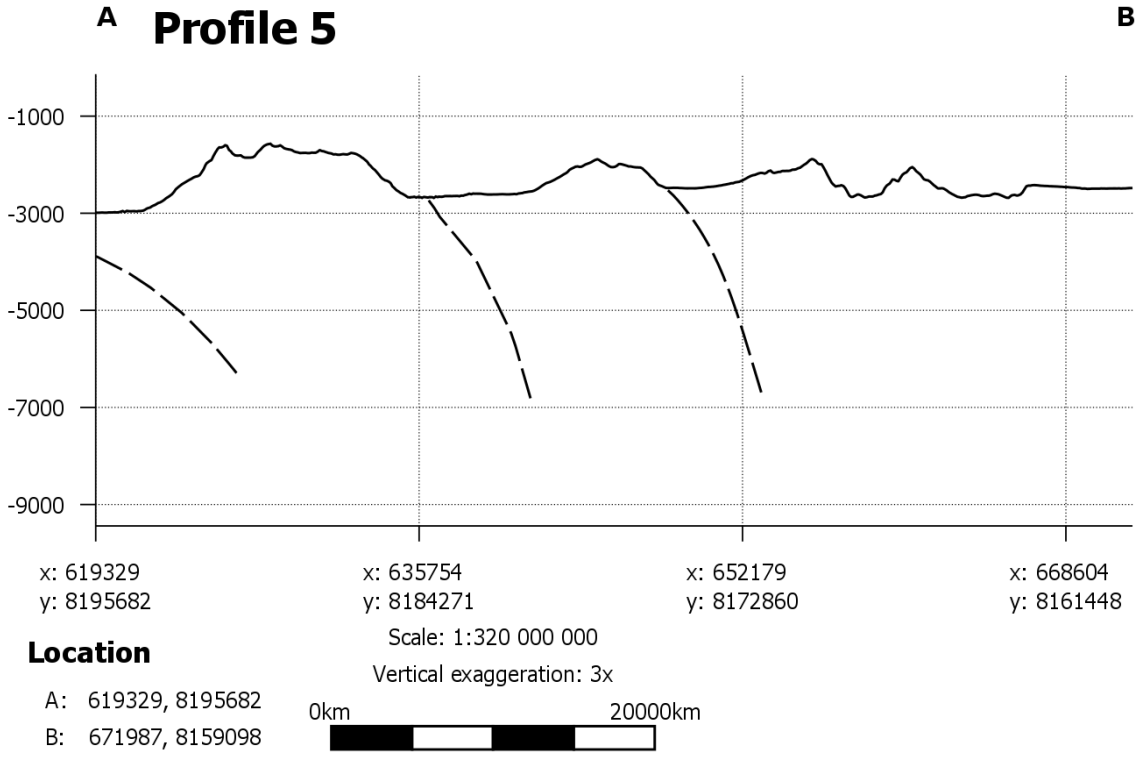
A
Profile 5
B
-1000
-3000
-5000
-7000
-9000
x: 619329
y: 8195682
x: 635754
y: 8184271
x: 652179
y: 8172860
x: 668604
y: 8161448
Location
A: 619329, 8195682
B: 671987, 8159098
Scale: 1:320 000 000
Vertical exaggeration: 3x
0km
20000km

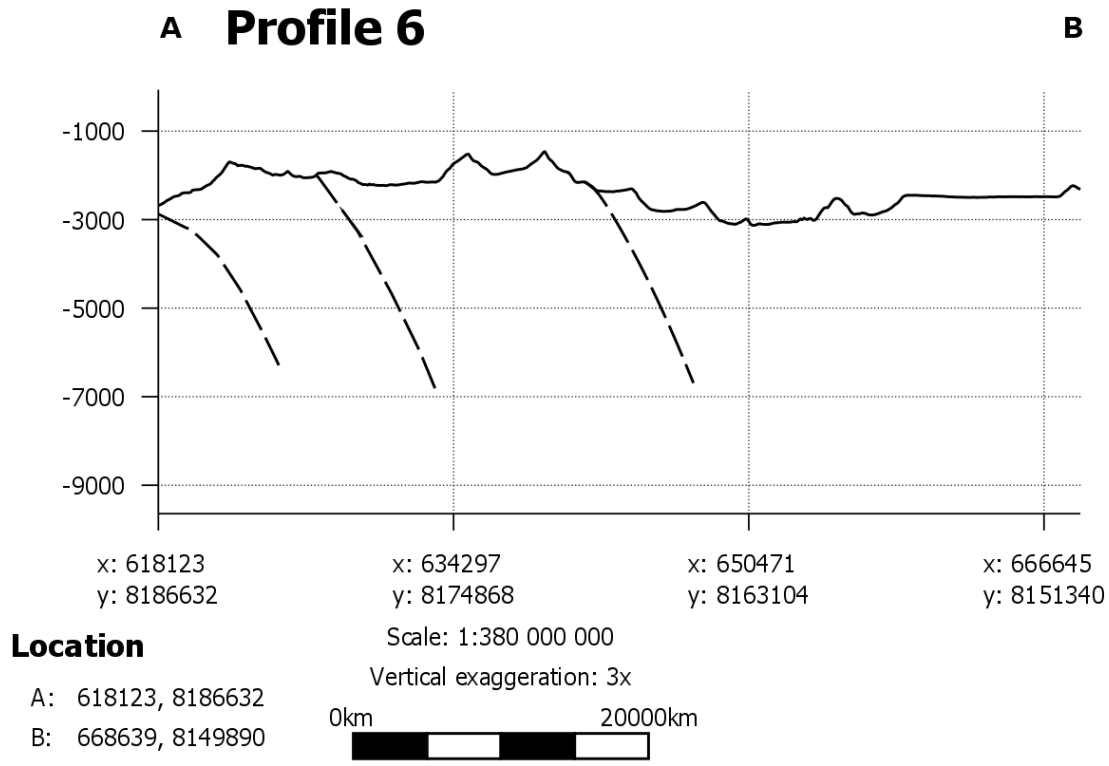
A
Profile 6
B
-1000
-3000
-5000
-7000
-9000
x: 618123
y: 8186632
x: 634297
y: 8174868
x: 650471
y: 8163104
x: 666645
y: 8151340
Location
A: 618123, 8186632
B: 668639, 8149890
Scale: 1:380 000 000
Vertical exaggeration: 3x
0km
20000km

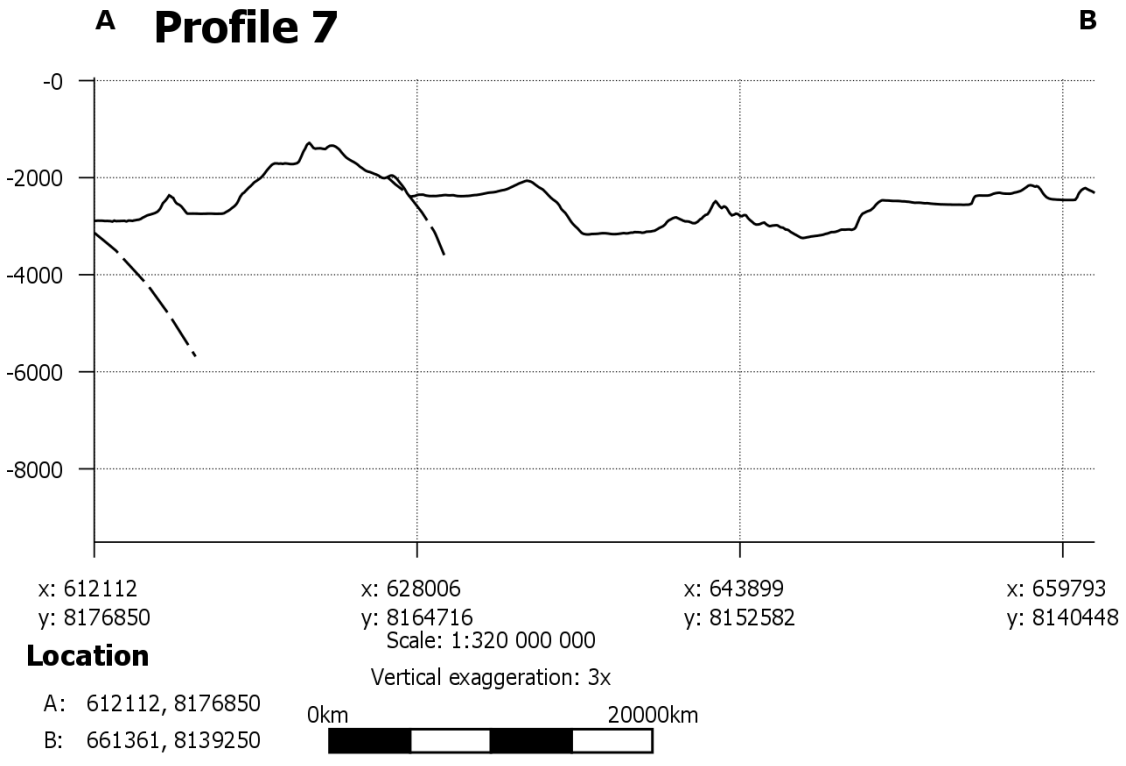
A
Profile 7
B
-0
-2000
-4000
-6000
-8000
x: 612112
y: 8176850
x: 628006
y: 8164716
x: 643899
y: 8152582
x: 659793
y: 8140448
Location
A: 612112, 8176850
B: 661361, 8139250
Scale: 1:320 000 000
Vertical exaggeration: 3x
0km
20000km

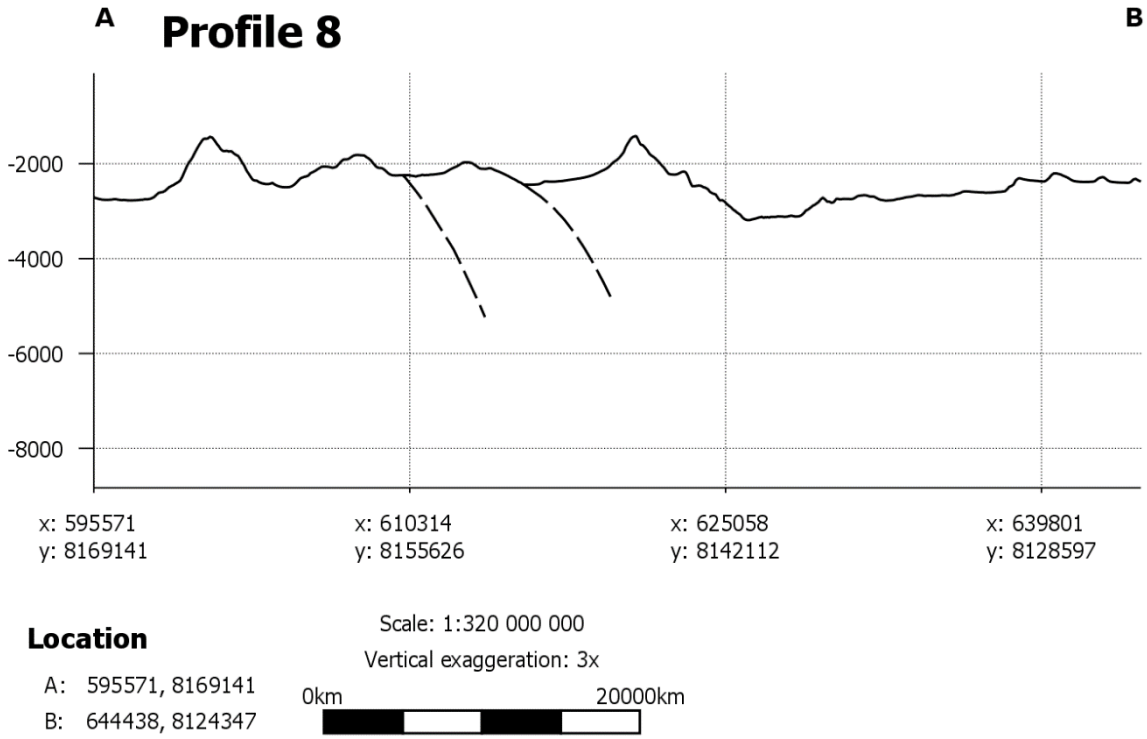

Location

A: 595571, 8169141
B: 644438, 8124347

Scale: 1:320 000 000
Vertical exaggeration: 3x
0km 20000km

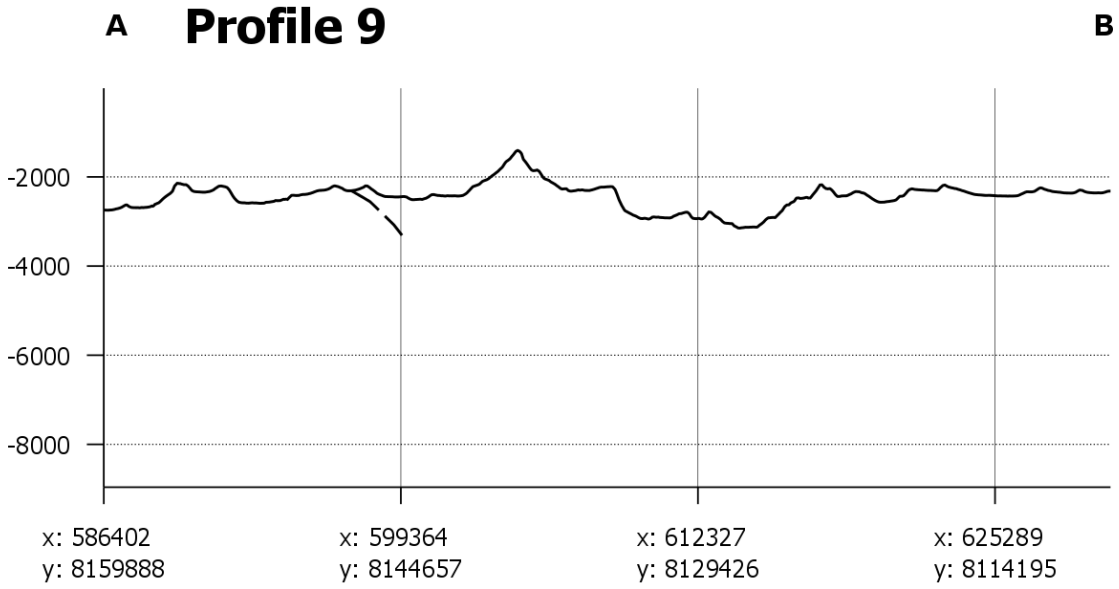

Location

A: 586402, 8159888
B: 630327, 8108276

Scale: 1:380 000 000
Vertical exaggeration: 3x
0km 20000km

Appendix D: DTM Processing

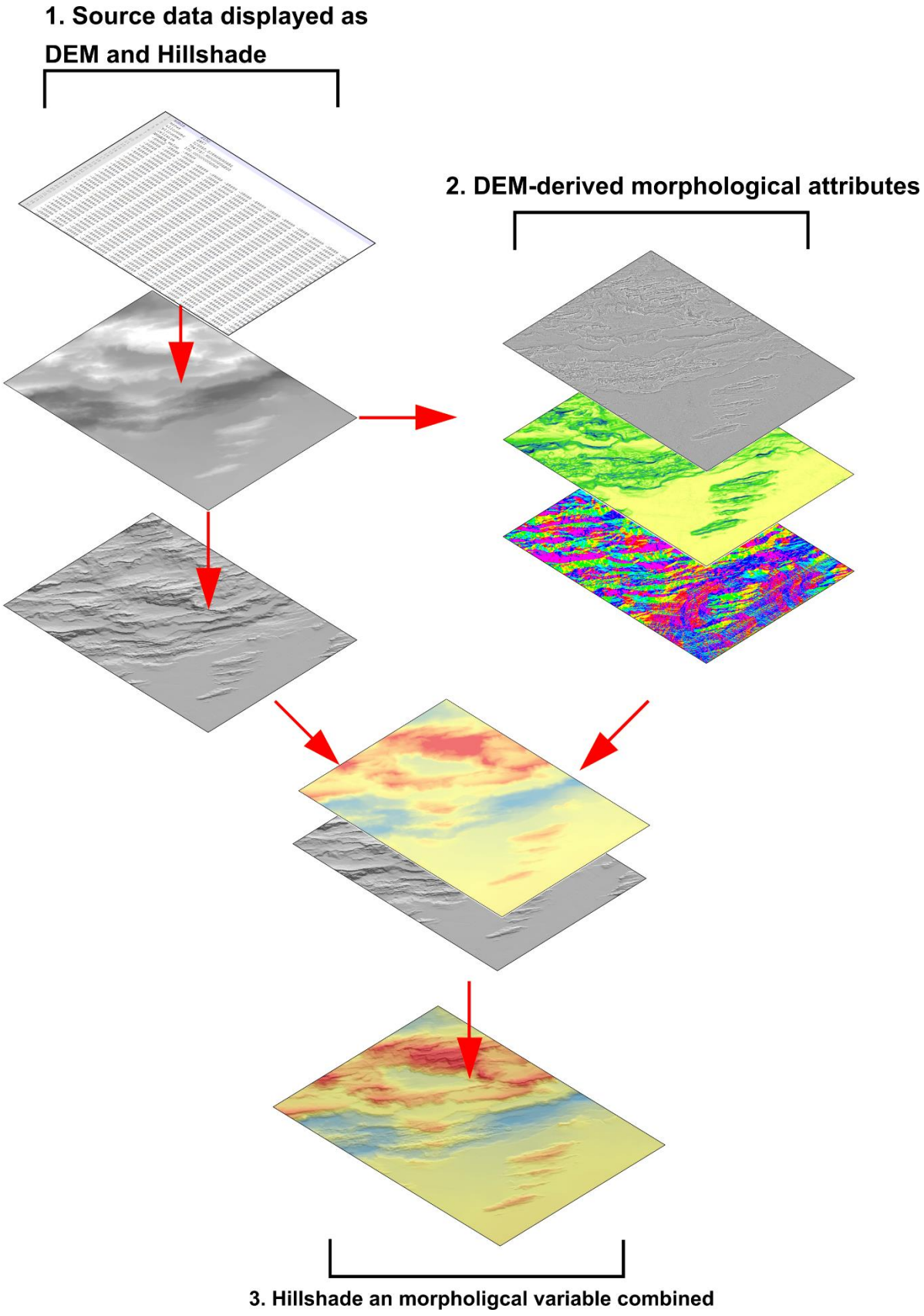

Appendix C: Python Code

```
1. #   Import the Pyproj coordinate transformation and the CSV
2. package
3. import pyproj
4. import csv
5.
6. #   Opens an existing delimited text file containing the
7. coordinates to be transformed, as well as creating a new
8. output file where the transformed coordinates will be stored.
9. with open(r'C:\Users\Hauke\Desktop\coord.txt', 'r') as csvInput:

10.     with open(r'C:\Users\Hauke\Desktop\coordOut.txt', 'w')as csvO
    utput:
11.         writer = csv.writer(csvOutput, delimiter='\t', linetermin
    ator='\n')
12.         reader = csv.reader(csvInput, delimiter='\t')
13.
14. #   Creates a new empty list as well as a variable called "row"
15. defined as a line in the input file.
16.         newList = []
17.         row = next(reader)
18.
19. #   Defines the projection formats to be used for the
20. transformation.
21.         WGS84 = pyproj.Proj(init='epsg:4326')
22.         UTM31N = pyproj.Proj(init='epsg:25831')
23.
24. #   Converts the input coordinates by reading each place in each
25. row in the "coord" file, returning them in their new format
26. and jumping to the next line in the input file.
27.         for row in reader:
28.
29.             x2, y2 = pyproj.transform(WGS84, UTM31N, row[0], row[
    1])
30.
31. #   The converted coordinates will then be added to the empty
32. list created earlier.
33.             row.append(x2)
34.             row.append(y2)
35.             newList.append(row)
36.
37. #   The new list is written to the output file.
38.         writer.writerows(newList)
```